Creep and oxidation behavior of eutectic and eutectoid microstructures in Molybdenum-Silicon-Titanium alloys

Zur Erlangung des akademischen Grades

Doktor der Ingenieurwissenschaften

der Fakultät für Maschinenbau

Karlsruher Institut für Technologie (KIT)

genehmigte

Dissertation

von

M. Sc. Xiangna Cong

Tag der mündlichen Prüfung: 10.10.2017

Hauptreferent: Prof. Dr.-Ing. Martin Heilmaier

Korreferent: Prof. Dr.-Ing. Tilmann Beck

Zusammenfassung

Werkstoffe für höchste Einsatztemperaturen spielen als Materialien für Turbinenschaufeln in Gasturbinen eine herausragende Rolle. Gängige Eisen (Fe)- und Nickel (Ni)-basierte Hochtemperaturmaterialien haben jedoch deutliche Nachteile wie Phaseninstabilität und niedrige Schmelztemperaturen. Um steigenden Leistungsanforderungen zu begegnen, müssen neue Hochtemperaturmaterialien entwickelt werden.

Mo-basierte Legierungen aus dem Mo-Si-Ti System gelten aufgrund ihrer Dichte und Schmelzpunkte als vielversprechende Materialien. Daher wurden in dieser Arbeit Mo-Si-Ti Legierungen in Hinblick auf Verarbeitung, Mikrostruktur und Eigenschaften im Hochtemperaturbereich untersucht. Im Einzelnen wurden geeignete Zusammensetzungen für die Bildung eutektoider und eutektischer Mo-Si-Ti Gefüge identifiziert und deren Gefüge analysiert. Des Weiteren wurde ihr Kriech- und Oxidationsverhalten systematisch untersucht.

Eine geeignete eutektische Mikrostruktur aus (Mo, Ti, Si) + (Ti, Mo)$_5$Si$_3$ wurde bei der Zusammensetzung Mo27.2-Si20.0-Ti52.8 (at.%, E5) gefunden, welche über ein fast ausschließlich eutektisches Gefüge (96.1 vol.%) verfügt. Als geeignete Zusammensetzung für die Bildung eines ausschließlich eutektoiden Gefüges zeigte sich Mo45-Si21-Ti34 (at.%, X5). Zur vollständigen Umwandlung des Gefüges ist eine Wärmebehandlung bei 1300 °C und 200 h notwendig. Der Volumengehalt des eutektoiden Gefüges in dieser Legierung erreichte 99 vol.%.

Das Kriechverhalten beider Legierungen wurde hinsichtlich seiner Last- und Temperaturabhängigkeit untersucht, um die zugrundeliegenden Mechanismen aufzuklären bzw. die am Kriechprozess partizipierenden Phasen zu identifizieren. Der Anstieg der Kriechgeschwindigkeit beider Legierungen bei zunehmender Last konnte anhand eines Spannungsexponenten von knapp 3.5 beschrieben werden und deutet demnach auf durch Versetzungsklettern bestimmtes Kriechen hin. Der Temperatureinfluss auf das Kriechverhalten liefert bei 200 MPa Belastung eine Aktivierungsenergie von knapp 460 bis 470 kJ/mol, was in jedem Fall geringer ist als die aus der Literatur bekannten 510 kJ/mol [Mason and Van Aken, 1995] für einkristallines Mo$_5$Si$_3$ und höher als 350 ± 20 kJ/mol für Ti$_5$Si$_3$ [Rosenkranz et al., 1992]. Es kann geschlussfolgert werden, dass(Mo, Ti, Si) und (Ti, Mo)$_5$Si$_3$ in E5 durch ihren geringen Kriechwiderstand für die signifikant höhere Kriechrate dieser Legierung verantwortlich sind. Im Gegensatz dazu scheint in X5 lediglich (Mo, Ti, Si) zum Kriechen beizutragen, während (Mo, Ti)$_5$Si$_3$ keinen wesentlichen Beitrag zum Kriechen im untersuchten Spannungs- und Temperaturbereich liefert. In Bezug auf das Oxidationsverhalten wurde festgestellt, bei 800 °C und 100 h zeigt E5 allerdings eine bessere Oxidationsbeständigkeit als X5. Die Untersuchung der Oberflächen bzw. Querschnitte beider Legierungen führen zu dem Resultat, dass die höhere Oxidationsbeständigkeit von E5 gegenüber X5 bei 800 °C maßgeblich auf die höhere Oxidationsbeständigkeit der (Ti, Mo)$_5$Si$_3$ Phase in E5 zurückzuführen ist. Demgegenüber kann die Silizidphase (Mo, Ti)$_5$Si$_3$ in X5 nicht zur Bildung einer schützenden Oxidschicht bei dieser Temperatur beitragen. Darüber hinaus wurden Versuche zur Verbesserung des Oxidationsverhaltens von X5 bei 800 °C

durchgeführt. Eine bewusst herbeigeführte Voroxidation von X5 bei 1100 °C für 10 h in Luft führte zu einer signifikanten Verbesserung des zyklischen Oxidationsverhaltens bei 800 °C.

Die weiterführende Optimierung der entstandenen Gefüge durch gerichtete Erstarrung wurde hinsichtlich verschiedener technologischer Probleme untersucht. Im Fall von E5 schränkt ein ausgedehntes Erstarrungsintervall von knapp 600 K unter Nichtgleichgewichtsbedingungen die gerichtete Erstarrung deutlich ein, da ein entsprechender Temperaturgradient zur Unterkühlung der Schmelze technologisch nicht zu erreichen ist. Demzufolge ist unter realen Bedingungen keine stabile Gefügeausbildung und somit auch keine Ausrichtung des Gefüges zu erreichen. Im Falle von X5 wird die Prozessierbarkeit aktuell noch durch Schwierigkeiten bei der schmelzmetallurgischen Herstellung von Halbzeugen für die gerichtete Erstarrung erschwert. Der Umweg über pulvermetallurgische Halbzeuge zeigt die prinzipielle Eignung der gerichtete Erstarrung von $(Mo, Ti)_3Si$ und ihrer anschließenden Umwandlung zu (Mo, Ti, Si) + $(Mo, Ti)_5Si_3$.

Literatures:

Mason, D. and Van Aken, D.C., *On the creep of directionally solidified* $MoSi_2$*-*Mo_5Si_3 *eutectics*. Acta metallurgica et materialia, 1995. 43(3): p. 1201-1210.

Rosenkranz, R., Frommeyer, G., and Smarsly, W., *Microstructures and properties of high melting point intermetallic* Ti_5Si_3 *and* $TiSi_2$ *compounds*. Materials Science and Engineering: A, 1992. 152(1-2): p. 288-294.

Declaration

I hereby declare this work was produced by me with help of the stated aids and appliances only. To the best of my knowledge and belief, it contains no material previously published or written by another person, except for where due reference has been given. The rules for good scientific practice of the Karlsruhe Institute of Technology (KIT) have been respected.

Outside of the Department of Mechanical Engineering of the Karlsruhe Institute of Technology (KIT) no other doctoral procedures are pending or have been finalized unsuccessfully.

Ich erkläre hiermit, die vorliegende Arbeit selbstständig angefertigt und keine anderen als die angegebenen Quellen und Hilfsmittel benutzt zu haben. Wörtlich oder inhaltlich übernommene Stellen wurden als solche kenntlich gemacht. Die Satzung des Karlsruher Instituts für Technologie (KIT) zur Sicherung guter wissenschaftlicher Praxis wurde beachtet.

Hiermit erkläre ich, dass für mich Promotionsverfahren außerhalb der Fakultät für Maschinenbau des Karlsruher Instituts für Technologie (KIT) weder anhängig sind noch erfolglos abgeschlossen wurden.

Karlsruhe, den 21.06.2017

(Xiangna Cong)

List of symbols

σ	Stress
ε	Strain
$\dot{\varepsilon}$	Strain rate
Q	Activation energy
R	Avogadro constant
T	Temperature
Δm	Mass gain
k_l	Linear rate constant of oxidation
k_p	Mass gain related parabolic rate constant
A	Surface area
t	Time
θ	half the angle between the incoming beam and the diffracted beam
d	spacing between two parallel crystal planes that cause the reinforcement of the beam
λ	Wavelength
m	Mass
ρ	Density
S	Microstructural parameter
P	Phase boundary density
N	Amounts of the phase boundary in a straight line that is arbitrarily set in SEM images
L	Length of the straight line

List of abbreviations

CC	Conventionally Cast
DS	Directionally Solidified
SC	Single Crystalline
BCC	Body Centered Cubic
FCC	Face Centered Cubic
BSE	Back-scattered electrons
SE	Secondary electrons
SEM	Scanning electron microscope
EDS	Energy dispersive spectroscopy
XRD	X-ray diffraction
TGA	Thermo Gravimetric Analysis

List of Figures

List of Tables

Table of contents

1 Introduction

This chapter introduces the development and principle of gas turbines. In addition, common high temperature materials including Iron-based alloys and Nickel-based alloys which are applied in these turbines are introduced. Their advantages and disadvantages are presented as a reference for new high temperature materials.

1.1 Gas turbine

A gas or combustion turbine is a type of internal combustion engine [1]. From the 18th century on, people began to be interested in gas turbines. In 1791, John Barber issued the first patent for a gas turbine. However, early gas turbines were inefficient because the power used for operating the compressors outweighed the generated power by the turbine [2]. Until the middle of the 20th century, gas turbines were developed into practical devices, primarily known as jet engines [3]. Since then gas turbines have been widely used in aircrafts [4].

As shown in Figure 1.1, a simple gas turbine consists of a compressor, a combustor and a power turbine. Specifically, in the gas turbine the flowing air is compressed by a compressor, then mixed with fuel and ignited in a combustion chamber to become a high temperature gas. Then, the expanding hot gas passes through the turbine and drives the turbine blades to rotate.

Blades are, thus, key components of gas turbine engines. A gas turbine engine usually contains three or four rows of turbine blades, and each row consists of about 60-100 turbine blades. The turbine blades can rotate with a speed of about 10000 rpm at a temperature of up to 1000 ℃ [5]. Hence, the turbine blades are greatly affected by the centrifugal forces and the temperature in a corrosive atmosphere, which is an extreme challenge for the turbine blade material.

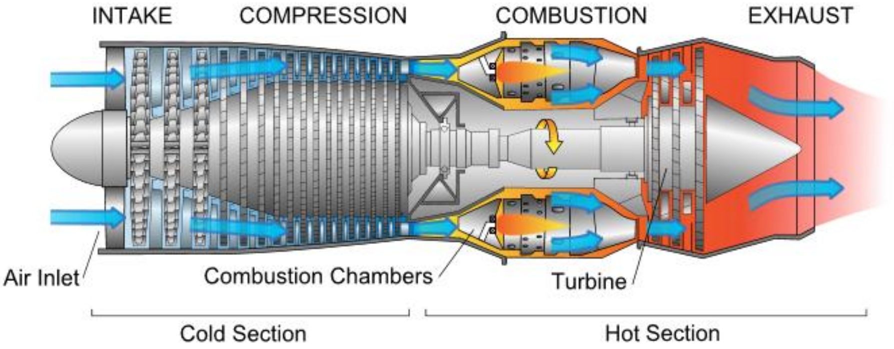

Figure 1.1: Schematic of gas turbine engines [6]

1.2 Common high temperature materials

Materials used in gas turbines have gone through many incremental improvements since the first practical turbines were developed in the 1940s [7]. Common high temperature structural materials mainly include Iron (Fe)-based alloys and Nickel (Ni)-based alloys.

1.2.1 Iron-based alloys

Fe-based alloys have been predominant in turbine wheels and blades due to their elevated temperature mechanical properties and cost effectiveness [8]. For example, A286 (a Fe-Ni-Cr alloy with significant additions of Molybdenum (Mo), Titanium (Ti) and Manganese (Mn)) is a typical austenitic Fe-based alloy of precipitation-hardening type [9-11]. The strengthening is mainly attributed to the intermetallic γ' phase (Ni_3(Al, Ti) with $L1_2$ structure) [11]. This alloy shows good mechanical properties at service conditions as well as at room temperature. Besides, also good corrosion resistance is provided due to the elevated Chromium (Cr) content. However, A286 is microstructurally unstable after short thermal exposure at 730°C because the strengthening phase γ' transforms to η phase (hcp Ni_3Ti), which leads to a degradation of the good mechanical performance of the material. Hence, A286 can only be used at temperatures below 730 ℃ to avoid the decrease in strength of the alloy [12].

1.2.2 Nickel-based alloys

Ni-based alloys which contain large amounts of Ni are typically strengthened by precipitates. Since the 1950-60s, Ni-based alloys, particularly single crystal Ni-based alloys, have been widely applied in jet engines and industrial gas turbines due to their outstanding high-temperature strength, excellent corrosion and creep resistance [13-19].

Figure 1.2 shows the progress of temperature capability of Ni-based alloys. Ni-based alloys have gone through different optimization stages including wrought, conventionally cast (CC), directionally solidified (DS), and single crystalline alloys (SC). Compared with polycrystalline materials, SC alloys of the first generation had a more homogeneous microstructure, which was due to the dissolution of the γ/γ' eutectic interdendritic nodules and secondary γ' precipitates [20, 21]. Furthermore, a pronounced improvement of SC alloys in mechanical properties [22-24] was obtained by the addition of Rhenium (Re) to enhance creep strength mainly by solid solution strengthening of the γ matrix [25, 26] or by the addition of Ruthenium (Ru) to extend the phase stability and reduce the density [27-30].

Generally, Ni-based single crystal alloys consist of two major phases, γ and γ' (Figure 1.3), which possess disordered face centered cubic (FCC) and ordered $L1_2$ crystal structures, respectively [19, 30]. Single crystal alloys exhibit exceptional creep resistance by the combined effect of strengthening γ' phase which hinders the movement of dislocation, particularly when the volume fraction γ' phase is in the range of 60-

70 vol.% [20, 31], and by the removal of grain boundaries transversely located to the applied creep stress being the cause for premature creep rupture due to void and crack formation [32, 33].

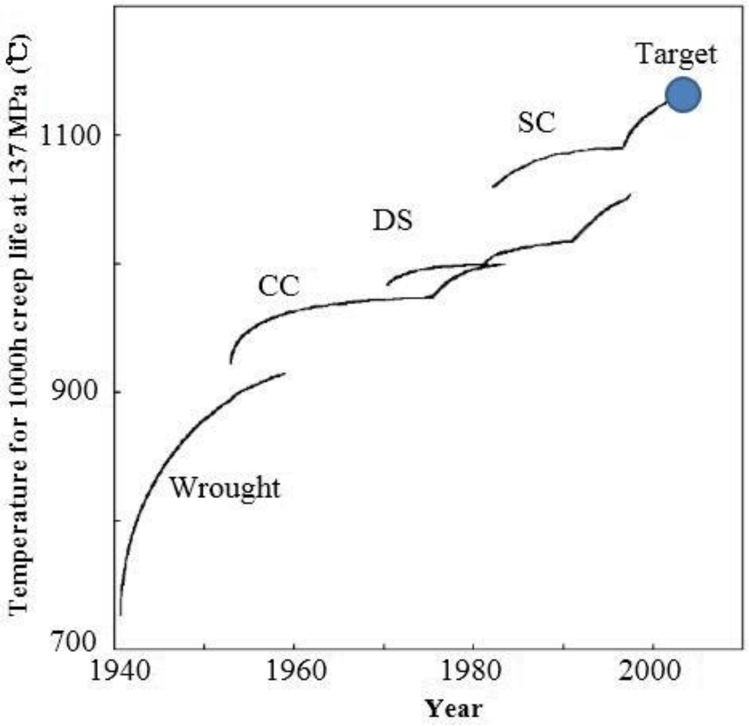

Figure 1.2: History of improvement in temperature capability of Ni-based alloys [34]

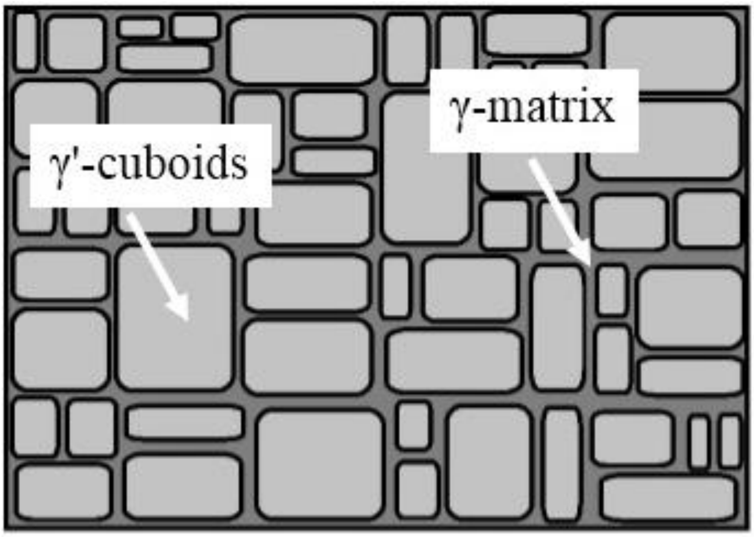

Figure 1.3: γ-γ' microstructure of a nickel-based single crystal alloy [19]

At present, single crystal Ni-based alloys used in turbine blades are operated at almost 1150 ℃, which is close to 90% of their absolute melting point [35]. In Figure 1.4, jet turbine efficiency is expressed as a function of the power produced from increasing inlet temperatures. It is found that the specific core power increases with increasing rotor inlet temperature. Importantly, the solvus temperature of the strengthening γ' phase is around 1300°C, and its volume fraction reduces already when the turbine rotor inlet temperature reaches 1150 ℃ [36]. Hence, it is difficult to apply Ni-based alloys at even higher temperatures. In order to increase the operating temperature of turbine blades, complex cooling systems and thermal barrier coatings have become common in turbines [37]. These cooling methods, however, result in increased deviation from the ideal performance (Figure 1.4) thereby increasing the efficiency losses.

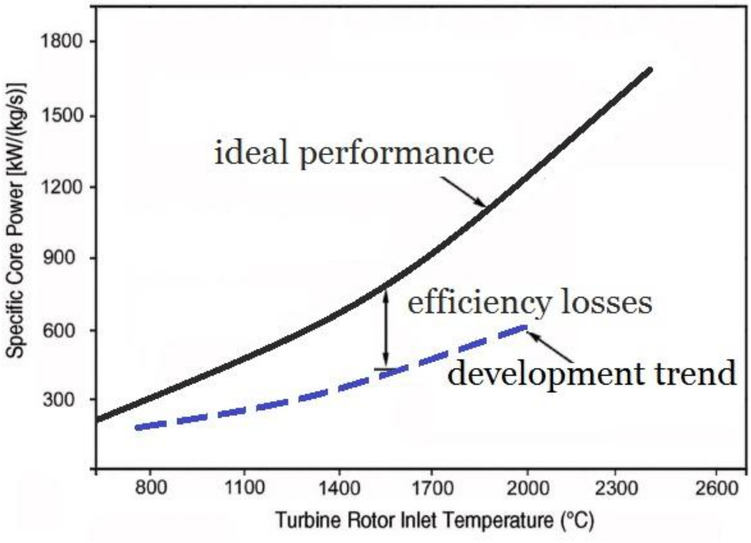

Figure 1.4: Specific core power vs. turbine inlet temperature for gas turbine engines [35]

In order to solve the problem of efficiency losses, the development of new alternative materials is necessary for high temperature gas engines. While several alternatives have been discussed in literature [38-45] , one of the most promising high-temperature materials are Mo-based alloys [35, 46-48]. Because of their much higher melting temperatures, Mo-based alloys can probably be operated at several hundred degrees higher than Ni-based alloys [49]. In the recent decades, research interest on Mo-based alloys has considerably increased [35, 46, 50, 51].

2 High temperature materials properties

Creep and oxidation behavior are basic properties and requirements for high temperature materials. In this part, characteristics of creep and oxidation behavior including the brief principle, the classification method and relevant equations describing the mechanistic behavior are summarized.

2.1 Characteristics of creep behavior

Creep is a thermally activated process, which is characterized by a time-depending plastic deformation of materials at a high temperature (T) and a constant stress (σ). As shown in Figure 2.1, a creep curve can be generally divided into three different stages including primary (stage I), secondary (stage II) and tertiary creep (stage III). Specifically, as shown in Figure 2.1 (b), the slope of the curves, i.e., the strain rate $\dot{\varepsilon}$, slowly declines with the increase of the strain in stage I, and then reaches a constant value. In stage II, when the creep rate stays approximately constant for more than 0.02 in strain, the term “true steady-state creep rate” is employed to evaluate the creep behavior. If no such constancy in strain rate is found, the term “minimum creep rate” is rather used. Subsequently, the creep rate steeply rises until fracture occurs in the stage III.

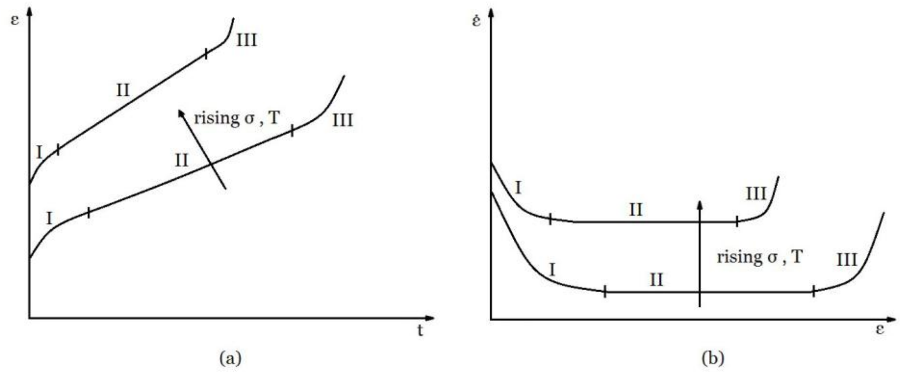

Figure 2.1: Schematic creep curve showing three different creep regimes [52]

Steady state is frequently observed only in simple material systems, i.e. in singe phase material [53]. In addition, minimum creep is also employed to evaluate the creep behavior in many researches [54-58]. Actually, minimum creep is more often used than steady state because there is no steady state which in turn results from the fact that the microstructure of the materials is often unstable at elevated temperatures [59].

According to the results of preliminary experiments, the term “minimum creep rate” is used to describe the creep behavior in this research.

Based on power law equations, the minimum creep rate ($\dot{\varepsilon}_m$) is expressed by the following equation [60]:

$$\dot{\varepsilon}_m = A\sigma^n \exp(-\frac{Q}{RT}) \quad (2.1)$$

where A is a constant, *n* is the stress exponent, Q is the activation energy for creep and R is the gas constant.

The stress exponent *n* can be used for the analysis of the creep mechanism, *n* can be identified by plotting the (double logarithmic) strain rate dependence of stress, the so called “Norton plot” as follows:

$$n = \frac{\Delta log\dot{\varepsilon}_m}{\Delta log\sigma} \quad (2.2)$$

The activation energy for creep can be determined by an Arrhenius law type behavior deduced from equ. (2.1) as:

$$Q = -R(\frac{\partial log\dot{\varepsilon}_m}{\partial(\frac{1}{T})})_\sigma \quad (2.3)$$

2.2 Characteristics of oxidation behavior

Oxidation is a special type of high-temperature corrosion behavior. Normally the term “oxidation” is used to describe the process when a material reacts with oxygen by forming an oxide [61]. Because high temperature materials are mainly applied in oxygen containing environments, oxidation is the most important form of high temperature corrosion. Besides the thermodynamic parameters, the kinetic analysis of high temperature oxidation behavior is an integral part for the prediction of the oxidation behavior. In general, the oxidation kinetics can be analyzed by measuring the specific mass change of a specimen (normalized to the specimen surface) over time or analyzing the thickness of the growing oxide scale in time intervals.

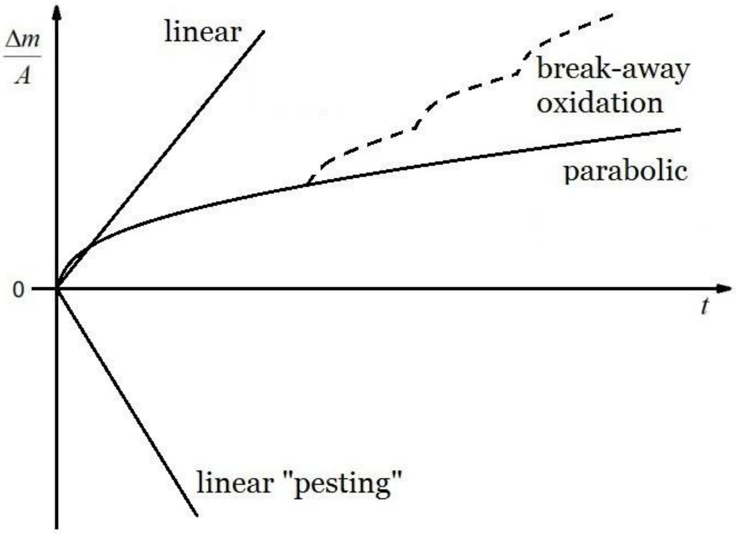

Figure 2.2: Idealized kinetic rules of mass change over time for various oxidation processes [62]

As shown in Figure 2.2, the oxidation kinetics of a metal may follow a parabolic rate law which can be expressed as:

$$\left(\frac{\Delta m}{A}\right)^2 = k_p \cdot t \tag{2.4}$$

where Δm is the mass change, A is the surface of specimen, k_p is the parabolic rate constant.

When oxidation kinetics of a metal proceeds at a constant rate, a linear rate law will be adopted which is expressed as follows:

$$\left(\frac{\Delta m}{A}\right) = k_l \cdot t \tag{2.5}$$

where k_l is the linear rate constant.

Pesting, the disintegration (fracture) of the intermetallic into smaller particles at the oxidation temperature, was first studied by Fitzer [63], who focused on the pest oxidation of $MoSi_2$. Westbrook and Wood [64] illustrated that pesting occurred in a wide range of intermetallic compounds. The pesting is summarized as a rapid attack on the sample which is preceded by an incubation period. In addition, the disintegration occurs within a limited temperature range [65].

Break-away oxidation means the loss of a protective oxide scale because of its mechanical failure and therefore the transition to a faster oxidation, generally expressed by linear rate law [61, 66, 67].

3 Literature overview for Mo-based alloys

This chapter reviews the development process from Mo to Mo-Si-B alloys and finally to the Mo-Si-Ti alloys, which are the subject of the present thesis. Creep and oxidation behavior of the participating phases are reviewed from literature. In addition, the goals and research contents of this thesis are described.

3.1 Molybdenum

As a refractory metal element, the melting point of Mo is with 2620 °C already very high, which is only surpassed by the following elements Tantalum (Ta), Tungsten (W), Osmium (Os) and Re [68]. In addition, Mo as pure element exhibits suitable ductility and room temperature fracture toughness, making Mo a candidate for high temperature applications [69].

Due to the demand for developing high temperature materials, several researchers have focused on the improvement of the mechanical behavior of Mo and its alloys in the last 70 years [68, 70]. However, these alloys could only be used in an inert environment at elevated temperatures. This is because Mo is unstable in oxidizing environment due to the rapid formation of the orthorhombic oxide MoO_3 above 500 °C. This leads to a catastrophic oxidation behavior typically referred to as “pesting” [71], and this is the most challenging issue for development of Mo based high temperature materials.

3.2 Molybdenum-Silicon alloys

In order to improve the oxidation resistance of Mo, Mo-Silicon (Si) alloys including Mo solid solution (highlighted as (Mo, Si) in this work) and intermetallic phases such as $MoSi_2$, Mo_3Si and Mo_5Si_3 obtain increasing attention (Figure 3.1).

As a solid solution strengthener, Si can significantly enhance strength but typically deteriorates room temperature fracture toughness of (Mo, Si). Sturm et al. [72] found the yield strength of Mo being substantially increased by the addition of only 0.1 wt.% Si. However, at the same time, the room temperature toughness of the Mo-Si alloy showed a steep reduction from ~24 MPa $\cdot m^{1/2}$ to ~ 8 MPa $\cdot m^{1/2}$. The results were attributed to the increased strength and a change from transgranular to intergranular fracture. As said before, pure Mo is easily oxidized above 500 °C. Hence, in multiphase materials reducing the fraction of

(Mo, Si) is considered as a suitable strategy to obtain good oxidation resistance. However, (Mo, Si) is also useful for maintaining the damage tolerance of multiphase alloys.

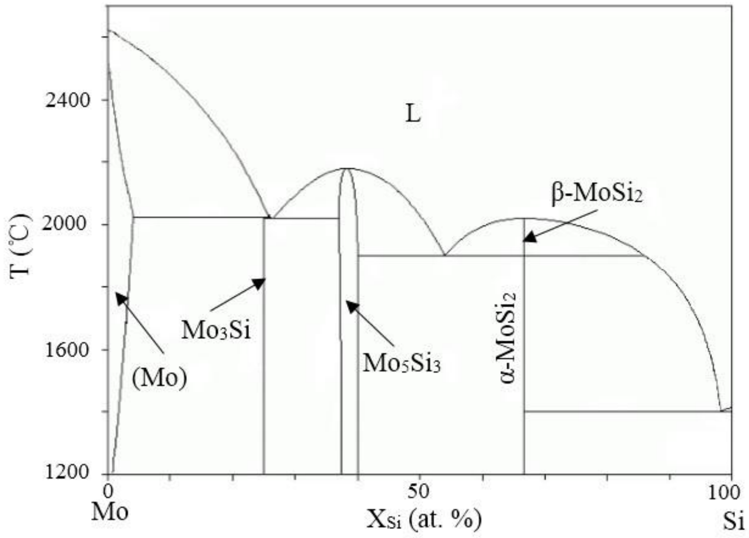

Figure 3.1: Molybdenum-Silicon binary phase diagram [73]

Miller et al. [74] found that addition of 0.16 at.% Zr improved the room temperature ductility of Mo-based alloys. The formation of ZrO_2 was considered to reduce the content of oxygen at the grain boundaries and thus to improve the grain boundary strength. Similarly, Saage et al. [69] concluded that the addition of Zr prevented the segregation of Si to the grain boundaries, which resulted in the improvement of grain boundary cohesive strength and increase of ductility. In addition, Scruggs [75] pointed out that additions of $MgAl_2O_4$ spinel particles getters detrimental impurities (such as nitrogen and oxygen), therefore, the Mo matrix metal is more pure, increasing its ductility. Schneibel et al. [76] also demonstrated that $MgAl_2O_4$ spinel played an important role in improving the ductility of Mo-based alloys. Fracture initiated at microcracks which were found on the surfaces of Mo-$MgAl_2O_4$ samples during tensile testing. The ductility maximum is attributed to the change in microcrack length and the ultimate tensile stress, as the volume fraction of $MgAl_2O_4$ increases. By contrast, Gunter et al. [77] found that no improvement of the fracture toughness occurred when $MgAl_2O_4$ particles were added up to 5 vol.%. They speculated that the reason for the former found improvement in ductility was the reduction of grain size, not $MgAl_2O_4$ spinel particles. Hence, an efficient strategy to improve the ductility of Mo-based alloys was grain refinement rather than adding $MgAl_2O_4$.

The intermetallic phase with the highest Si content in the binary Mo-Si phase diagram, $MoSi_2$ exhibits $Cl1_b$ crystal structure [78]. The fracture toughness of $MoSi_2$ single crystal varies in literature, probably because several different methods were applied to determine it. For instance, with pre-cracked bending specimens, Ito et al. [79] found fracture toughness values on the (110) plane and (001) plane of 2.4 MPa $m^{1/2}$ and 4.0 MPa $m^{1/2}$, respectively. However, Peralta et al. [80] reported fracture toughness values with an indentation approach of 6.1 MPa m$^{1/2}$ on the (110) plane and 2.5 MPa m$^{1/2}$ on the (001) plane of $MoSi_2$. By contrast, Yoo and Yoshimi [81] employed an empirical model showing calculated values of 1.8 MPa m$^{1/2}$ on the (110) plane and 1.9 MPa m$^{1/2}$ on the (001) plane. In addition, a fracture toughness of ~3 MPa m$^{1/2}$ for $MoSi_2$ was also reported [82, 83].

Kircher et al. [84] and Sharif [85] proved that $MoSi_2$ forms a protective SiO_2 scale in the temperature range of 1400-1700 ℃. However, at the temperature of 500 ℃, pesting was observed [86]. Liu et al. [87] gave an explanation for this behavior, they demonstrated that the low diffusion coefficient of $MoSi_2$ at low temperatures made it impossible to form a continuous silica layer, which resulted in the co-oxidation of Si and Mo, and formation of a mixed oxides scale. The formed MoO_3 accelerated volume changes of the mixed oxides scale. The remarkable volume expansion ruptured the oxide scale and accelerated the oxidation process, and then the pest phenomenon occurs. A similar pesting phenomenon was also reported by Yanagihara et al. [88]. They found the initial cracks distributed in the samples after arc-melting. The initial cracks play much more effect on pesting phenomenon than grain boundaries and the oxidation layer. About 200% volume expansion occurred during the co-oxidation process. The formation of $Mo(Si, Al)_2$ with the addition of Al decreased the pesting rate by the reduction of initial cracks.

$MoSi_2$ has a high creep rate at elevated temperatures, which prevents its structural application [89]. Umakoshi et al. [90], Maloy et al. [91] and Kimura et al. [92] demonstrated that the creep resistance of single crystals $MoSi_2$ on the [001] orientation was 3-4 times higher than that of non-[001] oriented SC up to 1400 ℃, which was attributed to the absence of <010> slip [93], and activation of ½ <331> and ½ <111> [4]. Furthermore, Inui et al. [94] found that the creep rate of $MoSi_2$ improved significantly with the addition of Re and Niobium (Nb) in the temperature range 1200-1400 ℃.

Since the coexistence of $MoSi_2$ and (Mo, Si) in thermodynamic equilibrium is not possible [95], other Mo-rich silicides such as Mo_3Si and Mo_5Si_3 had to be investigated for the oxidation- and creep resistance, too. Mo_3Si exhibits an A15 cubic structure and was initially considered to be a stoichiometric compound by Christensen [96]. However, Rosales et al. [97] showed that Mo_3Si had a phase region of 0.5% width after cooling in the furnace from 1600 ℃, and that the composition of single phase Mo_3Si was around Mo-24 at.% Si, indicating Mo_3Si is not a stoichiometric compound. They also investigated the room temperature fracture toughness of single phase Mo_3Si, which showed an average value of 3 MPa m$^{1/2}$. Due to the higher Mo content, Mo_3Si exhibits much poorer oxidation resistance than $MoSi_2$. But very little attention was paid to investigate the oxidation performance of Mo_3Si with further alloying additions. The studies focused on the addition of different elements. Ochiai [98] pointed out that more than 10 at.% Aluminum (Al) or 15 at.% Chromium (Cr) addition reduced the oxidation rate of Mo_3Si at 900 ℃. Rosales et al. [99] found that increasing Al content improved the oxidation resistance of Mo_3Si in the temperature range of 700-1000 ℃, and the sample with 16 at.% Al showed an excellent oxidation behavior due to the formation of a mixed SiO_2 and Al_2O_3 oxide scale. The compression creep behavior of

Mo_3Si was researched in vacuum at 1325 ℃ by Rosales et al. [100]. Slip trace analysis exhibited the active slip planes to be {001} and {012}, with similar critical resolved shear stresses.

Another Mo-rich silicide in the Mo-Si system is Mo_5Si_3, which exhibits a tetragonal crystal structure [41-43]. A solubility range of 2.1 at.% Si in Mo_5Si_3 was found by Ström [101], demonstrating that Mo_5Si_3 is not a stoichiometric compound. It was reported that Mo_5Si_3 had a room temperature fracture toughness above 2 MPa·$m^{1/2}$ [102]. Furthermore, Mo_5Si_3 exhibits a better oxidation resistance than Mo_3Si, where the high Mo content still limits its application in oxidizing environments [103, 104]. Higher temperature improved the formation of the protective silica passivation layer due to the volatilization of MoO_3. In addition, Meyer et al. [105] and Akinc et al. [106] found that the addition of B decreased the viscosity of the SiO_2 scale. A silica passivation layer was formed and the pores that formed by the volatilization of MoO_3 were quickly closed. In particular, only 1-3 wt.% B significantly decreased the oxidation rate of Mo_5Si_3 by more than 5 orders of magnitude at 1200 ℃.

Furthermore, Mo_5Si_3 exhibited compressive plasticity above ~1300 ℃, whereas at lower temperatures brittle fracture was observed by Yoshimi et.al [107]. Meyer et al. [108] also studied the compressive creep behavior of Mo_5Si_3 in the temperature range of 1240-1320 ℃ and 140-180 MPa. An average creep stress exponent of 4.3 was obtained, indicating that the creep rate was controlled by dislocation climb [109].

Table 3.1 comprehensively shows the main properties of the different phases including (Mo, Si), $MoSi_2$, Mo_3Si and Mo_5Si_3.

Table 3.1: The main properties of different phases [73]

Properties	**Crystal structure**	**Strukturbericht designation, Person symbol, and Space Group**	**Room temperature fracture toughness**	**Oxidation behavior**	**Creep behavior**
(Mo, Si)	Body-centered cubic	-	~8 MPa $m^{1/2}$ with 0.1 wt.% Si [72]	easily oxidized above 500 ℃	-
α-$MoSi_2$	Body-centered tetragonal	$C11_b$, tI6, I4/mmm	~3 MPa $m^{1/2}$ [82, 83]	a protective scale up to 1500 ℃ [84]	high creep rate [89]
Mo_3Si	Cubic	A15, cP8, $Pm\bar{3}n$	~3 MPa $m^{1/2}$ [97]	poorer oxidation resistance than $MoSi_2$	limited plastic deformation [100]
Mo_5Si_3	Body-centered tetragonal	$D8_m$, tI38, I4/mcm	~2 MPa $m^{1/2}$ [102]	poor oxidation resistance [103, 104]	high creep resistance [80]

3.3 Molybdenum-Silicon-Boron alloys

Considering the requirements of mechanical properties such as oxidation resistance and creep resistance, both, single phase intermetallics and multiphase binary Mo-Si alloys are unable to satisfy all the properties demanded for high temperature environments. Hence, some researchers began to pay close attention to Mo-Si-B alloys.

Figure 3.2 shows the Mo-rich part of the 1600 ℃ isothermal section of the Mo-Si-B phase diagram, which was researched by Nowotny et al. and improved later by Nunes et al. [95]. There are two important phase fields in the phase diagram, namely Mo_3Si-Mo_5Si_3-Mo_5SiB_2 (green triangle) and (Mo, Si)-Mo_3Si-Mo_5SiB_2 (blue triangle). Among them, the (Mo, Si)-Mo_3Si-Mo_5SiB_2 field obtains more attention for high temperature applications [82, 83]. In addition to the observed high melting temperatures of these alloys, the fracture toughness is considerably improved by (Mo, Si) as a ductile phase. Furthermore, Mo_5SiB_2 phase facilitates the formation of a molten borosilicate scale leading to improved oxidation resistance of the alloys. Moreover, no low temperature phase transition is present in the three-phase field. Thus, abrupt changes of mechanical properties are avoided in the entire temperatures range [42].

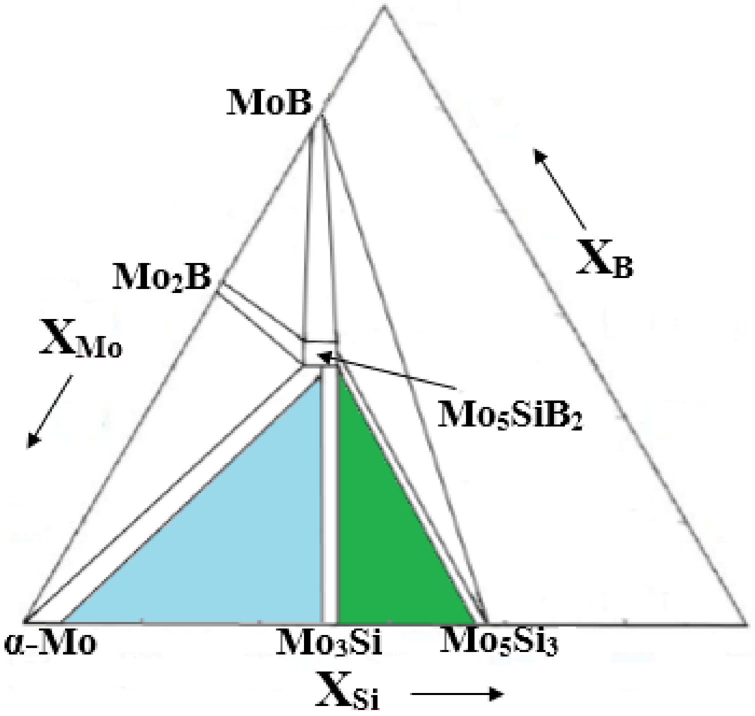

Figure 3.2: Mo-rich part of isothermal of Mo-Si-B phase diagram at 1600 ℃ [110]

The high temperature oxidation resistance of Mo-Si-B alloys was investigated by several researchers. For instance, Meyer et al. [111] found a two-step oxidation process was present in the initial scale formation for Mo-Si-B intermetallics containing 81-88 wt.% Mo. First a transient oxidation was observed for all compositions with a mass gain due to MoO_3 and SiO_2 formation. The second period exhibited a plateau region of slow oxidation rate. In addition, Parthasarathy et al. [112] found that for B-containing silica-scale formation, volatilization of B_2O_3, and the lowered viscosity of SiO_2 scale can be considered as main parameters for the kinetics of the oxidation behavior in a (Mo, Si)-Mo_5SiB_2-Mo_3Si alloy in the temperature range of 500-1300 ℃. Figure 3.3 shows the oxidation mechanism map in Mo-Si-B alloys, as developed by Parthasarathy et al. [112] and later improved by Dimiduk and Perepezko [35]. At temperatures below 700 ℃, the formation of MoO_3(s) results in a parabolic weight gain. At 700 ℃-750 ℃, MoO_3 begins to sublimate from the substrate. However, because of the high viscosity of SiO_2 at those temperatures, a protective scale is not formed. Hence, a linear weight loss occurs in the alloy. Above 750 ℃, a borosilicate scale forms. However, it is still found that the weight loss at 800 ℃ is much greater than that at 1300 ℃.

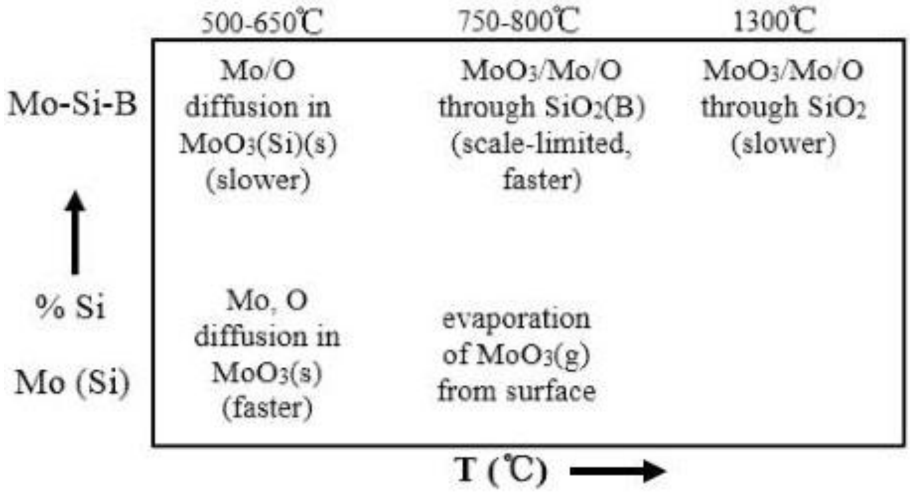

Figure 3.3: Oxidation mechanism map in temperature-composition space for selected Mo and Mo-Si-B alloys [35]

Supatarawanich et al. [113, 114] concluded that the best oxidation resistance of multiphase Mo-Mo_5SiB_2-Mo_3Si alloy was obtained with a Si:B ratio of 1:1 at 1300 ℃, and Mo_3Si provided a source of Si for controlling the composition of the glass scale at 1300 ℃. In addition, Wang et al. [115] found that the laser-remelted alloy showed a finer three-phase Mo-Mo_5SiB_2-Mo_3Si eutectic microstructure than the original alloy, leading to an improvement in the oxidation resistance by approximately an order of magnitude.

Furthermore, the effect of different (minor alloying) elements on the oxidation resistance of Mo-Si-B alloys was investigated. Majumdar et al. [116] found that Y significantly reduced the oxidation rate of the Mo-9Si-8B alloy in the temperature range of 650-1400 ℃,which was due to the formation of yttrium-silicate scale that limits inward diffusion of oxygen. Gorr et al. [117] pointed out that the presence of Y-rich inclusions in the borosilicate layer decrease the viscosity of the borosilicate scale. The flowing ability of the oxide layer was significantly improved, especially at 1000 ℃ and 1100 ℃. The probable reason was the presence of Y_2O_3 in the silica, and thus the oxide scale is less viscous and flows easier over the pores preventing the evaporation of gaseous MoO_3 [116]. They also found that the addition of Zr improved the oxidation behavior by reducing the time necessary for the formation of a protective oxide scale. Above 1150 ℃ the protective scale became unstable because of the phase transformation of ZrO_2 from a monoclinic to a tetragonal crystallographic structure [118]. Unfortunately, this phase transformation is accompanied by a volume decrease resulting in the formation of open pores in the SiO_2 scale. As the exposure time increases, the diameter of the pores enlarges leading to the evaporation of MoO_3 [119]. In addition, Majumdar et al. [120] demonstrated that the enrichment of La in the oxide/alloy interface of La-alloyed Mo-Si-B also resulted in an excellent oxidation resistance in the temperature range of 750-1300 ℃. Majumdar et al. [120] and Schliephake et al. [121] concluded that Ti addition increased the oxidation rate compared with the Mo-9Si-8B alloy. The authors argued that the formation of a porous duplex scale allowed easy oxygen diffusion to the interface of the substrate and the alloy.

Creep resistance is also a key indicator for the performance of high temperature materials. Jain et al. [122] confirmed that a Mo solid solution matrix phase with higher Si content and intermetallic phases (Mo_5SiB_2 and Mo_3Si) present in higher volume fractions exhibits a decreased creep rate compared with Mo solid solution alloy. Si addition in Mo caused pronounced solid solution strengthening. They pointed out that this high dissolved Si level, noted in the Mo solid solution alloy, not only substantially hardened the matrix and enhanced the high-temperature strength, but also enhanced the tensile creep resistance. In addition, coarse microstructures of Mo-Si-B alloys showed better creep resistance than fine microstructures when the temperature was higher than around 1300 ℃ [123]. This is because at high temperatures the fine microstructure is associated with poor strength because of the presence of a high density of high diffusivity interfaces. The effect of the diffusivity interfaces becomes less important at low temperatures and Hall-Petch hardening may be a key factor. Thus, the creep strength of this fine grained alloys at 1200 ℃ is similar to that of coarse-grained alloys.

The addition of different elements can also influence the creep behavior of Mo-Si-B alloys. Yoshimi et al. [124] concluded that Mo-5Si-10B-7.5TiC had good compressive deformability in the temperature range 1000-1600 ℃. Particularly, the alloy had a twice higher strength than Mo-6.7Si-7.9B at and above 1200 ℃. They pointed out that (Mo, Ti)C and $(Mo, Ti)_2C$ played an important role in determining the high-temperature deformation and strength properties of TiC-added Mo-Si-B alloys. Hochmuth et al. [125] demonstrated that addition of 1 at.% Zr significantly improved the grain boundary strength and led to decreased creep rates of the alloys by reducing the formation of SiO_2 on the grain boundaries. Furthermore, Yu et al. [126] investigated the tensile properties of Mo-10Si-14B-3Hf and Mo-9Si-8B-3Hf alloys manufactured by a powder metallurgy process. The results indicated that the Mo-10Si-14B-3Hf alloy showed a high strength of 560 MPa at 1400 ℃ due to the formation of Mo_3Si and Mo_5SiB_2. Furthermore, Mo-9Si-8B-3Hf showed superplasticity in the temperature range of 1400 to 1560 ℃, so it provided a possible solution for overcoming the poor formability of Mo-Si-B alloys by powder metallurgy at elevated temperature.

3.4 Goals and research contents

Besides excellent properties including oxidation and creep resistance at high temperature, the density of high temperature materials is also very important for high temperature application. Unfortunately, density is high for Mo-Si-B alloys. Alloying strategies addressing this issue have thus to be developed.

Substitution of Mo by Ti leads to a pronounced effect in reducing the density of the alloys. Jéhanno et al. [46] calculated the composite density of Mo-9 at.% Si-8 at.% B and obtained a value of 9.6 g/cm^3. Schliephake et al. [121] found that the density of Mo-9 at.% Si-8 at.% B-29 at.% Ti was 7.8 g/cm^3. Hence, the addition of Ti significantly reduces the density of Mo-alloys for high temperature application.

Table 3.2 shows the main advantages and disadvantages of the relevant alloys including Fe-based alloys, Ni-based alloys, Mo-Si-B alloys and Mo-Si-Ti alloys. After the comparison of their properties, it is easy to conclude that Mo-Si-Ti alloys are promising candidates due to their high melting point and low density.

Table 3.2: The comparison of different high temperature alloys

Properties	Main Advantages	Main Disadvantages
Fe-based alloys	easy and cheap to produce	phase instability (strengthening phase γ' transforms to η phase)
Ni-based alloys	excellent strength (high volume fraction γ' phase)	decreasing strength (above ~1150 ℃)
Mo-Si-B alloys	high melting point (above 2000 ℃)	high density (around 9.6 g/cm^3)
Mo-Si-Ti alloys	high melting point, low density (around 7.7 g/cm^3)	-

In-situ composites including equilibrium phases have greater competitiveness than artificial composites with regard to the interface stability at elevated temperatures [127]. Hence, eutectic or eutectoid microstructures which can be called in-situ composites should perform better. Besides the good performance such as high melting point and low density of Mo-Si-Ti alloys, Ti might pose a positive effect on (Ti, Mo)$_5$Si$_3$ [128, 129] and (Mo,Ti)$_5$Si$_3$ for the oxidation resistance [130]. In addition, eutectic and eutectoid microstructures of Mo-Si-Ti alloys can be further modified to lamellar microstructures by directional solidification technology, which is considered to cause improvement in the creep resistance. Therefore, the research on Mo-Si-Ti alloy was conducted in this research.

Yang et al. [131] developed a thermodynamic data set for Mo-Si-Ti alloys using the CALPHAD (CALculation of PHAse Diagram) approach. The experimental observation showed a good correlation with thermodynamic descriptions of the Mo-Si-Ti system. Based on their research, a liquidus projection of Mo-Si-Ti alloys is shown in Figure 3.4, which includes (Mo, Ti, Si) and intermetallic compounds within this system such as (Mo, Ti)$_5$Si$_3$ and (Ti, Mo)$_5$Si$_3$. In (Mo, Ti)$_5$Si$_3$, Mo is partly substituted by Ti and the solubility of Ti is about 40 at.%. In (Ti, Mo)$_5$Si$_3$, the solubility of Mo is about 12.5 at.% [131, 132].

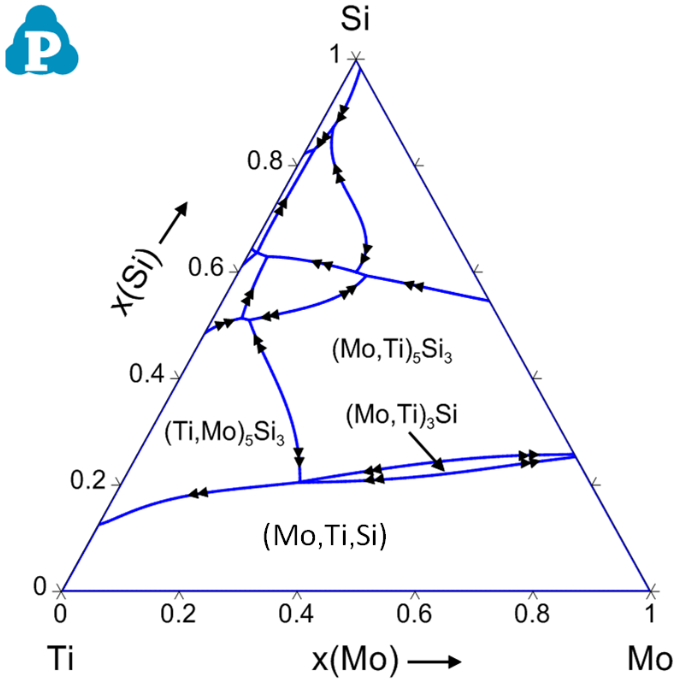

Figure 3.4: The calculated liquidus projection of the Mo-Si-Ti system

Few manuscripts report on the mechanical properties of (Ti, Mo)$_5$Si$_3$, so Ti_5Si_3 is introduced as a reference due to its identical crystal structure. It was reported that the room fracture toughness of Ti_5Si_3, a Mn_5Si_3-type silicide ($D8_8$ structure) [133], was 2.1 MPa m$^{1/2}$ at a grain size of 20-50 μm [134] and 2.69 ±0.21 MPa m$^{1/2}$ at a grain size of 5 to 6 μm [135]. The data demonstrated that finer grain size of Ti_5Si_3 led to higher fracture toughness, which is probably attributed to the reduction in the density of microcracks, compared with that with coarse grain size [136]. Abba et al. [137] noted poor oxidation resistance of Ti_5Si_3 in air above 850 ℃, while Taniguchi et al. [138] drew opposite conclusions. They found good oxidation resistance behavior of Ti_5Si_3 up to 1250 ℃, which was attributed to the formation of an outer TiO_2 layer and inner SiO_2 layer. The oxidation behavior discrepancies were explained by slight variations of the Ti_5Si_3 composition and synthesis methods in those studies. Tang et al. [139, 140] proposed that N_2 increased the oxidation rate of Ti_5Si_3 in air above 1000 ℃. This is attributed to the formation of TiN preventing the formation of a continuous protective silica scale.

Accordingly, part of my research focuses on alloys containing (Mo, Ti, Si) + (Ti, Mo)$_5$Si$_3$ by eutectic reaction from the melt because of the reported good ductility, room fracture toughness of (Mo, Ti, Si) [69] as well as of the promising high temperature properties of (Ti, Mo)$_5$Si$_3$ [121, 138, 139, 141-143]. Besides this, the research is placed on the region of (Mo, Ti)$_3$Si in the liquidus projection as it is known to undergo the eutectoid decomposition of (Mo, Ti)$_3$Si → (Mo, Ti, Si) + (Mo, Ti)$_5$Si$_3$. Again, two phase alloys in this range may benefit from the ductility and room fracture toughness of (Mo, Ti, Si) as well as from the creep resistance of (Mo, Ti)$_5$Si$_3$ at high temperature [69, 102-104].

4 Experiments

All experimental methods and instruments used for the sample production, microstructure analysis, and creep and oxidation testing in this work are presented in this chapter.

4.1 Thermodynamic simulations

Pandat software can be used for the simulation and calculation of phase diagrams and thermodynamic properties of materials in multi-component systems. In this thesis, Pandat software with a database version PanMo_2014 delivered by from the technical support of Computherm LLCMadison, Wisconsin, USA was used. Phase diagram and isopleth sections, Scheil and lever-rule solidification simulations in the Mo-Si-Ti system were calculated. The architecture of Pandat software includes an interface layer, variety of calculation modules and robust database layer. In the operating process, a command could be generated by the toolbar. A database file from database layer could be selected and imported to the workspace. Afterwards, the option such as PanPhaseDiagram including phase diagram and thermodynamic property calculation provided a simulation and calculation for a workspace file. In this way, different tables and graphs could be generated and then exported into this thesis.

4.2 Sample production

4.2.1 Raw materials

Different high purity elements in the work were used as ingot materials including Mo, Si and Ti. Table 4.1 gives more details about the materials.

Table 4.1: Details about the elements used for arc melting

Element	Purity (%)	Shape	Size (mm)	Manufacturer
Mo	99.95	foil	0.5×100×200	CHEMPUR Feinchemikalien und Forschungsbedarf GmbH
Si	99.9999	lump	1-25	Alfa Aesar-A Johnson Matthey Company
Ti	> 99.5	granule	< 5	CHEMPUR Feinchemikalien und Forschungs-bedarf GmbH

4.2.2 Arc melting

With the arc melting method, materials which are easily oxidized or have high melting points can be produced under inert gas. The melting process can be done diametrically by the arc in a copper crucible.

In this work, an Edmund Bühler AM0.5 arc melting furnace, which includes several components such as high vacuum furnace, operating handle and cooling system, was employed to manufacture the alloys. In the high vacuum chamber, the operation with inert gas is possible up to 1.2 bar. On the operating handle, the current on/off switch is used to ignite on/off the arc, the maximum possible electrode current is 800A. The electrode up/down switch vertically moves the electrode upwards/downwards. The operating handle is used to horizontally control the electrode. In addition, a water cooling system is essential to decrease the temperature of the chamber.

Before the arc melting, different high purity elements were weighed to yield the nominal chemical composition and put together. Afterwards, these materials were melted in a water-cooled copper crucible with Ar atmosphere (99.998 % Ar) by non-consumable W electrode arc melting and solidified into a button ingot (of approximately 40 g per button in total). In order to obtain a homogeneous chemical composition and structure, the button should be turned to the reverse side by a tweezer mechanism and remelted. After repeating the whole process five times, the final button was gained with a diameter of about 30 mm and a thickness of about 10 mm. Furthermore, a Zr slug, which was in the side of the copper crucible during the sample preparation, was used to deplete residual oxygen before each melting step.

4.2.3 Heat treatment

Heat treatment was used to promote the eutectoid decomposition within the Mo-Si-Ti alloys in this work, because the decomposition is to slow for finishing during cooling in the arc melting. Two methods were used for heat treatment depending on the temperatures necessary. When temperatures are not higher than about 1250 ℃, silica glass tubes are used as containers. Before sealing, the glass tubes are evacuated using a turbo pump. This procedure allows comparably high cooling rates and less influence by the cooling regime on the microstructure evolution. The heat treatment process was operated in a Linn High Therm chamber furnace with the type of LM-312.07 at 1000-1250 ℃ for 100 or 200 hours in the specific experiments. In the second method, the samples are placed in a boat made from Al_2O_3 and then heat-treated under Ar atmosphere in a Gero tube furnace type HTRH 70-600/18. Compared with the first method, the second one has a slower cooling rate after heat treatment. However, the specific temperature and time for heat treatment were higher with 1300-1600 ℃ and up to 200 hours with the second method in this research.

4.3 Analysis of the microstructures

In order to analyze the microstructures and compositions of the alloys, flat and smooth specimens are necessary and were obtained by standard metallographic procedures. The specimens were ground and polished using a Bühler EcoMet 300 Pro equipped with an AutoMet 250. Specifically, for grinding, SiC papers were used successively with grit sizes P120 to P4000 with continuous water lubrication. For polishing, diamond polishing suspension with 3&1µm particle size was employed, with water-based lubrication. For removing deformation layers, final polishing was conducted combined mechanically-chemically using a stabilized oxide polishing suspension with particles of 25-40 nm size and pH=9.8 provided by Bühler.

Some parameters of the grinding and polishing are shown in Table 4.2.

Table 4.2: Parameters for grinding and polishing procedures in the metallographic preparation

Parameter	**Grinding**	**Polishing**	
Abrasive	SiC (P120, P320, P600, P1200, P2500 and P4000 grits)	diamond polishing paste(1μm, 3 μm)	OP-S
Time (min)	1 or 2 or until sample is plane and no scratch is present	≤ 5	≤ 5
Lubricant	continuous spray water	water-based	-
Head force (N)	40	20	20
Platen frequency (rpm)	300	150	150
Head frequency (rpm)	60	60	60
Head direction	opposite	opposite	opposite

4.3.1 Scanning Electron Microscopy

The microstructures of Mo-Si-Ti alloys were observed by scanning electron microscopy (SEM). In the SEM, electrons are generated by an electron gun and start to accelerate towards the anode. After passing through the anode, however, the electrons will diverge. Using one or more electron lenses, the electrons are focused to a relatively parallel electron beam. Then the electron beam is converged to a probe spot on the surface of the specimen, thus different signals including secondary electrons (SE) and backscattered electrons (BSE) will be excited from the specimen surface and finally captured by an electron collector. In this case, only the information of one single spot excited by the electron beam is obtained. Hence, the specimen must be scanned from top left to bottom right to form an SEM image. In particular, SE is excited under the specimen surface of a few nanometers, with energies of less than 50 eV [144]. BSE have greater depths than SE under the sample surface. Generally, the energy of the BSE is more than 50eV. SE and BSE signals are widely utilized to form images in the SEM [145, 146]. In general, SE is used for imaging to observe the topography of the sample. A BSE detector supplies compositional contrast, based on the strong correlation between the backscatter efficiency and the elemental mass. In this thesis, an instrument of SEM with the type of Zeiss Evo 50 was used to observe the microstructures of the materials by SE and BSE imagines.

In addition, phase areal fraction was calculated by analySIS pro software in this work based on the SEM images. Different phases show different brightness and contrast in the SEM images, hence the fraction of phases is easy to calculate by analySIS pro software in the Mo-Si-Ti samples. However, the fractions of eutectic and eutectoid regions are difficult to calculate by this method. In this work, a manual tool provided by the analySIS pro was used to draw the outlines of all the areas of the required microstructure. In this case, in order to reduce operational deviation, 6-10 SEM images with the 500x magnification in different regions were selected to obtain the average fraction of the microstructures in the alloys.

4.3.2 Energy Dispersive Spectroscopy

Chemical compositions of the alloys can be detected by energy dispersive spectroscopy (EDS) based on characteristic X-ray spectra produced by different elements induced by the electron beam within the SEM. X-radiation is detected by a Si (Lithium) drift detector. Through several components such as preamplifier and digital pulse processor, electron pairs resulting from the X-radiation are converted into digital pulses, whose heights are proportional to the detected X-ray energy. The pulses were classified and counted and finally generated X-ray spectra [93, 147, 148].

In this work, the element compositions of Mo-Si-Ti alloys were obtained by EDS with a Thermo Scientific NSS3 device together with the Zeiss Evo 50 SEM. For each sample, three or more regions were selected for EDS analysis to reduce the experimental deviation especially during the investigation of small features.

4.3.3 X-Ray Diffraction

X-ray diffraction (XRD) is an important tool which can be utilized widely to determine crystal structure present in the samples [149, 150]. Figure 4.1 shows the interactions between incident X-rays and the crystal structure of a material. When the incoming X-rays are diffracted, they need to satisfy Bragg's law for positive interference:

$$\sin\theta = n\lambda/2d \qquad (4.1)$$

where θ is half the angle between the incoming beam and the diffracted beam, n is diffraction order, λ is wavelength of incoming X-ray beam, d is the spacing between two parallel crystal planes that cause the reinforcement of the beam.

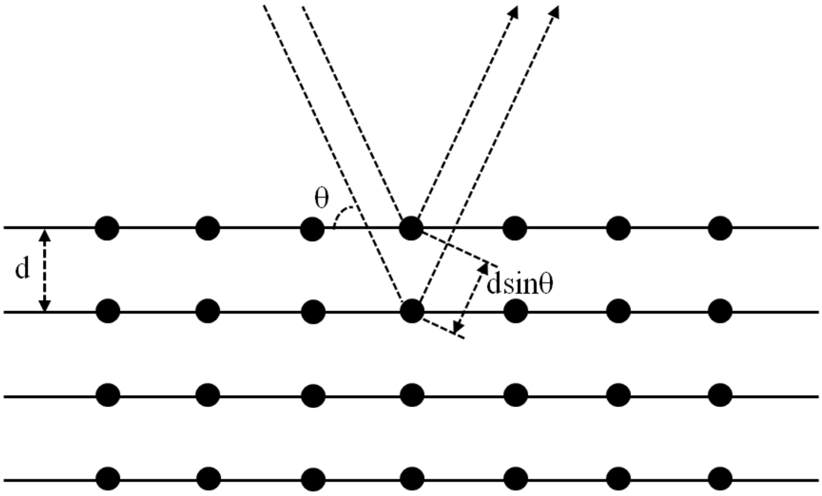

Figure 4.1: Schematic of Bragg's law [150]

A diffraction pattern can be created based on the crystal structure and lattice parameters of the materials. Different crystalline materials have distinct characteristic X-ray patterns. Hence, analyzing the XRD pattern can determine the phases present in the material. In this work, a diffractometer (Bruker D2 PHASER) together with Cu-Kα radiation and a LYNXEYE line detector were used to detect the characteristic diffraction patterns of the materials. The operating current and voltage are approximately 10 mA and 30 kV in the X-ray tube. The peaks in the diffraction pattern are analyzed by DIFFRAC.EVA software.

4.4 Creep Testing

For creep tests, the samples were cut using electrical discharge machining (with the dimensions of 3mm×3mm×5mm) and then ground with SiC paper to 2500 grit finish. Boron nitride spray was used for the samples as lubricant in order to reduce the friction between the samples and the testing machine.

The samples were loaded on a Zwick Z100 SW materials testing machine with central ball-lead screw with a high temperature Mo vacuum radiation furnace Maytec MSRA-81/P/RS-2 (Figure 4.2). In the machine, vacuum conditions were held at about 10^{-7} mbar. For the compression tests, the samples were tested at 1000 ℃-1300 ℃ and 50-200MPa.

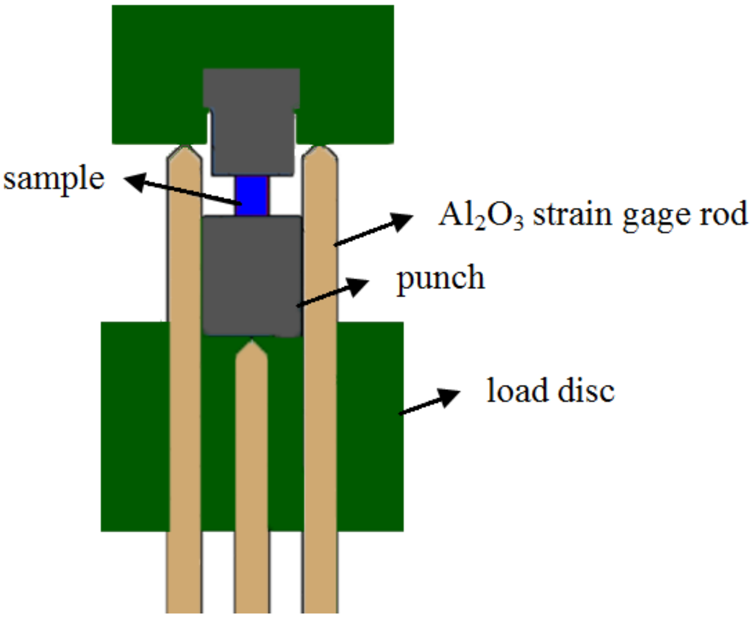

Figure 4.2: Schematic of strain measurement in compression [151]

4.5 Oxidation Testing

For oxidation tests, the samples were cut into a cube shape with the side length of 3 mm and a height of 2 mm by electrical discharge machining. The cut samples were then ground to 2500 grit with SiC paper and rinsed in ethanol. Before the oxidation tests, the samples were weighed and measured carefully and recorded their initial values of mass and area.

In the cyclic oxidation test, the samples were individually placed in alumina crucibles, and then were supported in a muffle furnace for 1 hour. After that, the samples were removed from the furnace and air cooled to room temperature with a cooling rate of 0.3-0.4 ℃/s, weighed and then again placed in the furnace for further oxidation. The cyclic oxidation tests were conducted in the temperature range of 800-1200 ℃.

Besides the cyclic oxidation test, constant-temperature oxidation tests were also conducted. In this research the constant-temperature oxidation test is achieved by thermogravimetric analysis (TGA). Specifically, the TGA test was performed at 800, 1100 and 1200 ℃ for durations of up to 100 h in flow synthetic air with N_2 and O_2 atmosphere (20.5 ±0.5 vol.% O_2) at 30K/min.

Major instruments used in the experiments are summarized in Table 4.3.

Table 4.3: List of major instruments used in experiments

Instrument	Type	Manufacturer
Arc melting furnace	AM0.5	Edmund Bühler
Tube furnace (HT)	HTRH 70-600/18	Carbolite Gero
Chamber furnace (HT)	LM-312.07	Linn High Therm
SEM	Zeiss Evo 50	Carl Zeiss AG
EDS	Thermo Scientific NSS3	Thermo Fisher SCIENTIFIC
XRD	Bruker D2 PHASER	Bruker

5 Results and Discussion

5.1 Eutectic microstructure in Mo-Si-Ti alloys

In this part, a suitable composition to obtain a eutectic microstructure of (Mo, Ti, Si) + $(Ti, Mo)_5Si_3$ is investigated by considering the primarily solidified phase, atomic phase fraction, crystallographic density and volume fraction according to the Pandat simulations and experimental observations.

5.1.1 Evaluation of Pandat simulations

Pandat simulations can be used for the composition selection of ternary alloys. In order to understand the applicability of Pandat for the present research, different compositions of Mo-Si-Ti alloys are chosen to investigate the relationship between simulation and the experimental observations. Their nominal compositions are summarized in Table 5.1 and displayed in Figure 5.1 in combination with the abbreviated forms used throughout this thesis. Specifically, E1, E2 and E3 alloys are located in a region of primarily solidified (Mo, Ti, Si), whereas E4 is in a region in which $(Ti, Mo)_5Si_3$ is the primarily solidified phase, E5 is located on the line where the eutectic microstructure should be obtained.

Table 5.1: Names and Nominal Compositions of Materials

Sample	Mo (at.%)	Si (at.%)	Ti (at.%)
E1	32.6	18.7	48.7
E2	26.4	19.1	54.5
E3	30.1	19.0	50.9
E4	25.4	23.1	51.5
E5	27.2	20.0	52.8

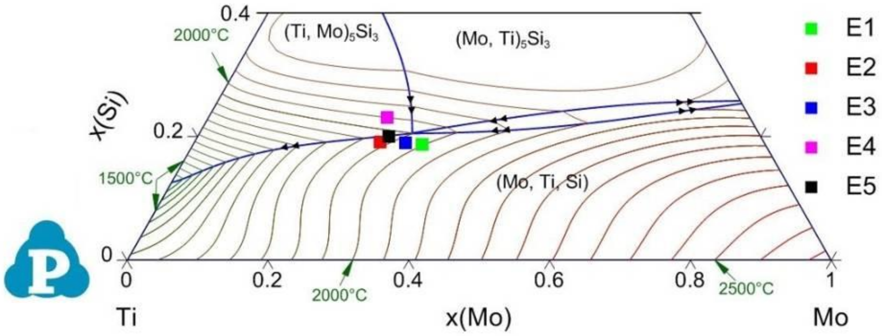

Figure 5.1: Liquidus projection of Mo-Ti-Si ternary system

The liquidus projection of Mo-Si-Ti ternary system shows the presence of the primary phase in different regions. However, specific solidification paths of the alloys are not completely described by the projected diagram. In this work, a non-equilibrium solidification Scheil model [152], under realistic rather than equilibrium conditions [153], is applied to calculate the solidification sequence of Mo-Si-Ti alloys. In this model, it is assumed that no diffusion occurs in the solid phases. By contrast, diffusion is considered infinitely fast in the liquid phase, and the phase equilibrium can be obtained in a local interface between liquid and solid phases. Furthermore, phase equilibrium at the interface is calculated by Pandat using the average composition of the remaining liquid in the current time step as the overall liquid composition in the next time step. In the Scheil model, it is assumed that there is no diffusion in the solid phase but an infinite diffusion in the liquid phase, thus the liquid composition follows the equilibrium liquidus line of the phase diagram, while the solid composition deviates from the solidus line. Because the eutectic reaction primarily requires diffusion in the liquid, Scheil's equation provides a more realistic model of the solidification path than the equilibrium model.

Figure 5.2 shows the Scheil solidification simulation of E1-E4. At first, (Mo, Ti, Si) phase is formed from the liquid in E1-E3 within a temperature interval of ~50K. The eutectic reaction of L → (Ti, Mo)$_5$Si$_3$ + (Mo, Ti, Si) then occurs. When the temperature decreases by about 600K, the eutectic reaction is almost finished. By contrast, in the solidification path of E4, the primary solidified phase is (Ti, Mo)$_5$Si$_3$. Then the eutectic microstructure of (Ti, Mo)$_5$Si$_3$ + (Mo, Ti, Si) is formed by the eutectic reaction of L → (Ti, Mo)$_5$Si$_3$+ (Mo, Ti, Si).

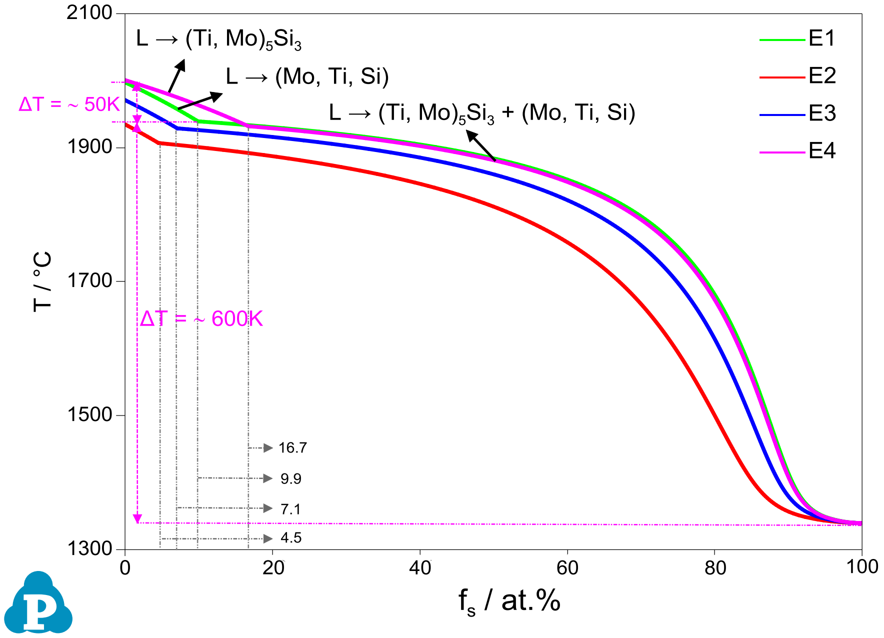

Figure 5.2: The simulations of Scheil solidification paths for alloys E1-E4

Figure 5.3 (a-c) shows that the backscattered electrons images of E1-E3 indicate two different phases. A white dendritic phase surrounded by the eutectic microstructure is the primary solidified phase. As shown in Figure 5.4 (a), the atomic fractions of Si in (white) primary phases of the three alloys are about 3.8-4.4 at.%, which are in good agreement with the solubility of Si in (Mo, Si) based on the Mo-Si binary phase diagram (Si solubility is less than 5 at.%) [73]. Likewise, Ti is also detected with significant amounts in all three alloys, which indicates that the white primary phases of E1-E3 are (Mo, Ti, Si). By contrast, as shown in Figure 5.3 (d), the first solidifying phase of E4 is a black phase with a hexagonal plate morphology, which is surrounded by the eutectic microstructure. EDS indicate that the (atomic) element ratio between Si and the other two species (Mo and Ti) is 0.54:1 (Figure 5.4 (b)), which is close to the stoichiometric ratio (0.6:1) in Ti_5Si_3 or Mo_5Si_3. Hence, the black primary phase in E4 can probably be (Ti, Mo)$_5$Si$_3$ or (Mo, Ti)$_5$Si$_3$. Verification of (Ti, Mo)$_5$Si$_3$, as it is suggested by Pandat simulations, and falsification of (Mo, Ti)$_5$Si$_3$ will be provided based on XRD later in this chapter.

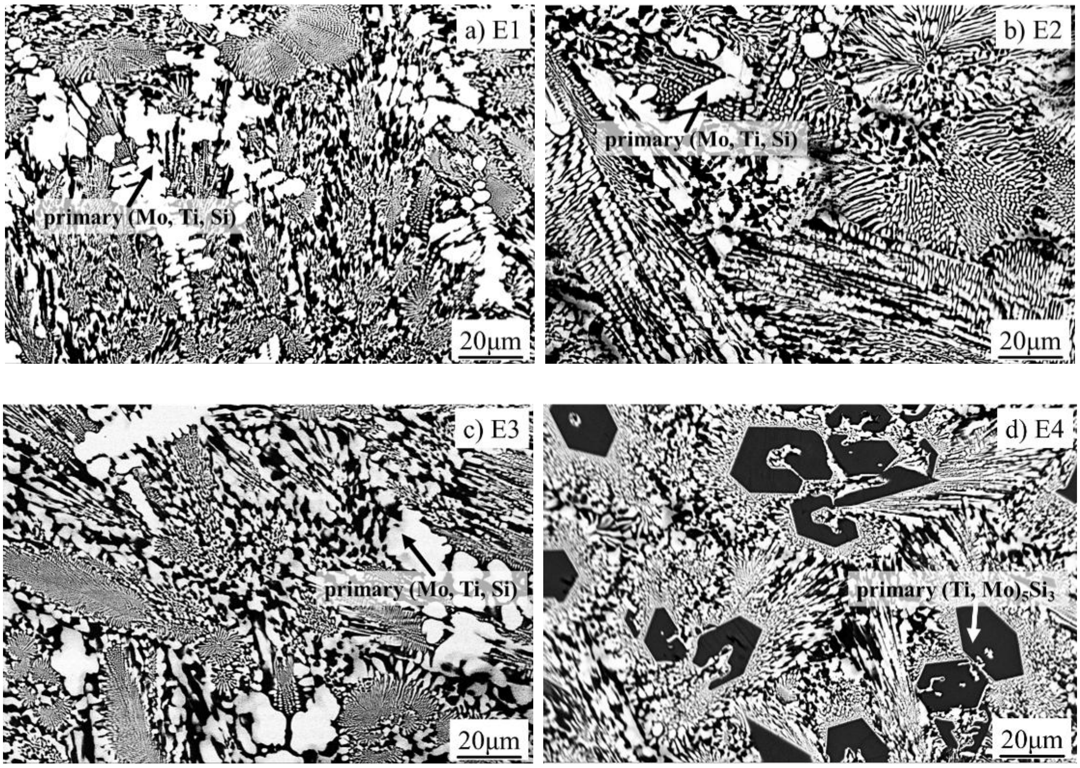

Figure 5.3: SEM images (BSE contrast) of the investigated alloys in as-cast conditions

Moreover, the atomic phase fractions of the primary phases of alloys E1-E4 were calculated. Specifically, the atomic phase fractions X_p of different elements in primary phases from E1 to E4 can be expressed with the following formula:

$$X_p = \frac{X - f_l \cdot X_l}{f_p} \tag{5.1}$$

where X is the composition of each element in the alloy (Table 5.1); f_p is the atomic fraction of primary phase; f_l is the atomic fraction of the liquid when the primary phase solidification just finished; X_l is the concentration of each element in the liquid fraction when the primary phase solidification just finished. The respective values are shown in Table 5.2.

Figure 5.4 shows the composition of the primary phases in E1-E4 calculated with Pandat in comparison to experimental results by EDS. It is found that the Si contents in the primary phase of E1-E3 agree well between the Pandat calculations and the EDS measurements. However, the Ti contents in E1-E3 determined by EDS are significantly higher than that suggested by Pandat. This is probably because Ti and Mo can substitute each other in the primary (Mo, Ti, Si), resulting in the change of the concentration of Ti in (Mo, Si, Ti). Yang et al. [131, 132, 154] reported that Ti substituted for Mo, leaving the Si concentration unaffected, in which the solubility of Ti in Mo solid solution is as high as 35 at.% in Mo37.5-Ti18-Si9B [154]. By contrast, the composition of primary (Ti, Mo)$_5$Si$_3$ in E4 is appropriately predicted by Pandat.

Table 5.2: Relevant parameters of primary phases based on Pandat

Primary Phase		***M*** **(g/mol)**	**X_p (at.%)**	**X_l (at.%)**	**f_p (at.%)**	**f_l (at.%)**
E1	**Mo**	95.95	66.4	28.9	9.9	90.1
	Si	28.09	4.0	20.3		
	Ti	47.87	29.6	50.8		
E2	**Mo**	95.95	63.2	24.7	4.5	95.5
	Si	28.09	3.8	19.8		
	Ti	47.87	33.0	55.5		
E3	**Mo**	95.95	65.3	27.4	7.1	92.9
	Si	28.09	4.0	20.2		
	Ti	47.87	30.7	52.4		
E4	**Mo**	95.95	13.2	27.8	16.7	83.3
	Si	28.09	37.5	20.2		
	Ti	47.87	49.3	52.0		
E5	**Mo**	95.95	65.0	27.0	0.5	99.5
	Si	28.09	3.9	20.1		
	Ti	47.87	31.1	52.9		

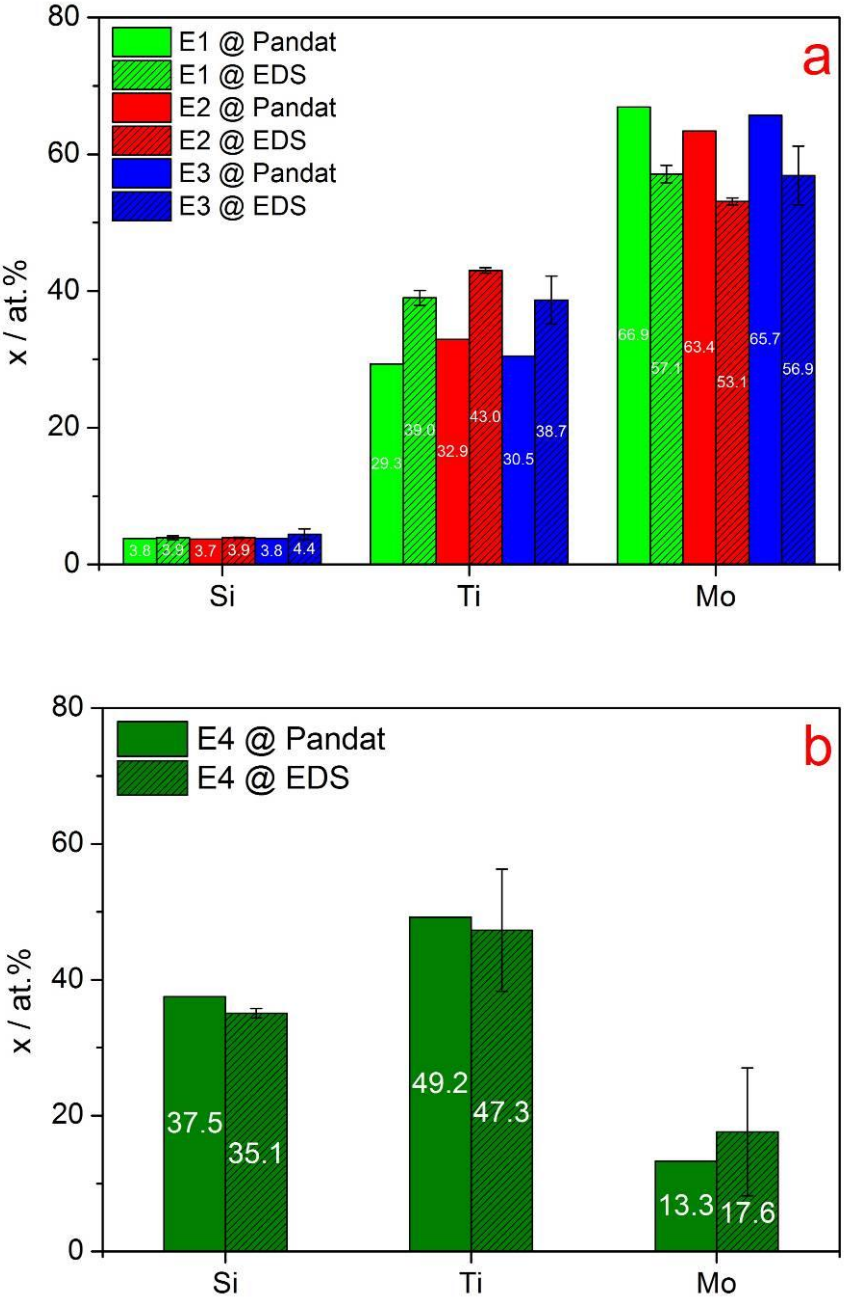

Figure 5.4: The atomic fractions of the primary phases of alloys E1-E4: comparison of Pandat and EDS results

XRD is further employed to verify the phases in E1-E4. As shown in Figure 5.5, some peaks correspond to that of Mo solid solution with BCC crystal structure, namely 2θ of 40.52 ° {110}, 58.61 ° {120}, 73.68 ° {117}, 87.60 ° {121}, 101.41 ° {122} and 115.97 ° {123} (pattern No. PDF 42-1120). Because of the presence of Ti and Si, the diffraction peaks in E1-E4 are shifted to lower 2θ values in comparison to pure Mo. Moreover, the peaks of (Ti, Mo)$_5$Si$_3$ are observed with the main 2θ of 35.54 ° {116}, 37.25 ° {320}, 38.35 ° {210} and 42.18 ° {100} (pattern No. PDF 29-1362), while the peaks of (Mo, Ti)$_5$Si$_3$ with 2θ angles of 60.64 ° {620} and 70.09 ° {413} are not found. These results demonstrated that the phase in E1-E4 is (Ti, Mo)$_5$Si$_3$, but not (Mo, Ti)$_5$Si$_3$.

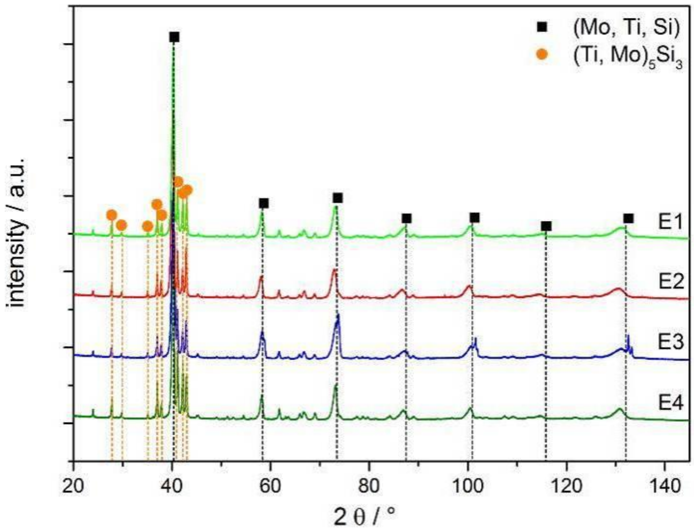

Figure 5.5: XRD patterns of alloys E1 to E4

In order to evaluate the observed volume fraction of the primary phase in the investigated alloys, a conversion of the atomic phase fraction to volumetric phase fraction is necessary. For this mean molecular weights and densities of the phases have to be obtained.

The crystallographic density ρ of the participating phases is calculated by means of (see also Appendix Table 8.1):

$$\rho = \frac{nM}{N_A V} \tag{5.2}$$

where n is the number of atoms/unit cell; M is the mean atomic weight; N_A is the Avogadro number (6.02 ×10^{23}(mol^{-1})); V is the volume of a unit cell. M is determined based on the composition of the phases suggested by the Pandat simulations (Table 5.2 & Figure 5.4)

The volume fractions of the primary phases can be calculated as follows:

$$V_p = \frac{W_p/\rho_p}{W_p/\rho_p + W_e/\rho_e} = \frac{W_p/\rho_p}{W_p/\rho_p + W_l/\rho_e} = \frac{W_p \rho_e}{W_p \rho_e + W_l \rho_p} \tag{5.3}$$

where V_p is the volume fraction of the primary phase; ρ_e is the crystallographic density of eutectic microstructure; W_p is the weight fraction of the primary phase; W_l is the weight fraction of liquid when the solidification of the primary phase is just finished. In the equ. 5.3, the weight fraction of the eutectic microstructure W_e is replaced by the weight fraction of liquid W_l. This is because after the solidification of the primary phase, the liquid begins to translate into the eutectic microstructure. Therefore, the weight fraction of liquid W_l can be considered the same as the weight fraction of the eutectic microstructure W_e.

According to the Delesse-principle, the areal fraction calculated from SEM images is set equal to the volume fraction in the experimental results [155]. The volume fractions of primary phases in E1-E4 according to the prediction of Pandat are shown in Table 5.3. The comparison of the volume fractions of different alloys between experiment and simulation results is displayed in Figure 5.6. It is found that a good agreement between experimental results and Pandat calculations is observed in E1-E4.

Table 5.3: Relevant parameters of primary phases in E1-E5

Primary phase	W_p *(wt.%)*	W_l *(wt.%)*	ρ_p *(g/cm^3)*	ρ_e *(g/cm^3)*	V_p *(vol.%)*	V_e *(vol.%)*
E1	13.1	86.9	8.45	6.42	10.3	89.7
E2	6.2	93.8	8.27	6.09	4.6	95.4
E3	9.5	90.5	8.38	6.29	7.3	92.7
E4	14.1	85.9	5.07	5.97	16.2	83.8
E5	0.3	99.7	8.35	7.46	2.1	97.9

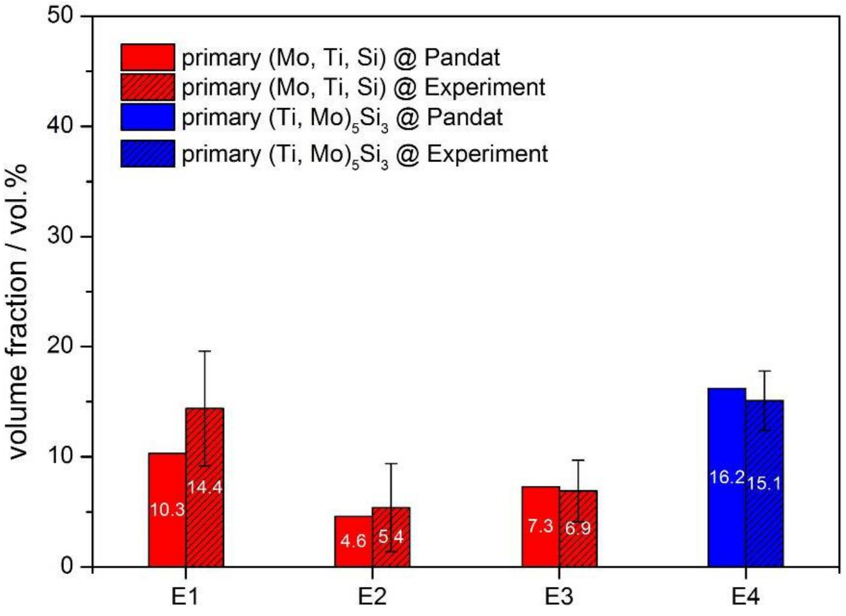

Figure 5.6: Volume fractions of primary phases in E1-E4 between the simulation and the experimental results

Therefore, after a series of analyses including SEM, EDS and XRD, it is confirmed that the experimental results are corresponding to the thermodynamic calculations and solidification paths according to Pandat: this is valid with respect to the Si compositions and to the volume fractions of the primary phases. By contrast, the Ti contents of the primary phases in the EDS results are higher than those given by Pandat, which is probable attributed to the substitution of Mo by Ti.

5.1.2 Determination of a suitable eutectic composition

According to the analysis of the Pandat simulation and the experimental observation, the eutectic microstructure can be obtained when a composition on the eutectic through enclosed by the compositions of E1-E4 are chosen. With the consideration of the measurement deviation and experimental operability, Mo27.2-Si20.0-Ti52.8 (abbreviated as E5) is selected (Figure 5.1).

Figure 5.7 shows the E5 Scheil simulation sequence, and as expected a eutectic microstructure of (Mo, Ti, Si) + (Ti, Mo)$_5$Si$_3$ is present in the sample. It can also be found that the temperature interval for which the entire material is solidified is about 600K.

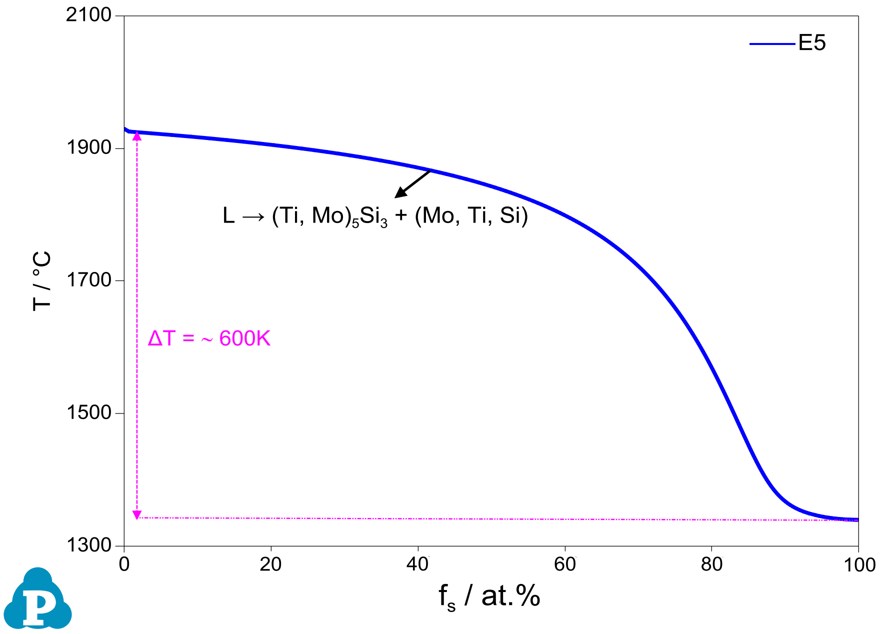

Figure 5.7: Scheil simulation of the solidification path of alloy E5

Eutectic microstructure with colony morphology in X5 can be found in Figure 5.8, which consists of the solid solution phase (Mo, Ti, Si) and (Ti, Mo)$_5$Si$_3$ as demonstrated by XRD results (Figure 5.9). It is difficult to calculate the content of eutectic microstructure by analySIS pro software, therefore the volume fractions of the primary phase in E5 are calculated. The results show that E5 has a small amount of primary phase (about 3.9 vol.%), suggesting that the composition of the eutectic microstructure is > 96 vol.%. Hence, E5 can be considered as the desired eutectic microstructure.

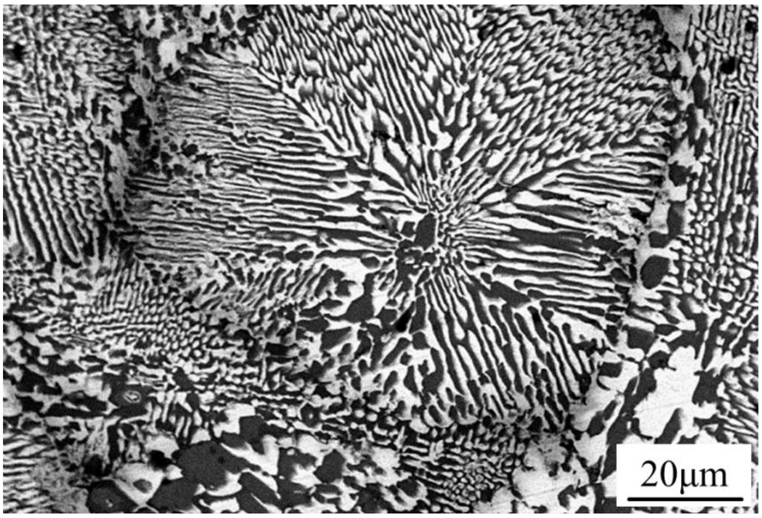

Figure 5.8: SEM image (BSE contrast) of alloy E5

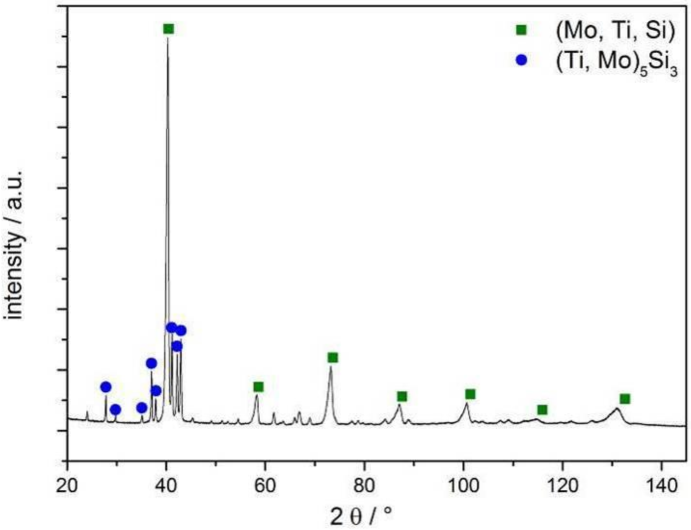

Figure 5.9: XRD pattern on alloy E5

5.1.3 Conclusions

Four different alloys designated E1-E4, which are located in a region that primary solidified (Mo, Ti, Si) and (Ti, Mo)$_5$Si$_3$, are selected to analyze whether the results of thermodynamic simulations by Pandat are corresponding to the experimental results. After a series of analysis including determining the compositions and volume fractions of the primary phases, it is confirmed that the compositions of Si and the volume fractions of the primary phases are well predicted by the thermodynamic calculations. The found compositions of Ti in EDS results are higher than those predicted by Pandat, which is probably attributed to the substitution of Mo by Ti.

According to the analysis of the Pandat simulation and the experimental observation, alloy E5 (Mo27.2-Si20.0-Ti52.8) was selected to show a eutectic microstructure. Indeed, E5 exhibits a eutectic microstructure of (Mo, Si, Ti) and (Ti, Mo)$_5$Si$_3$, and its volume fraction in E5 is up to 96.1 vol.%. Hence, E5 is considered as a desired eutectic microstructure.

5.2 Eutectoid microstructure in Mo-Si-Ti alloys

In order to obtain a fully eutectoidically decomposed microstructure, a two-step process should be applied: first, (Mo, Ti)$_3$Si phase has to be solidified from the liquid; then these samples should be subjected to a high temperature treatment since the kinetics to conduct the eutectoid decomposition of (Mo, Ti)$_3$Si → (Mo, Ti, Si) + (Mo, Ti)$_5$Si$_3$ may be slow. In this part, a suitable composition for the formation of eutectoid microstructure in Mo-Si-Ti alloy is investigated, and the related mechanisms are systematically analyzed.

5.2.1 The formation of (Mo, Ti)$_3$Si phase

Figure 5.10 shows again the liquidus projection of the Mo-Si-Ti ternary phase diagram (similarly to Figure 5.1, but here emphasis is placed on the eutectoid region). Because the formation of (Mo, Ti)$_3$Si phase is the first step to obtain the eutectoid microstructure, the compositions of the investigated alloys in Mo-Si-Ti system should locate in the single phase region of (Mo, Ti)$_3$Si. Hence, Mo58-Si25-Ti17 abbreviated as X1 is chosen as the first candidate based on the liquidus projection suggestion. This is because X1 has the highest melting point in the region of (Mo, Ti)$_3$Si (Figure 5.11). From that it is anticipated that a high thermal stability and a narrow solidification interval (< 5K) can be obtained. In addition, two compositions (abbreviated as X2 and X3) of Mo-Si-Ti alloys are also selected as an optimization of the eutectoid microstructure. The nominal compositions of alloys are summarized in Table 5.4 in combination with the abbreviated forms used throughout this thesis.

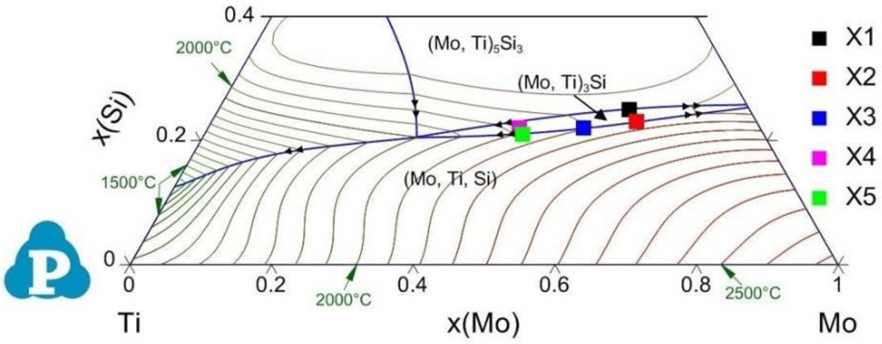

Figure 5.10: Mo-Ti-Si partial ternary system of liquidus projection

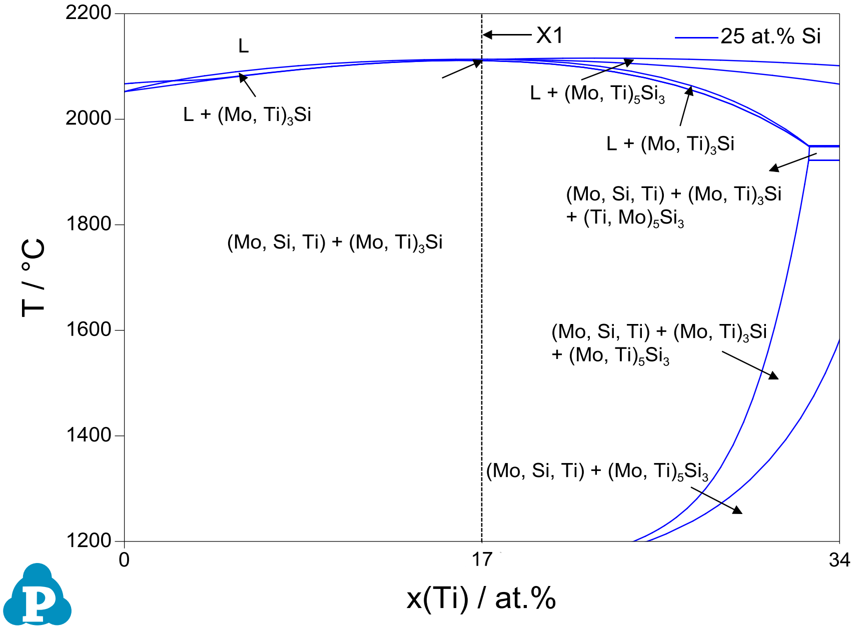

Figure 5.11: Vertical section of the ternary phase diagram with 25 at.% Si

Table 5.4: Nominal Compositions and Abbreviation of Selected Alloys

Sample	Mo (at.%)	Si (at.%)	Ti (at.%)
X1	58	25	17
X2	60	23	17
X3	53	22	25
X4	44	22	34
X5	45	21	34

Figure 5.12 shows a vertical section of the ternary phase diagram for X1. Above 2000 ℃, (Mo, Ti)$_3$Si phase is firstly formed, and then the eutectoid decomposition of (Mo, Ti)$_3$Si → (Mo, Ti, Si) + (Mo, Ti)$_5$Si$_3$ occurs. Hence, it is considered that eutectoid microstructure (Mo, Ti, Si) + (Mo, Ti)$_5$Si$_3$ can be obtained from X1.

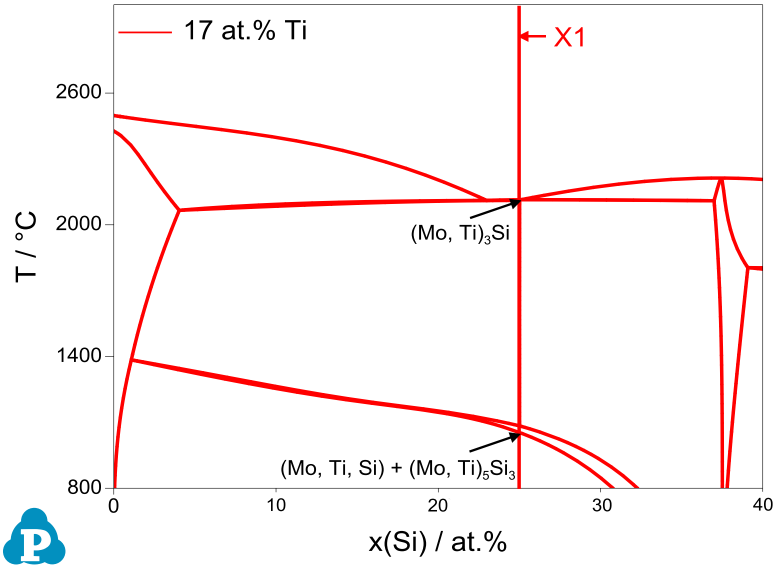

Figure 5.12: Vertical section of the ternary phase diagram for X1 and 17 at.% Ti

As shown in the backscatter electron image of Figure 5.13 (a), the microstructure of X1 consists of a large-scale light dendritic phase, which is surrounded by a dark residual phase at the dendrite boundaries. In order to determine the different phases, the sample was analyzed by EDS. As shown in Figure 5.14, the concentration of Si in the light phase is about 23 at.%, which is lower than the suggested 25 at.% according to the stoichiometry of Mo_3Si. This might be attributed the Si vacancies and atomic replacement between Mo and Si in Mo_3Si [156]. In fact, Rosales et al. [97] found that Mo_3Si is not a stoichiometric compound, and the concentration of Si in single-phase Mo_3Si is rather near 24 at.%. Also, Ti could play an important role in changing the (Mo, Ti)$_3$Si phase stability region. In this case, the light dendritic phase in X1 is speculated to be (Mo, Ti)$_3$Si. It is worth noting that the concentration of Si in the fringes (22.6 at.%) is almost the same as the Si content in the dendrites being 22.9 at.%. Thus, the fringe phase is also (Mo, Ti)$_3$Si. However, the concentration of Ti in the fringes (20.3 at.%) is higher than that of the Ti in the dendrites (14.3 at.%), indicating the segregation of Ti into the fringe areas. This may be due to the substitution of Mo by Ti. As reported by Yang et al. [132], the solubility of Ti in Mo_3Si could be as high as 30 at.% and the substitution between Ti and Mo occurred. Moreover, the residual phase is considered to be (Mo, Ti)$_5$Si$_3$ or (Ti, Mo)$_5$Si$_3$. This is because the concentration of Si in the dark residual phase is 35.9 at.% (Figure 5.14), which is close to the 37.5 at.% Si of the stoichiometric Mo_5Si_3/Ti_5Si_3 phases.

In order to further determine the specific phases, XRD patterns of X1 are displayed in Figure 5.15, in which the peaks of (Mo, Ti)$_3$Si phase are clearly detected, namely the relatively strong peaks with 2θ of 36.67 ° {200}, 41.19 ° {210}, 45.33 ° {211}, 69.10 ° {320}, 92.25 ° {421}and 115.79 ° {432} (pattern No. PDF 51-0764). Because of the presence of Ti, the diffraction peaks of (Mo, Ti)$_3$Si are shifted to slightly lower 2θ values. Furthermore, a small amount of (Mo, Ti)$_5$Si$_3$ diffraction peaks are also observed, namely 2θ of 27.49 ° {211}, 38.27 ° {321}, 42.76 ° {411}and 77.72 ° {004} (pattern No. PDF 34-0371).

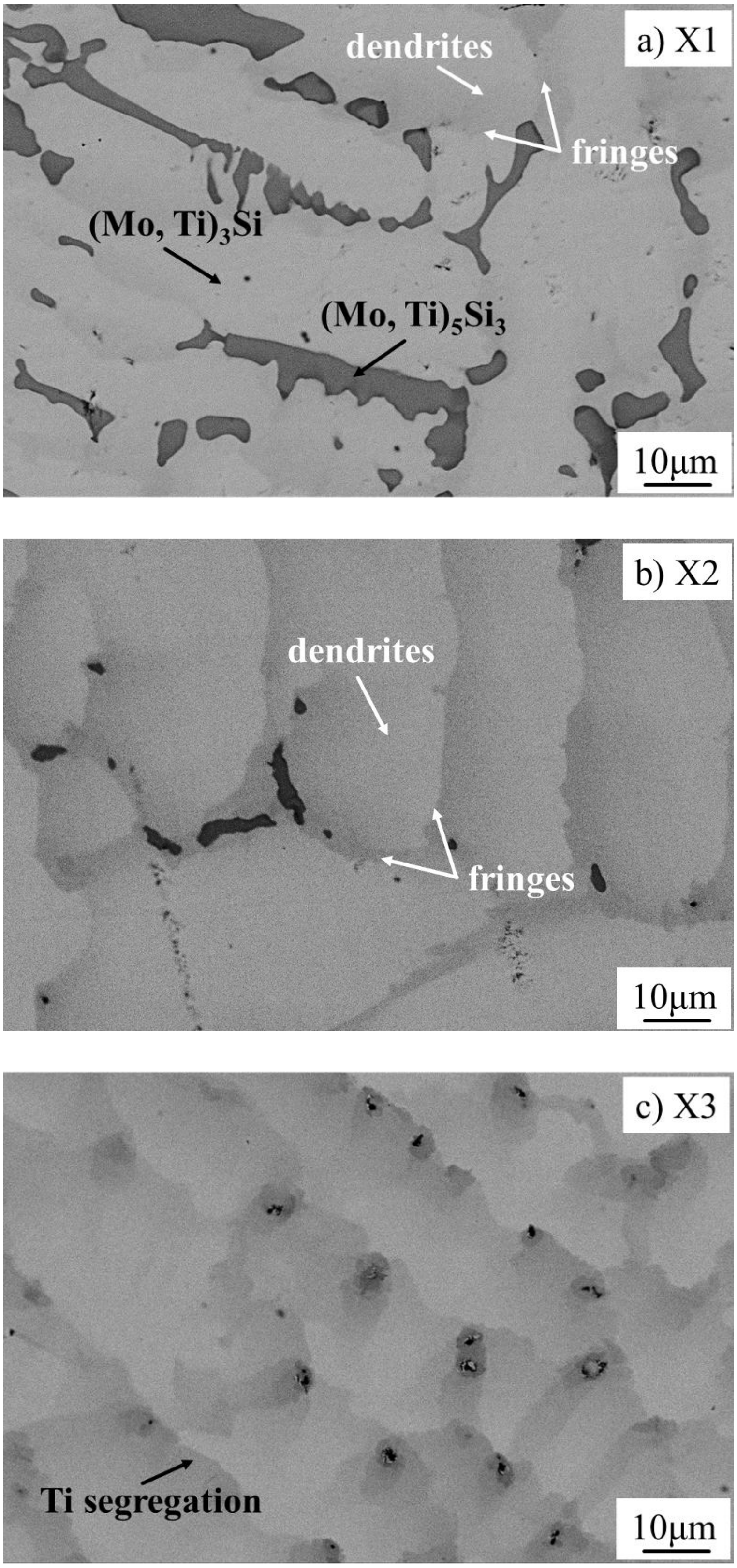

Figure 5.13: Back scattered images of the X1-X3 as-cast microstructures

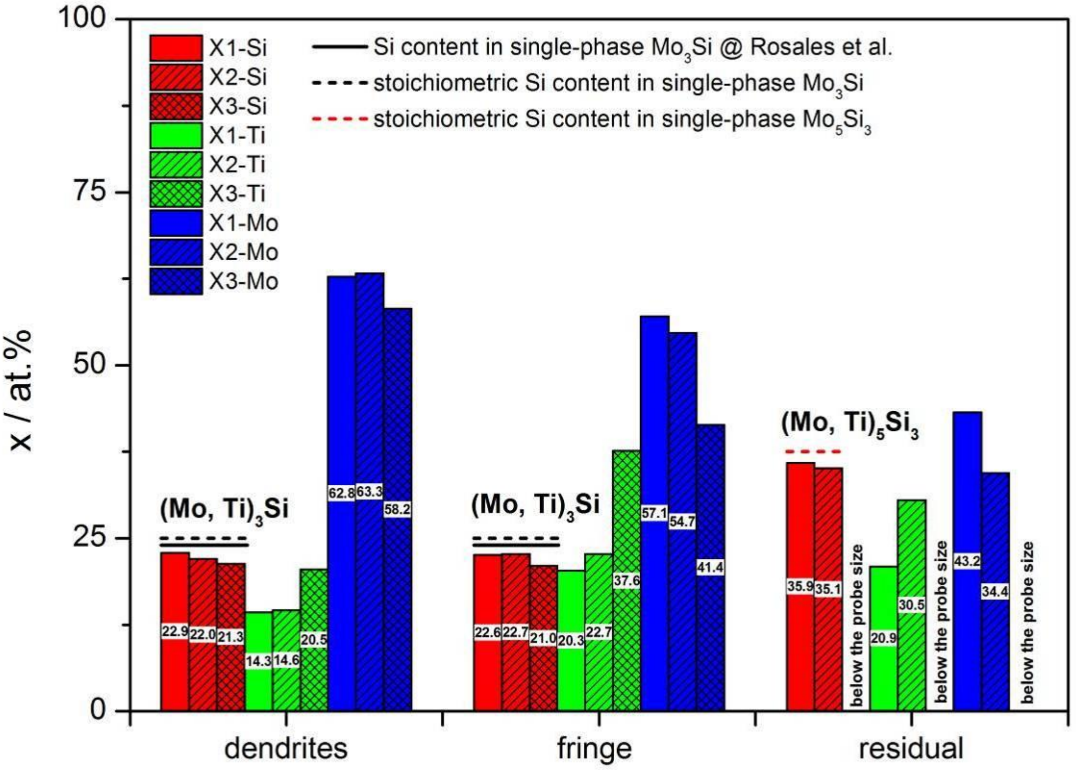

Figure 5.14: The atomic phase fractions of the different regions of alloys X1-X3 with EDS results

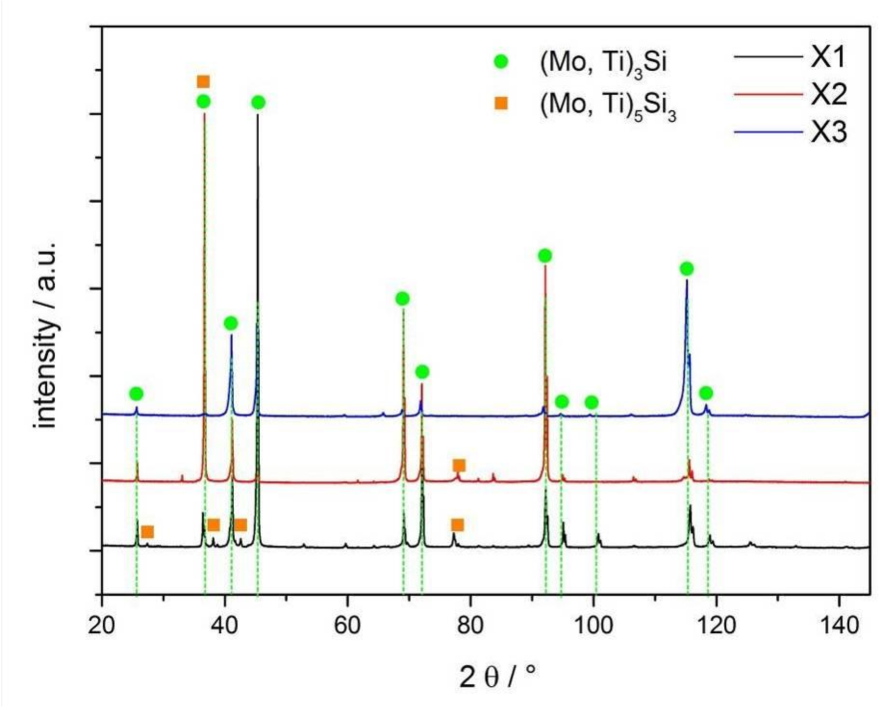

Figure 5.15: XRD patterns of alloys X1-X3

Although Pandat suggests the existence of single-phase (Mo, Ti)$_3$Si in X1, a residual (Mo, Ti)$_5$Si$_3$ is also found in the specimen in this research. The EDS result for the dendritic phase (Mo, Ti)$_3$Si implies that it is possible to obtain (Mo, Ti)$_3$Si phase with about 23 at.% Si (Figure 5.14), which was used for determing the composition of alloy X2. However, the SEM image of X2 (Figure 5.13 (b)) reveals that there is still some residual (Mo, Ti)$_5$Si$_3$, whereas its content is significantly reduced. EDS analysis shows that the concentration of Si decreases to 22 at.% in the (Mo, Ti)$_3$Si phase (Figure 5.14). Thus, X3 with 22 at.% Si is selected for further research. The analysis of the microstructure of X3 reveals that now the whole area is covered with the (Mo, Ti)$_3$Si phase. The remaining dark residual particles in the SEM image are difficult to analyze by EDS due to the large probe size of EDS (Figure 5.14).The other parts are considered as (Mo, Ti)$_3$Si with the composition of Si 21.3 at% in the dendrites and 21 at% in the fringe. Therefore, X3 is considered as the expected “eutectoid” alloy which has the (Mo, Ti)$_3$Si phase in almost the entire microstructure.

5.2.2 Determination of a suitable eutectoid composition

As described above, X3 is considered as the expected alloy which has the (Mo, Ti)$_3$Si phase. Hence, a heat treatment of X3 should be conducted to obtain suitable eutectoid microstructures. Figure 5.16 shows the microstructures of X3 after heat treatments in the range from 1000 ℃ to 1600 ℃ for 100h. A fine eutectoid microstructure is observed at the dendrite boundaries of (Mo, Ti)$_3$Si phase at 1000 ℃. With the increase of the heat treatment temperature, the eutectoid microstructure increases in volume at the dendrite boundaries. Particularly, at 1300 ℃ the eutectoid microstructure strongly increases and begins to coarsen. However, the content of eutectoid microstructure decreases at even higher heat treatment temperatures (1400 ℃-1600 ℃). There almost no eutectoid microstructure is present in the samples at 1500 ℃ and 1600 ℃, and only rod-like and spherical-like phases are present. Overall, the eutectoid decomposition is significantly affected by the heat treatment temperature, and the most suitable condition for heat treatment is 1300 ℃ for 100h, although there is no complete eutectoid microstructure in X3. In addition, the eutectoid microstructure is present in the region where Ti segregates. No Ti segregation is found at 1500 ℃-1600 ℃, the eutectoid microstructure is also not formed at these temperatures. Hence, Ti segregation also plays an important role in the eutectoid decomposition.

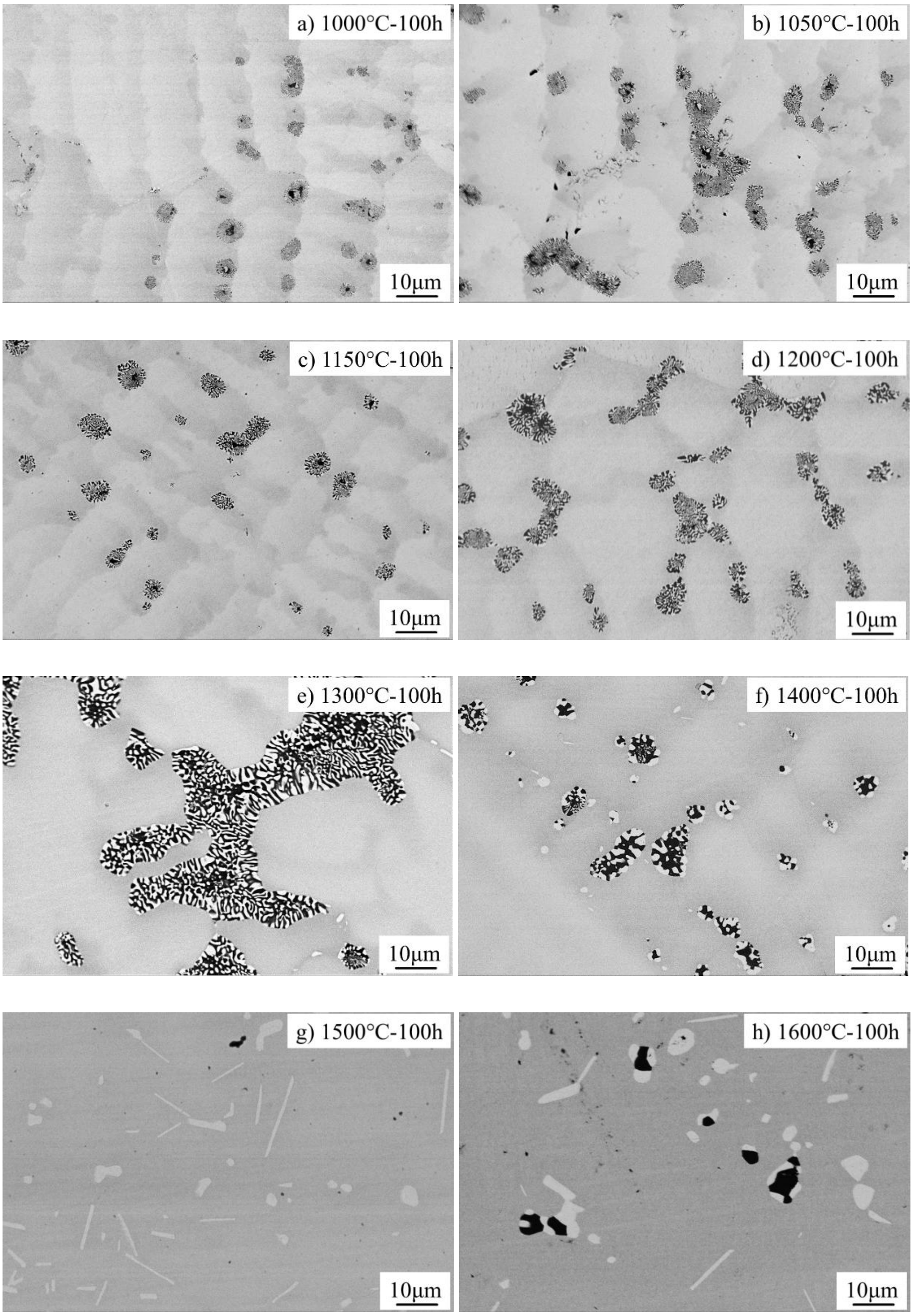

Figure 5.16: SEM image of X3 at different heat treatment temperatures from 1000 ℃ to 1600 ℃ for 100h

In order to increase the content of eutectoid microstructure, a new composition should be selected. In X3, because of the segregation of Ti, the eutectoid decomposition is formed at the dendritic boundaries.

Hence, the effect of Ti concentration on the eutectoid decomposition is investigated with Pandat. As shown in Figure 5.17, 22 at.% Si and 1300 ℃ based on the Si composition and heat treatment temperature of X3 are set up to calculate the phase fractions. With the increase of Ti concentration from ~26 at.% to ~27 at.%, (Mo, Ti)$_3$Si phase significantly decreases, (Mo, Si, Ti) and (Mo, Ti)$_5$Si$_3$ begin to simultaneously increase, suggesting that the eutectoid decomposition of (Mo, Ti)$_3$Si → (Mo, Si, Ti) + (Mo, Ti)$_5$Si$_3$ occurs. However, when the Ti content reaches ~35 at.%, the (Ti, Mo)$_5$Si$_3$ phase is found (purple vertical line in Figure 5.17). Therefore, in order to get the eutectoid microstructure of (Mo, Si, Ti) + (Mo, Ti)$_5$Si$_3$, the composition of Ti should be lower than 35 at.%. Thus, 34 at.% Ti and 22 at.% Si are considered as a new composition named X4 (Figure 5.18).

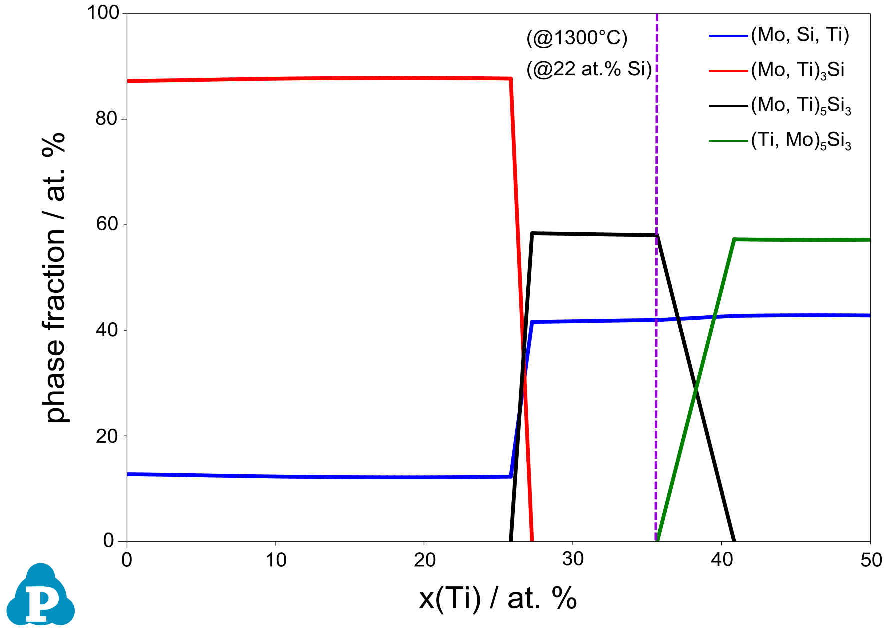

Figure 5.17: Calculated fractions of phases with 22 at.% Si at 1300 ℃

Compared with as-cast X3 with 25 at.% Ti (Figure 5.13 (c)), the eutectoid decomposition of X4 is strongly promoted by the increasing Ti at the dendrite boundaries, and the amount of eutectoid microstructure significantly increases (Figure 5.18). Residual (Mo, Ti)$_5$Si$_3$ is observed by EDS (Figure 5.19) and XRD analyses (Figure 5.20). Notably, the content of Si in the (Mo, Ti)$_3$Si is about 21 at.% in the dendritic phase. Therefore, a new alloy X5 with the Si content of 21 at.% is selected for the elimination of the residual (Mo, Ti)$_5$Si$_3$.

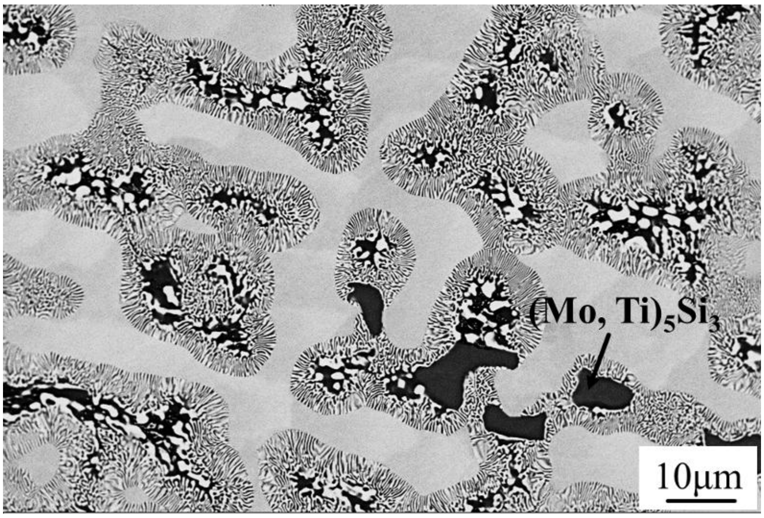

Figure 5.18: SEM image (BSE contrast) of alloy X4

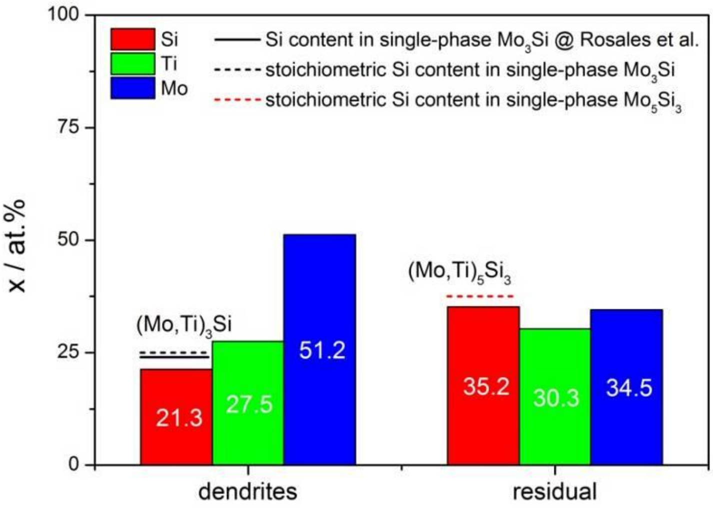

Figure 5.19: EDS column diagram of alloy X4

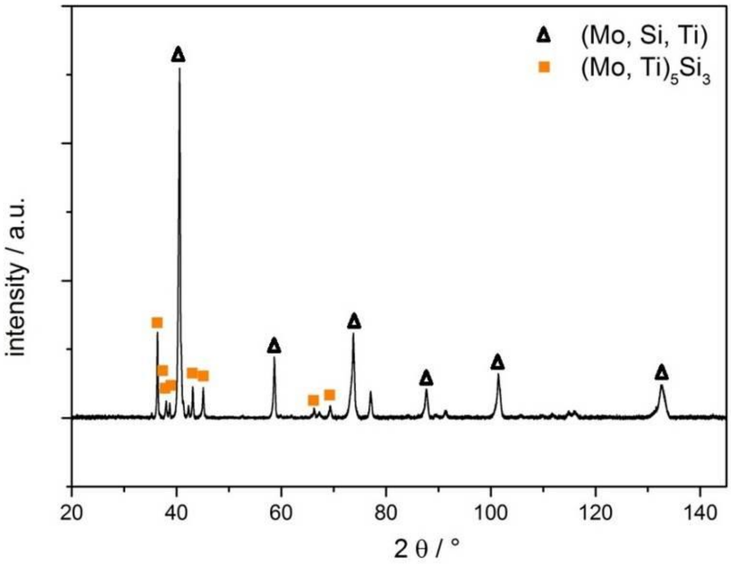

Figure 5.20: XRD pattern on alloy X4 after annealing at 1300 ℃ for 200h

Figure 5.21 shows the microstructure of X5. A fine eutectoid microstructure consisting of (Mo, Ti, Si) + (Mo, Ti)$_5$Si$_3$ distributes at the dendrite boundaries of (Mo, Ti)$_3$Si phase. Moreover, no primary phase is found in the sample. Therefore, it is possible to obtain a suitable eutectoid microstructure after a subsequent heat treatment.

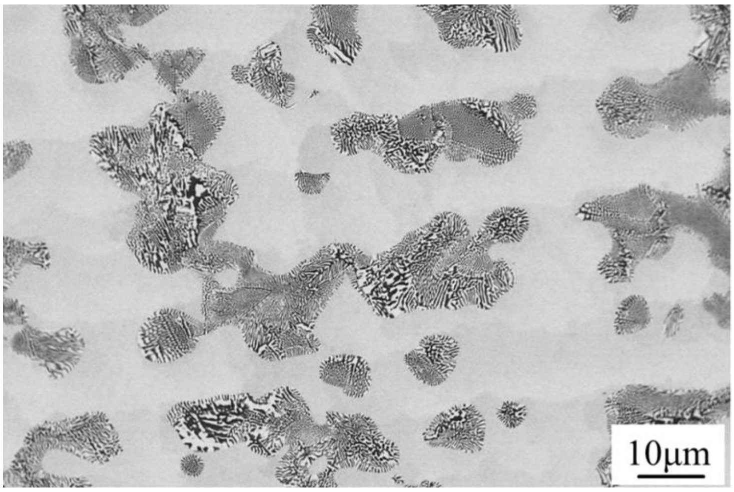

Figure 5.21: Back scattered image of the as-cast microstructure of alloy X5

With the results of X3 during heat treatment, the temperatures of heat treatment in X5 are selected in the range 1200 ℃-1300 ℃. Figure 5.22 (a) shows that the sample contains a two-phase (Mo, Ti, Si) + (Mo, Ti)$_5$Si$_3$ eutectoid microstructure at 1200 ℃ for 100 h. However, (Mo, Ti)$_3$Si is still present in the annealed alloy. Figure 5.22 (b-d) demonstrate that at the higher temperatures and longer times, more eutectoid microstructure is produced. Meanwhile, the content of (Mo, Ti)$_3$Si gradually decreases. Finally, an almost complete eutectoid microstructure of (Mo, Ti, Si) + $(Mo, Ti)_5Si_3$ is present by the heat treatment condition at 1300 ℃ for 200h.

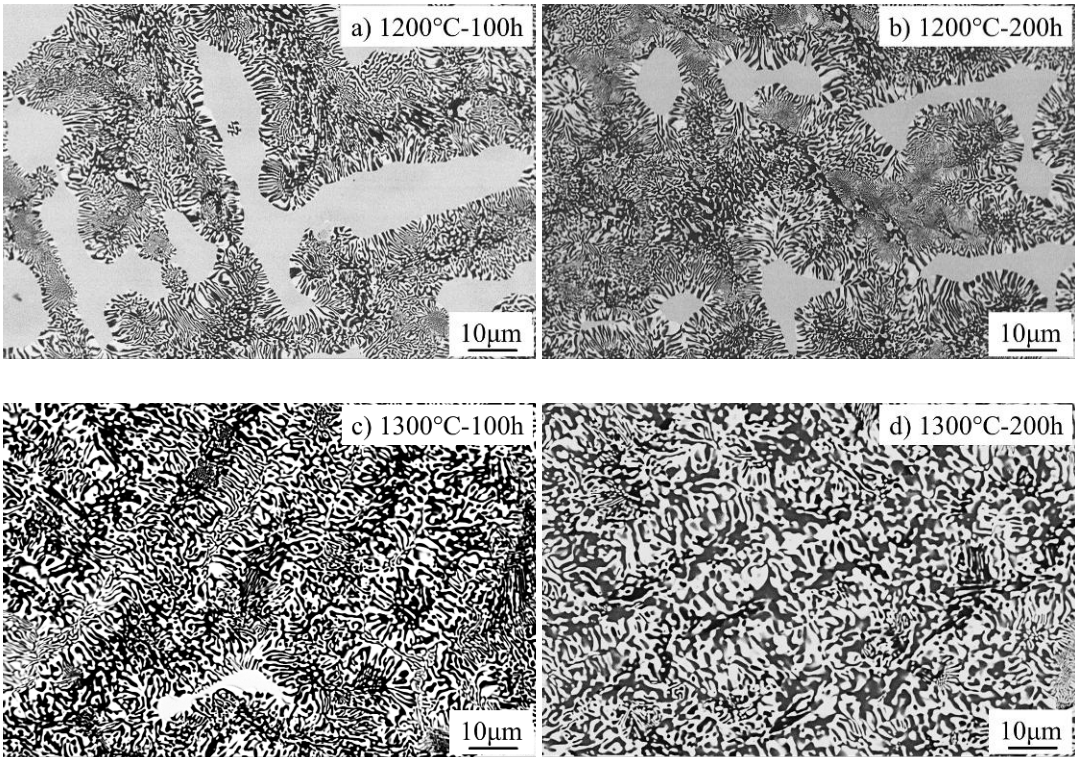

Figure 5.22: SEM images of X5 for heat treatment at 1200-1300 ℃ for 100-200h

In order to quantitatively analyze the content of eutectoid microstructure, it is necessary to calculate the volume fraction of the eutectoid in X5. Based on the SEM images, 44 vol.% eutectoid microstructure is present in the as-cast alloy. Then the volume fraction of the eutectoid microstructure increases stepwise with the increase of temperature and time. Nearly complete eutectoid microstructure with a volume fraction of about 99 vol.% is obtained at 1300 ℃ for 200h (Figure 5.23). Hence, the microstructure of X5 at 1300 ℃ for 200h is considered as the desired eutectoid microstructure.

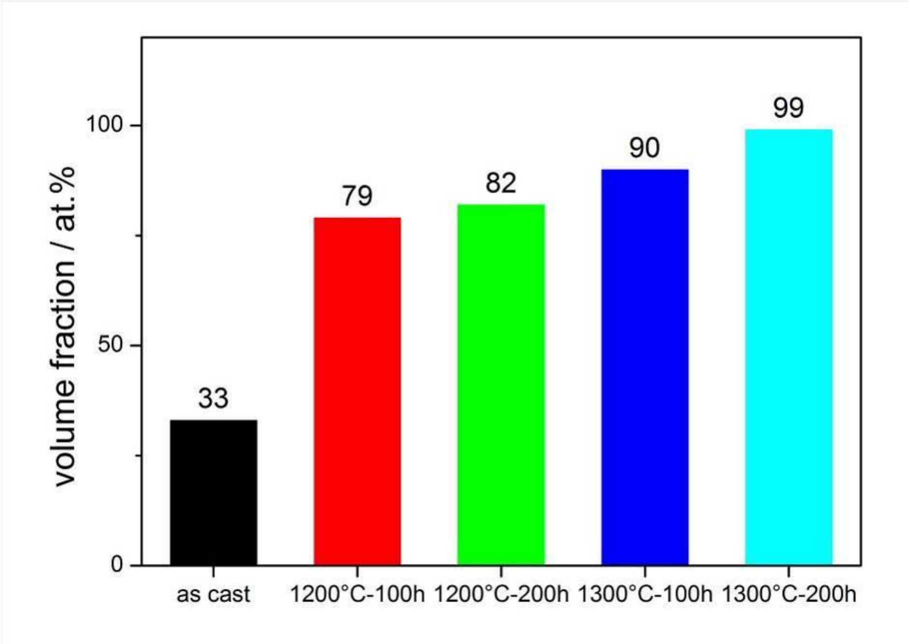

Figure 5.23: Volume fraction of eutectoid microstructures in X5 for the different heat treatment parameters

In addition, as shown in Table 5.5, there are still some differences between the Pandat simulation and experimental observation. Firstly, (Mo, Ti)$_3$Si is stoichiometry with the composition of 25 at.% Si in Pandat. By contrast, the concentration of Si in (Mo, Ti)$_3$Si is observed as 21at.%-24 at.% with EDS. Furthermore, Si concentration is suggested constant for varying Ti to obtain the eutectoid microstructure based on Pandat simulation, while the concentration of Si can be adjusted to eliminate residual phases by the help of EDS.

Table 5.5: Comparison between the Pandat simulation and experimental observation in the eutectoid microstructure

Pandat	**Experimental Observation**
(Mo, Ti)$_3$Si is stoichiometry (25 at.% Si)	21at.%-24 at.% Si in (Mo, Ti)$_3$Si
Si is constant for varying Ti content	Si is to be adjusted, which varies for suppression of residual phases

5.2.3 Conclusions

Based on the liquidus projection suggestion of the Mo-Si-Ti system, a composition of Mo58-Si25-Ti17 (X1) was chosen to obtain the desired eutectoid microstructure of (Mo, Si, Ti) and (Mo, Ti)$_5$Si$_3$. This is because X1 has the highest melting point in the region of (Mo, Ti)$_3$Si and a narrow solidification interval. However, the microstructure of X1 exhibits residual (Mo, Ti)$_5$Si$_3$. The EDS result for the dendritic phase (Mo, Ti)$_3$Si implies to further reduce the Si which eventually leads to alloy X3 with the composition of

Mo53-Si22-Ti25. The microstructure of X3 reveals that almost the whole area is covered with the (Mo, Ti)$_3$Si phase. Therefore, X3 is considered as the expected alloy which has the (Mo, Ti)$_3$Si phase in the entire microstructure. However, there is only a small amount of eutectoid microstructure which is formed at the dendrites boundaries after heat treatment which is believed to be caused by Ti segregation. Increasing Ti content is employed after analyzing the effect of Ti concentration on the eutectoid decomposition. Thus, 34 at.% Ti and 22 at.% Si are considered as a new composition named X4. However, then some residual (Mo, Ti)$_5$Si$_3$ phase formed. By further reducing the Si content, a fine eutectoid microstructure, with the composition of Mo45-Si21-Ti34 (X5), distributes at the dendrite boundaries consisting of (Mo, Ti, Si) + (Mo, Ti)$_5$Si$_3$. Nearly complete eutectoid microstructure with a volume fraction of about 99 vol.% is obtained by the subsequent heat treatment at 1300 ℃ for 200h. Therefore, X5 is believed to be a suitable composition for the formation of fully eutectoid microstructures in Mo-Si-Ti alloys.

5.3 Creep behavior

According to the analysis of the microstructure, E5 and X5 have the desired eutectic and eutectoid microstructure, respectively. Hence, in this part, the effects of different factors including stress and temperature on the creep behavior of E5 and X5 are investigated with the indicators of the creep rate, stress exponent and activation energy. In addition, the microstructure and creep mechanism involved are also analyzed.

5.3.1 Effect of stress on the creep behavior

In Figure 5.24, creep curves of the alloys E5 and X5 are presented in the form of a semi logarithmic plot of strain rate vs. strain. Actually, all curves exhibit a minimum creep rate (green squares) which is probably attributed as the microstructural changes during creep, an analogous to the phenomenon of rafting observed in single-crystalline superalloys [157, 158]. In Figure 5.24 (a), the minimum creep rates of E5 are 1.2×10^{-6} s^{-1} at 50 MPa, 4.7×10^{-6} s^{-1} at 100 MPa, 3.3×10^{-5} s^{-1} at 150 MPa, and 1.9×10^{-4} s^{-1} at 200 MPa, respectively. By contrast, Figure 5.24 (b) shows that the minimum creep rates of X5 increased from 2.3×10^{-8} s^{-1} at 50 MPa to 3.1×10^{-6} s^{-1} at 200 MPa. After comparison, it is found that the minimum creep rates of X5 are substantially lower than that of E5 in the same temperature and stress, meaning that the alloy X5 exhibits a higher creep resistance than E5.

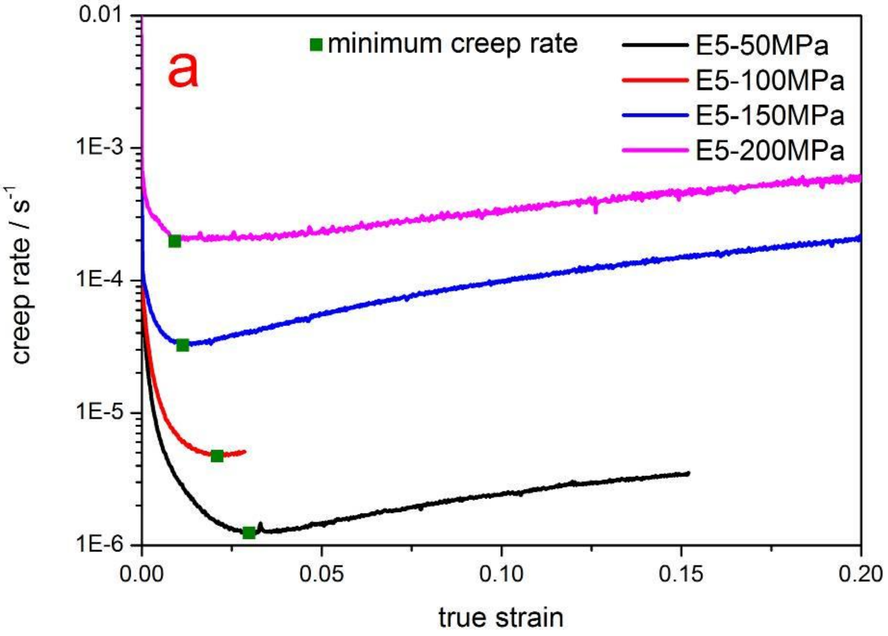

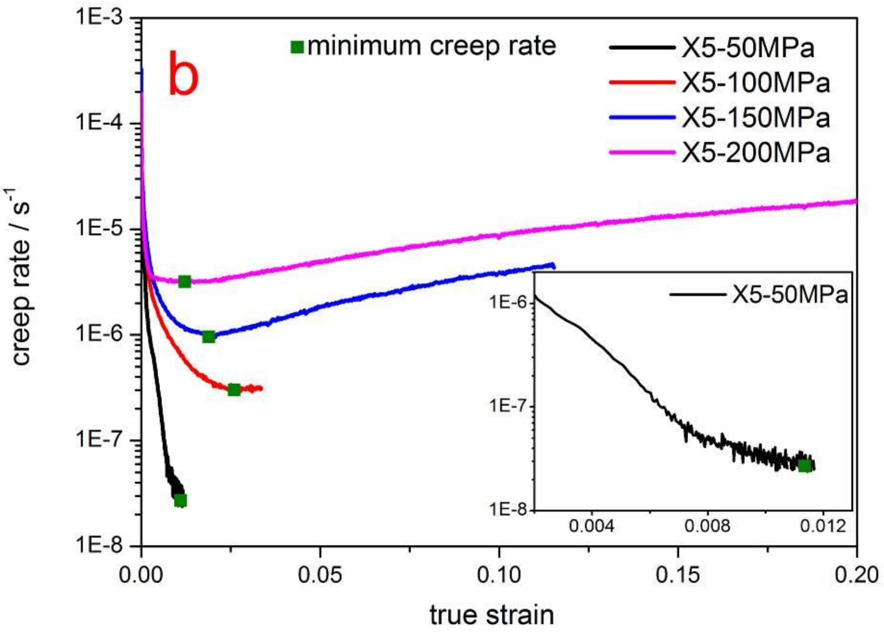

Figure 5.24: Half logarithmic plot of creep rates as a function of true strain at 1200 ℃: (a) E5; (b) X5

Figure 5.25 shows a Norton plot (double logarithmic plot of minimum strain rate vs. stress) of E5 and X5 at 1200 ℃. The values of stress exponent *n* (at the minimum creep rate) in E5 and X5 are 3.6 and 3.5, indicating that E5 and X5 may have the same creep mechanism of dislocation climb according to the stress dependence, where according to literature dislocation climb controls the creep behavior with the value of *n* between 3-5 [159]. In order to check whether the increase of strain rate causes a change in the dominant creep mechanism [160], the strain rates of E5 and X5 are plotted at different plastic strain in the Norton plot, and the corresponding stress exponents are given in Table 5.6. It is found that the creep mechanism of E5 and X5 are not changed, in spite of a slight difference of the stress exponents in the stages from the strain at the minimum creep rate to maximum 0.3 strain.

X5 consists of (Mo, Ti)$_5$Si$_3$ and (Mo, Si, Ti) phases. (Mo, Ti)$_5$Si$_3$ is known as a phase with high creep resistance [107, 161]. The single crystal Mo$_5$Si$_3$ investigated by Mason [161] showed even in soft [314] orientation a creep rate of approximately 10^{-6} s^{-1} at 1300 ℃ and 200 MPa. Meyer et al. [108] also found that the creep rate of Mo$_5$Si$_3$ was 1.5×10^{-7} s^{-1} at 1240 ℃ at a stress of 140 MPa. In addition, the creep rate of 4×10^{-8} s^{-1} at 1200 ℃ was reached at 69 MPa for the single phase Mo$_5$Si$_3$ [108]. Although these experimental temperatures (1200 ℃, 1240 ℃ and 1300 ℃) are higher than or the same as the investigated temperatures for alloy X5 (Figure 5.24), the creep rates of Mo$_5$Si$_3$ described in literature are lower than that of X5. Hence, the (Mo, Ti)$_5$Si$_3$ phase is believed not to significantly participate to the creep of X5. By contrast, the results indicate that the other present phase (Mo, Si, Ti) in X5 dominates the creep process. The creep behavior of X5 is found to be comparable with a three phase alloy (Mo solid solution, Mo$_5$Si$_3$ and Mo$_5$SiB$_2$ with respect to (minimum) creep rate and stress exponent [160], in which the Mo solid solution is also considered as the only phase that contributes to the creep behavior.

Alloy E5 consists of (Ti, Mo)$_5$Si$_3$ and (Mo, Si, Ti) phases. It displays a significantly higher minimum creep rate than alloy X5. This might be due to that the (Ti, Mo)$_5$Si$_3$ phase may also participate in the creep process. Actually, as reported by Sadananda et al. [162], the creep rate of monolithic Ti$_5$Si$_3$ at 1200 ℃ is close to the creep rate of E5 (approximately 8×10^{-5} s^{-1} at 50 MPa and 8×10^{-4} s^{-1} at 100 MPa). In addition, assuming power law creep, the stress exponent of Ti$_5$Si$_3$ is approximately 3, meaning that the creep mechanism is also dislocation climb. This corresponds to the stress exponent of E5. Azim et al. [163] reported that (Ti, Mo)$_5$Si$_3$ possesses some dislocations observed by TEM after 0.15 strain at 1300 ℃ and 200MPa. Overall, it can be concluded that the (Ti, Mo)$_5$Si$_3$ phase and most probably (Mo, Si, Ti), too, contribute the creep process of E5.

Taking this observation and the above-discussed deformability of E5 and X5 into account, (Ti, Mo)$_5$Si$_3$ phase is a deformable phase at the test temperatures in E5. By contrast, (Mo, Si, Ti) phase dominates the creep process in E5 and X5. (Mo, Ti)$_5$Si$_3$ is considered to be not a deformable phase, yielding a much better creep resistance than that of (Ti, Mo)$_5$Si$_3$. Hence, overall alloy X5 has a better creep resistance than E5.

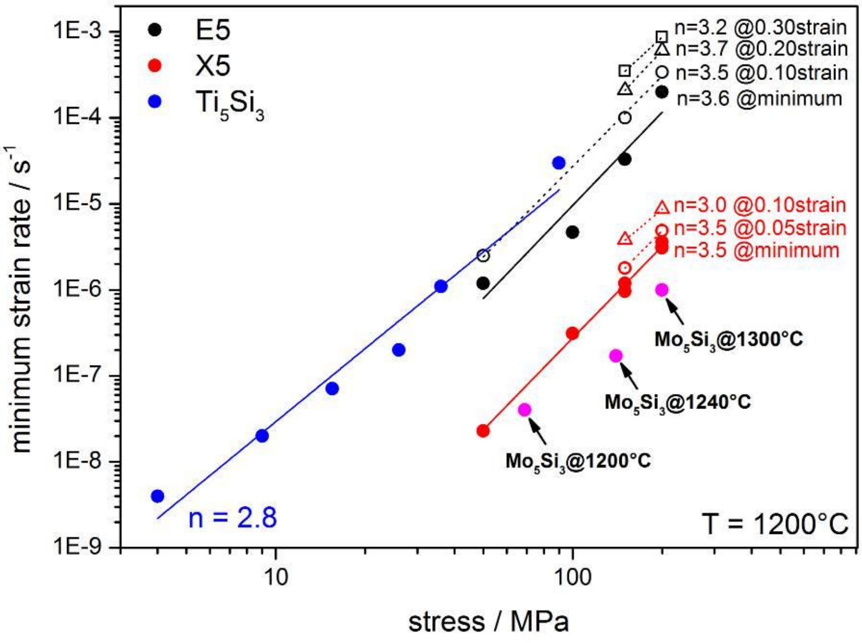

Figure 5.25: Norton plot for minimum creep rates for E5, X5, Ti$_5$Si$_3$ [162] at 1200 ℃ and Mo$_5$Si$_3$ at 1200 ℃-1100 ℃ [108, 161]

Table 5.6: The stress exponents evaluated at different strains and stresses in E5 and X5 at 1200 ℃

Alloy	**Strain in minimum creep rate**	**0.05 strain**	**0.10 strain**	**0.20 strain**	**0.30 strain**
E5	3.6	-	3.5	3.7	3.2
X5	3.5	3.5	3.0	-	-

Ni-based alloys and Mo-based alloys are widely investigated in high temperature environment. In Ni-based alloy, single-crystal CMSX-4 can be considered as a good representative for high creep resistance. By contrast, in Mo-based alloy, Mo9Si8B0.4La$_2$O$_3$ shows an excellent performance in terms of creep resistance, which is even higher than that of CMSX-4. Hence, the minimum creep rates of CMSX-4 and Mo9Si8B0.4La$_2$O$_3$ are compared with the investigated alloy in the present work [49]. As shown in Figure 5.26, CMSX-4 exhibits a higher creep rate than the other alloys at 1200 ℃. This is because γ' is the strengthening phase in CMSX-4 and 1200 ℃ is already close to its solvus temperature. Thus, a substantial decrease in the volume fraction of γ' phase occurs, leading to accelerated creep [164]. In addition, Mo9Si8B0.4La$_2$O$_3$ alloy and Mo21Si34Ti0.5B alloy exhibit almost the same creep behavior. Mo21Si34Ti0.5B has a higher creep rate in comparison to alloy X5, suggesting that adding a small amount of B has no significant influence on the creep rate of the Mo-Si-Ti alloy. Therefore, alloy X5 exhibits the best creep resistance among the alloys under comparison, which is promising for commercial application.

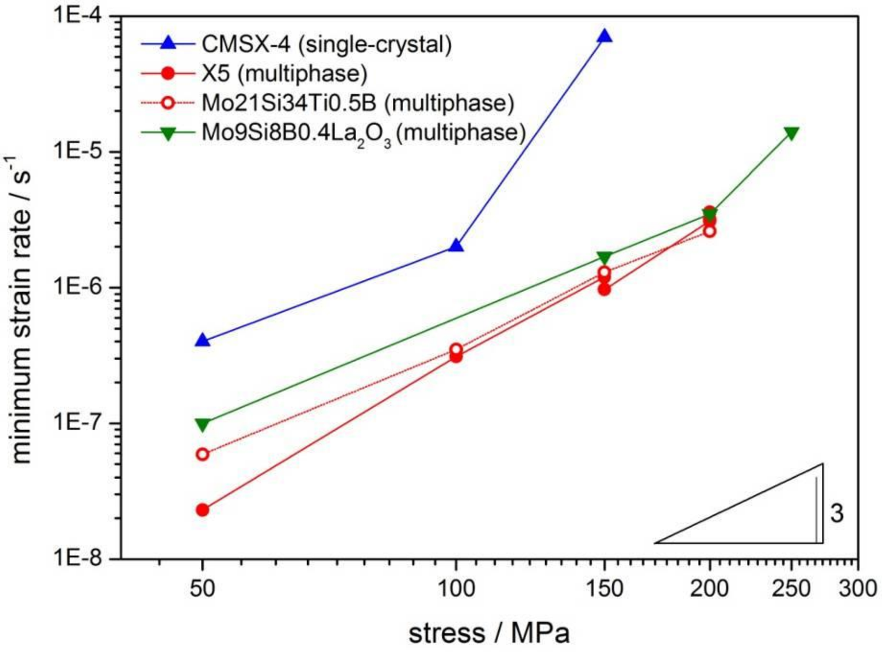

Figure 5.26: Comparison of the creep rates of the various alloys at 1200 ℃ [163] (a ruler which the slope is 3 displays in the lower right corner)

5.3.2 Effect of temperature on the creep behavior

The effect of temperature on the creep behavior of alloys E5 and X5 is investigated in the temperature range of 1000-1300 ℃ at a constant stress of 200 MPa. As shown in Figure 5.27 (a), the minimum creep rates of E5 are 4.6×10^{-7} s^{-1} at 1000 ℃, 1.1×10^{-5} s^{-1} at 1100 ℃, and 2×10^{-4} s^{-1} at 1200 ℃, respectively. In X5, the minimum creep rates vary from 2.2×10^{-7} s^{-1} at 1100 ℃ to 3.7×10^{-5} s^{-1} at 1300 ℃ (Figure 5.27 (b)). Compared with E5, the minimum creep rates of X5 are lower at the same temperature and stress, meaning a higher creep resistance of X5 under the researched temperature and stress conditions is observed.

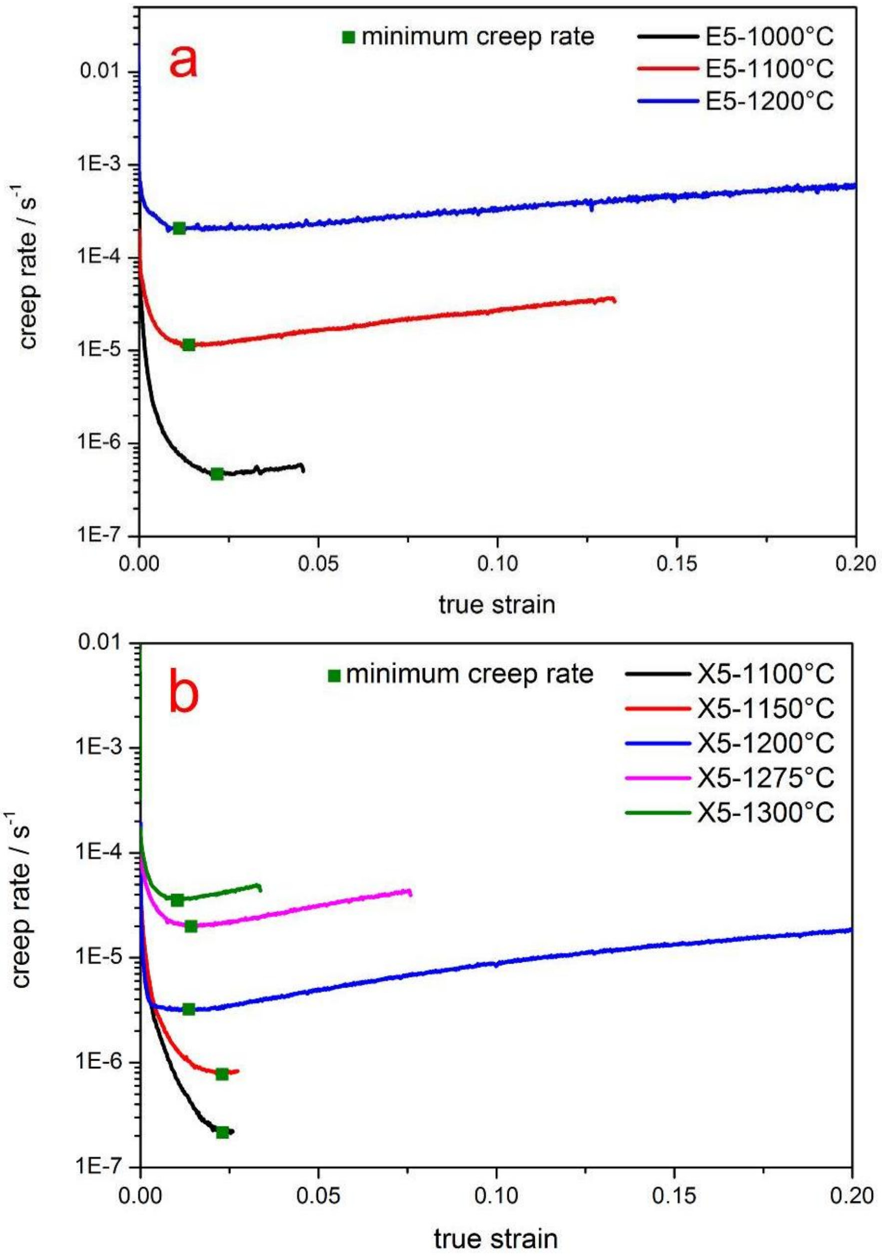

Figure 5.27: Half logarithmic plot of creep rates as a function of true strain at 200 MPa

A further indication of the phases participating in the creep deformation may be the activation energy for creep. This can be extracted from the Arrhenius plot in Figure 5.28 at 200 MPa in X5 and E5. The activation energies for X5 and E5 are about 461 kJ/mol and 472 kJ/mol, respectively. An activation energy of 510 kJ/mol was reported in the single crystal Mo_5Si_3 with the [314] orientation [161], which is substantially higher than that of X5, indicating that there should be no significant contribution for $(Mo, Ti)_5Si_3$ in the plastic deformation of X5. With the presence of Ti and Si, the activation energy of (Mo, Si, Ti) is considered to be equal or higher than 405 kJ/mol (being the activation energy of the self-diffusion of Mo) [165, 166], thus, creep of alloy X5 may be controlled by the deformation of the Mo solid solution. It is also reported that the intermetallic Ti_5Si_3 exhibits an activation energy of 350 ±20 kJ/mol [134], which is lower than the activation energy of E5. Hence, it is likely that deformation of the phases (Mo, Si, Ti) and $(Ti, Mo)_5Si_3$ will dominate the creep process of E5.

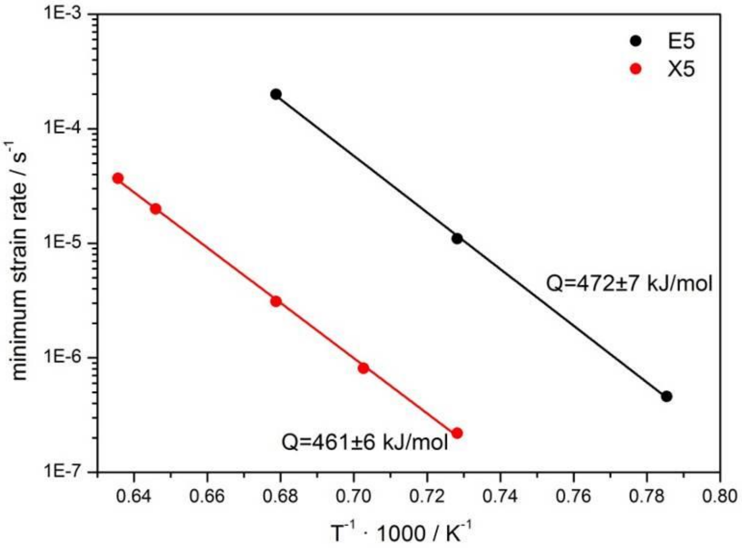

Figure 5.28: Arrhenius plot and corresponding activation energies for E5 and X5 in the stress of 200 MPa

5.3.3 Microstructures of alloys after creep

To verify the stability of X5 and E5 during creep, the microstructures and respective phase distributions are determined after creep and are tabulated in Figure 5.29 and Table 5.7. Comparison of the microstructures before creep and after creep at the minimum creep rate (1200 ℃-100MPa for E5 and 1200 ℃-200MPa for X5), no significant microstructure coarsening is observed, indicating the microstructure stability of both alloys X5 and E5. In addition, the volume fractions of (Mo, Si, Ti) and $(Ti, Mo)_5Si_3$ in E5 of about 48 at.% and 52 at.%, respectively (Table 5.7), do not change during creep testing. Similarly, there is also no significant difference in the volume fraction of the phases in X5 before creep and at the minimum creep rate. Simultaneously, the phase boundary densities (P) can be determined to further analyse the phase distribution. The specific calculation is as follows [160, 167]:

$$P = \frac{2N}{L} \tag{5.4}$$

where N is the amount of the phase boundary in a straight line that is arbitrarily set in SEM images, L is the length of the straight line.

As shown in Table 5.7, after creep at the minimum creep rate (less than 0.02 strain), the phase boundary density slightly varies from 0.93 μm^{-1} to 0.99 μm^{-1} in E5, and from 1.61 μm^{-1} to 1.74 μm^{-1} in X5, respectively. By contrast, when the strain is more than 0.6, the phase boundary density significantly decreases to 0.55 μm^{-1} in E5 and 1.16 μm^{-1} in X5, respectively, implying that the microstructures of both alloys change. The SEM results show that the microstructures of E5 and X5 obviously change after creep with a more than 0.6 strain (Figure 5.29 (c) and (f)), compared to the microstructure before creep and after creep at the minimum creep rate (less than 0.02 strain). Particularly, an obvious coarsening microstructure is found in E5 (Figure 5.29 (c)). The unstable microstructure accelerates the coarsening and creep behavior [168].

It is a common feature of creep testing at constant load or stress that materials with unstable microstructures exhibit a minimum creep rate, whereas materials with stable microstructures show steady-state creep [53-59].

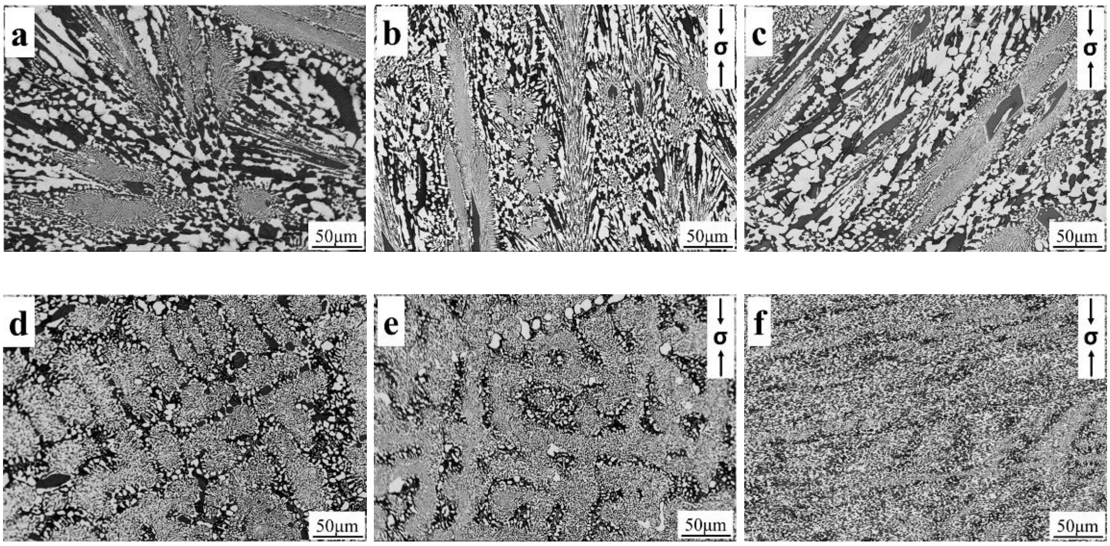

Figure 5.29: SEM images for E5 and X5: (a) microstructure of E5 before creep; (b) microstructure of E5 at the minimum creep rate (less than 0.02 strain) at 1200 ℃ and 100MPa; (c) microstructure of E5 after creep (more than 0.6 strain) at 1200 ℃ and 150MPa; (d) microstructure of X5 before creep; (e) microstructure of X5 at the minimum creep rate (less than 0.02 strain) at 1200 ℃ and 200MPa; (f) microstructure of X5 after creep (more than 0.6 strain) at 1200 ℃ and 150MPa (the direction of the arrow in (b), (c), (e) and (f) represents the direction of the creep stress loading)

Table 5.7: Volume fractions of different phases before creep and at the minimum creep rate and phase boundary densities of the investigated alloys (standard deviation in parentheses)

Alloy		**(Mo, Si, Ti)**	**(Ti, Mo)$_5$Si$_3$**	**(Mo, Ti)$_5$Si$_3$**	**Phase boundary density (μm^{-1})**
E5	before creep	47.9(±3.1)	52.1(±3.3)	-	0.93
	at the minimum creep rate	46.6(±2.1)	53.4(±2.8)	-	0.99
	more than 0.6 strain	-	-	-	0.55
X5	before creep	54.2(±3.0)	-	45.8(±3.5)	1.61
	at the minimum creep rate	55.1(±2.7)	-	44.9(±3.0)	1.74
	morethan 0.6 strain	-	-	-	1.16

5.3.4 Conclusions

The determined stress exponents of 3.6 in E5 and 3.5 in alloy X5 demonstrate that dislocation climb controlled creep is active. In alloy E5, (Ti, Mo)$_5$Si$_3$ and (Mo, Si, Ti) play the main role in the creep process based on the analysis of the strain rate and the activation energy. By contrast, (Mo, Si, Ti) dominates the creep process of X5. It is also found that X5 has a better creep resistance behavior than E5. This is because (Mo, Ti)$_5$Si$_3$ has a lower creep rate than the other phases present and, thus, significantly improves the creep resistance of X5. By contrast, (Ti, Mo)$_5$Si$_3$, is a relatively easy deformable phase in E5, hence, alloy E5 has a lower creep resistance than (Mo, Ti)$_5$Si$_3$ in X5.

Furthermore, E5 and X5 have stable microstructures during creep with the strain that less than 0.02 by the analysis of the volume fractions of different phases and the phase boundary density. However, when the strain is more than 0.6, the phase boundary density significantly decreases, implying the microstructures of both alloys change. The unstable microstructure accelerates the coarsening and creep behavior. Thus, E5 and X5 exhibit a minimum creep rate rather than steady state creep rate.

Comparison with single-crystal Ni-based alloys CMSX-4 and Mo-based alloys such as Mo9Si8B0.4La$_2$O$_3$, X5 exhibits the best creep resistance, which is probably beneficial for its commercial application.

5.4 Oxidation behavior

In this part, the oxidation behavior of E5 and X5 at 800, 1100 and 1200 ℃ in laboratory air is investigated under continuous exposure and cyclic conditions, respectively. In this context, the related oxidation mechanisms are discussed.

5.4.1 Mass change

The mass changes of E5 and X5 during cyclic oxidation at 800 ℃, 1100 ℃ and 1200 ℃ are recorded in Figure 5.30. It is found that nearly no mass change of E5 is observed at 800 ℃, while a slight mass gain is observed at 1100 ℃ and 1200 ℃. The TGA results of E5 are almost consistent with that of the cyclic oxidation at 800 ℃ and 1100 ℃. At 1200 ℃, the mass change reaches a steady state after 20h and 70h in the cyclic oxidation and TGA, respectively. The cyclic and TGA results are consistent in X5, as shown in Figure 5.30 (c-d). Specifically, the mass loss of X5 is serious at 800 ℃, while there is a slight decrease at 1100 ℃. Almost no mass change is observed at 1200 ℃.

Based on the oxidation kinetic rules of mass change over time for various oxidation processes (Figure. 2.2), the parabolic rate law and the linear rate law are selected in this research, and the relevant oxidation rate constants were calculated with the equ. 2.4 $\left(\frac{\Delta m}{A}\right)^2 = k_p \cdot t$ [169] and equ. 2.5 $\left(\frac{\Delta m}{A}\right) = k_l \cdot t$ [170], respectively. The determination coefficient (R^2) was employed to compare the fitness of both equations and the higher values are list in Table 5.8. E5 exhibits a linear mass change during oxidation at 800 ℃, 1100 ℃, and a parabolic mass change at 1200 ℃. Further, no oxidation rate constants were calculated for X5 at 800 ℃, 1100 ℃ and 1200 ℃ because of their negative (at 800 and 1100 ℃)/positive and negative alternating (at 1200 ℃) mass change in the oxidation kinetics (Figure 5.30 (c)-(d)), which cannot be explained by the oxidation kinetic rules equs. 2.4 and 2.5, respectively.

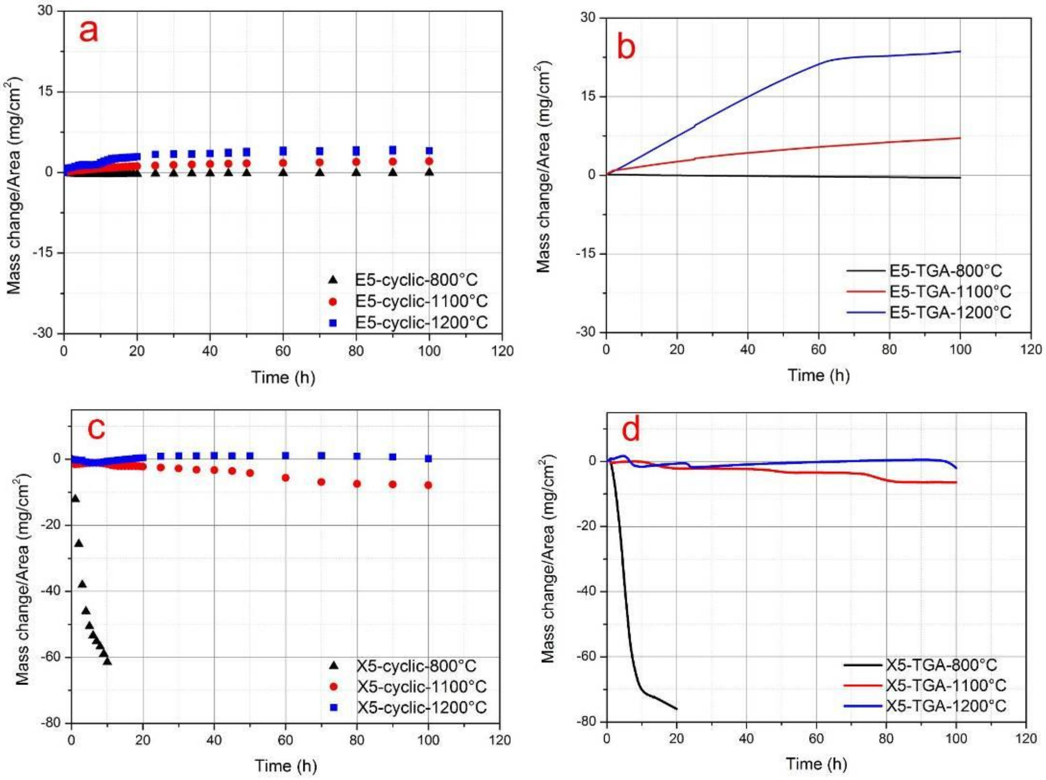

Figure 5.30: Cyclic oxidation kinetics and TGA oxidation of E5 and X5 at 800 ℃-1200 ℃: (a) cyclic oxidation of E5; (b) TGA of E5; (c) cyclic oxidation of X5; (d) TGA of X5

Table 5.8: Oxidation rate constants of k_p or k_l value from cyclic and TGA oxidation tests after 100 h of E5 (*means that the samples exhibit parabolic rate law (k_p: mg^2 cm^{-4} h^{-1}) [169]; others correspond a linear rate law (k_l: mg cm^{-2} h^{-1}) [170])

Oxidation temperature (℃)	E5			
	cyclic	R^2	TGA	R^2
800	2.3×10^{-3}	0.97	5.9×10^{-3}	0.98
1100	1.5×10^{-2}	0.92	6.0×10^{-2}	0.97
1200	$1.8\times10^{-1*}$	0.80	6.9^{*}	0.95

In this research, for E5 at 800 ℃ and 1100 ℃, the oxidation kinetics follows the linear rate law, which suggested that no protective scale is formed. Generally, high-temperature materials of Fe-based, Ni-based, Mo-Si-B alloys rely on the establishment of Cr_2O_3, $A1_2O_3$ or SiO_2 oxidation layers for protection against oxidation, which makes the oxidation kinetics fit the parabolic rate law above 800 ℃ [171]. Thus, Table 5.9 lists the oxidation rate constant of k_p of different alloys (Fe-based, Ni-based and Mo-based alloys) sorted out chromia-, alumina- and silica-former at the temperature range of 1050-1257 ℃.

As shown in Table 5.9, the oxidation rate of Ni34Cr significantly increased at 1200 °C, compared to 1100 °C. This is because the Cr_2O_3 scale becomes unstable with increasing of exposition temperature in Ni34Cr. When temperature exceeds 1100 °C, the external part of the Cr_2O_3 scale is continuously oxidized into gaseous CrO_3, resulting in a decrease of the oxidation resistance. Compared with alloys forming α-Al_2O_3 as the former such as NiCoCrAlYTa/IN792, NiAl0.04Zr, NiCoCrAlYTa/MC2 and Fe25Al, E5 has a slightly higher oxidation rate at 1200 °C. This is probably because that metastable θ-Al_2O_3 phase can transform into the more stable α-Al_2O_3 at 1050 °C [172], which improves the oxidation resistance of the investigated alloys with α-Al_2O_3 as the former.

Table 5.9: Oxidation data of k_p value from the oxidation tests of different alloys at the temperature range of 1050-1257 °C (*a: Balance Ni, 12.4 Cr, 10.0 Co, 2.1 Mo,4.1 W,3.5 Ta,3.1 Al,4.2 Ti, 0.011B, 0.1 Zr,0.2 C (given in wt.%) [173]; *b: Balance Ni, 9.1 Cr, 5.3 Co, 11.2 Al, 1.3 Mo, 1.9 Ti, 2.6 W, 1.9 Ta (given in at.%) [174])

Alloys	**Former**	**Oxidation temperature (°C)**	**Oxidation type**	k_p **($mg^2\ cm^{-4}\ h^{-1}$)**	**References**
Ni34Cr	Cr_2O_3	1100	TGA	3.5×10^{-1}	[175]
Ni34Cr		1200	TGA	0.1×10^{1}	[175]
NiCoCrAlYTa/IN792*^{a}	α-Al_2O_3	1050	TGA	0.87×10^{-2}	[176]
NiAl0.04Zr		1200	TGA	0.85×10^{-2}	[176]
NiCoCrAlYTa/MC2*^{b}		1150	cyclic	0.82×10^{-2}	[174]
Fe25Al		1152	cyclic	3.0×10^{-2}	[177]
Mo9Si8B	SiO_2	1200	TGA	4.3×10^{-1}	[178]
Mo9Si8B1Zr		1200	TGA	10.8×10^{-1}	[178]
E5		1200	TGA	6.9	in this work
E5		1200	cyclic	1.8×10^{-1}	in this work

5.4.2 Oxide scales

Figure 5.31 shows SEM microstructures (surface and cross-section views) of E5 after cyclic oxidation at 800 °C-1200 °C for 100 h. At 800 °C, TiO_2 (rutile) is detected on the surface with the main 2θ of 27.44°, 53.99°{211}, 56.63°{220}(pattern No. PDF 21-1276) (Figure 5.32), which seems to act as a covering scale with an average thickness of less than 1 μm. Normally, the formation of TiO_2 increases the mass of the sample. However, according to the results of cyclic oxidation in Figure 5.30 (a), E5 exhibits almost no mass change at 800 °C. Therefore, it is possible that evaporation of MoO_3 occurred simultaneously during scale formation which could yield a total very low weight change. EDS results also show that no Mo is present on the surface (Table 5.10). In addition, it should be pointed out that SiO_2 (quartz) is detected by XRD with the main 2θ of 40.29°{111}, 42.45°{200} and 73.47°{104} (pattern No. PDF 46-1045) and a small amount of Si (3 at.% in Table 5.10) is found in EDS. Hence, a small amount of SiO_2 is present in E5, which is found among the particle TiO_2.

As shown in Figure 5.31 (c), only a continuous TiO_2 scale (detected by XRD (Figure 5.32)) is observed on the surface of E5 after cyclic oxidation at 1100 ℃. Actually, Ti has a high concentration (52.8 at.%) in E5 (Table 5.1), and the diffusion of O in TiO_2 is faster than that in SiO_2 at 1100 ℃ [179, 180]. Thus, after the MoO_3 evaporates, TiO_2 is easy to form and covers the surface with increasing exposure time, especially above the Ti-rich (Ti, $Mo)_5Si_3$ phase. In addition, there is a content of 1.5 at.% Si on the surface of the sample analyzed by EDS. Observed by the cross section of the sample in Figure 5.31 (d), it is found that the oxide scale consists of a continuous TiO_2 scale, and a duplex scale underneath consisting of SiO_2 and TiO_2 (based on the EDS results (Table 5.10). Importantly, the depth of the outside TiO_2 scale is variable in the different regions (Figure 5.31 (d)). Because in some regions the scale is too thin that can easily be penetrated, SiO_2 located in the inside oxide scale can be detected by XRD.

The outermost TiO_2 scale grows through outward Ti diffusion [164]. The duplex scale is formed through inward diffusion of oxygen [163]. In this research, because of the poor viscosity and mobility, TiO_2 cannot establish an effective protective scale against oxidation at 1100 ℃. A similar conclusion was reported by Azim et al. [181], in which the diffusion of O into the Ti-rich (Ti, $Mo)_5Si_3$ phase was accelerated after oxidation for 5 min at temperatures beyond 1100 ℃. They pointed out that the accelerated growing rate of TiO_2, the high volume fraction of Ti and the different thermal expansion coefficients for TiO_2 and SiO_2 (coefficient of thermal expansion of SiO_2 is about forty times lower than TiO_2 [181]) are the reasons for the development of a highly porous duplex layer mainly consisting of rutile. Compared with the grain size of microstructure on the surface of E5 at 1100 ℃, a more coarse-grained TiO_2 is observed at 1200 ℃. The diffusion increases with increasing of temperature and the duplex layer becomes thicker (Figure 5.31 (f)).

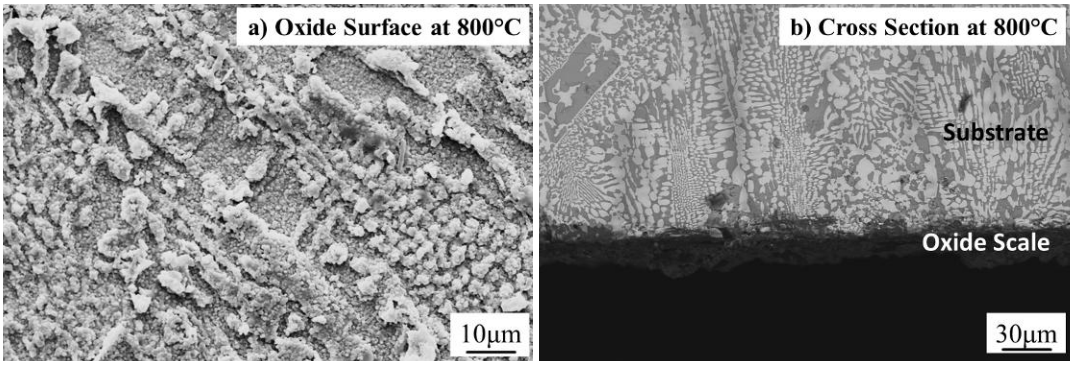

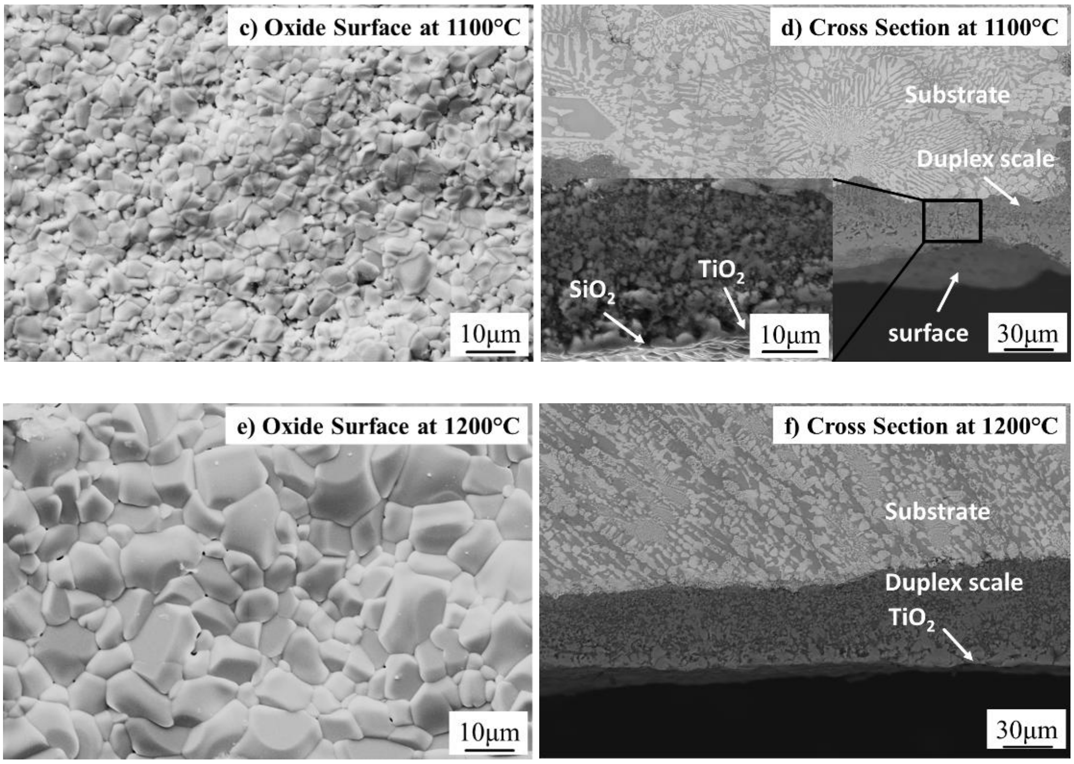

Figure 5.31: Microstructures of the oxide surface and cross section of E5 at 800 ℃-1200 ℃: (a) oxide surface at 800 ℃; (b) cross section at 800 ℃; (c) oxide surface at 1100 ℃; (d) cross section at 1100 ℃; (e) oxide surface at 1200 ℃; (f) cross section at 1200 ℃

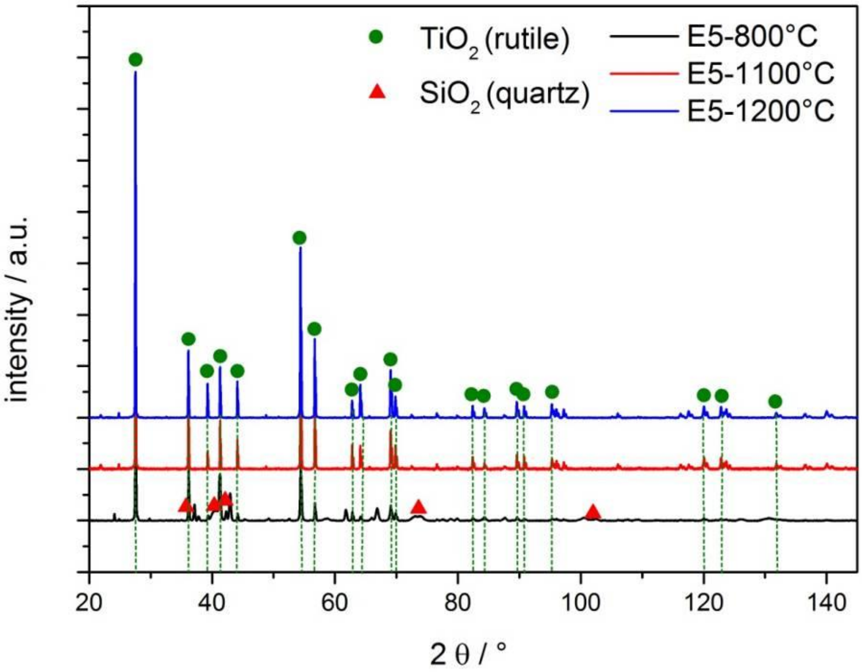

Figure 5.32: XRD patterns of the surface of oxide E5 at 800 ℃-1200 ℃

Table 5.10: EDS results for alloy E5 on the surface and the duplex scale at 800 ℃-1200 ℃

Element (at.%)	**800 ℃**		**1100 ℃**		**1200 ℃**	
	surface	**duplex scale**	**surface**	**duplex scale**	**surface**	**duplex scale**
Mo	0.0	2.1	0.0	0.1	0.0	0.1
Si	3.0	6.8	1.5	14.4	0.5	9.7
Ti	33.9	40.5	44.8	13.6	46.6	16.5
O	63.1	50.6	53.7	71.9	52.9	73.7

The micrograph of the oxidized X5 alloy is shown in Figure 5.33. At 800 ℃, some cracks and pores are present on the surface and on the cross section, suggesting a lack of oxidation protection. At this temperature, Mo reacts with O and then the formed oxide MoO_3 phase volatilizes. Meanwhile, the formation of the SiO_2 phase is too low that cannot offer protection against further oxidation. A similar phenomenon is reported for Mo-23Si-30Ti at 820 ℃ [163], in which the low Si activity could not form a continuous/adherent oxide layer quickly, then the sample was fully degraded and pesting occurred.

At 1100 ℃-1200 ℃, a TiO_2 scale (Figure 5.34), detected by X-ray diffraction analysis (with the main 2θ of 27.44 °{110} and 53.99 °{211} (pattern No. PDF 21-1276)), is present. In addition, there is the presence of Si on the surface of the sample in EDS results (Table 5.11), which may be due to the different depth of the outside TiO_2 scale in the different regions such as E5. On the cross section, both TiO_2 scales and the duplex scale of TiO_2 and SiO_2 are found (Table 5.11). Burk et al. [130] indicated that $(Mo, Ti)_5Si_3$ phase exhibited a good oxidation resistance in the temperature range of 750-1300 ℃ through the formation of a SiO_2-TiO_2 duplex layer with SiO_2 as matrix phase. Obviously, SiO_2 matrix phase is an oxidation barrier, which decreases the continuous formation of the outer TiO_2 scale, inhibits the growth and evaporation of Mo oxide [163, 181], and then improves the oxidation resistance of X5.

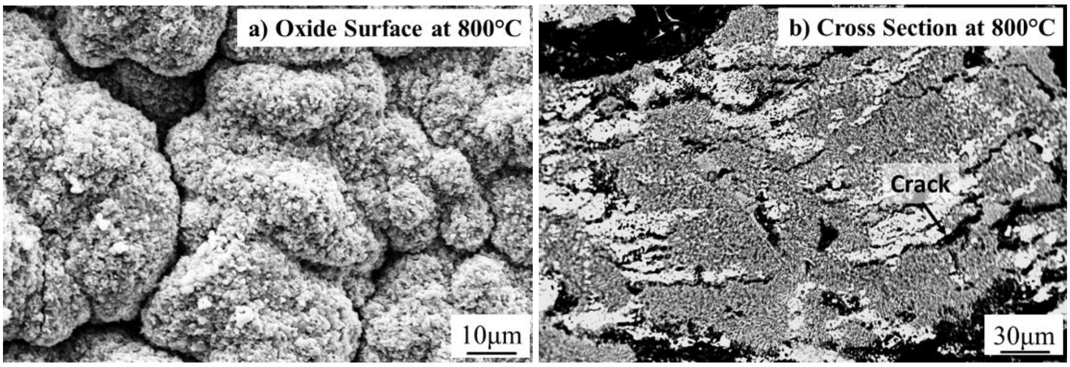

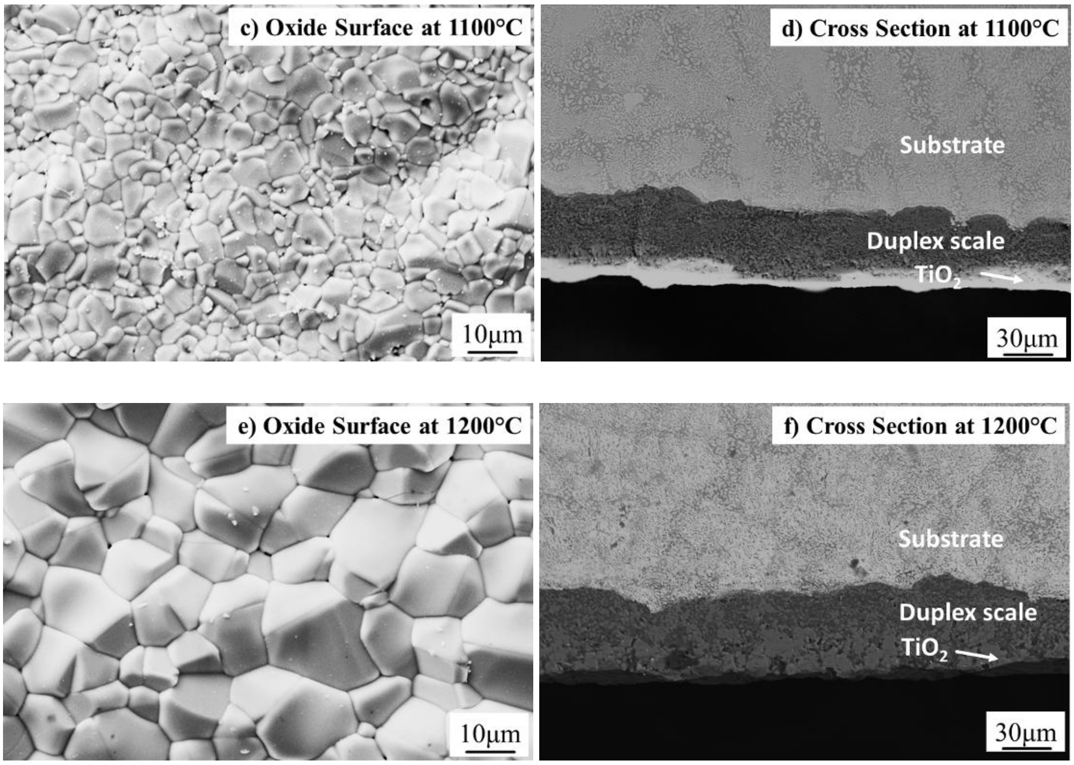

Figure 5.33: Microstructures of the oxide surface and cross section of X5 at 800 ℃-1200 ℃: (a) oxide surface at 800 ℃; (b) cross section at 800 ℃; (c) oxide surface at 1100 ℃; (d) cross section at 1100 ℃; (e) oxide surface at 1200 ℃; (f) cross section at 1200 ℃

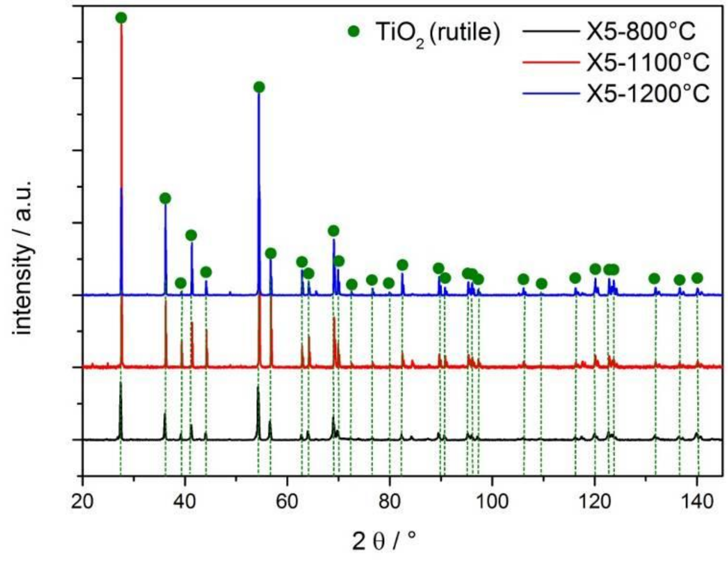

Figure 5.34: XRD patterns of the surface of oxides present in X5 at 800 ℃-1200 ℃

Table 5.11: EDS results for alloy X5 on the surface and the duplex scale at 800 ℃-1200 ℃

Element (at.%)	**800 ℃**	**1100 ℃**		**1200 ℃**	
		surface	**duplex scale**	**surface**	**duplex scale**
Mo	-	0.0	0.0	0.0	0.0
Si	-	1.1	14.1	0.4	18.1
Ti	-	39.2	16.5	33.6	14.0
O	-	59.7	69.4	66.1	67.9

At 820 ℃-1300 ℃, Azim et al. [181] reported that (Mo, Ti)$_5$Si$_3$ is necessary for developing a protective oxide layer for Mo-Si-B-Ti alloy compared with (Ti, Mo)$_5$Si$_3$. The major difference of (Ti, Mo)$_5$Si$_3$ and (Mo, Ti)$_5$Si$_3$ regarding the oxidation behavior is how TiO$_2$ or SiO$_2$ as matrix character, which seems to be pivotal for the oxidation resistance behavior [121]. Burk et al. [130] pointed out a SiO$_2$ matrix with a SiO$_2$-TiO$_2$ duplex scale, which is formed in the oxidation of the bulk monolithic (Mo,Ti)$_5$Si$_3$ phase, acts as an effective oxidation barrier and inhibits the oxidation as well as evaporation of the Ti and Mo oxide. By contrast, if the duplex-layer exhibits a TiO$_2$ matrix, which is the case for the conventional Ti$_5$Si$_3$, its viscosity is insufficient to heal all the pores and gaps between the fast and inhomogeneous growing Ti grains. This results in an unavoidable volatilization of MoO$_3$, and then breakaway oxidation is likely to be observed [129]. However, in the research, according to the analysis of mass change and oxide scale in E5 and X5, it is concluded that E5 consisting of (Ti, Mo)$_5$Si$_3$ and (Mo, Si, Ti) has a better oxidation resistance at 800 ℃ than X5 which consists of (Mo, Ti)$_5$Si$_3$ and (Mo, Si, Ti), indicating that (Ti, Mo)$_5$Si$_3$ exhibits a better oxidation resistance than (Mo, Ti)$_5$Si$_3$ at 800 ℃ because of a similar content of (Mo, Si, Ti) (47.9 at.% in E5 and 54.2 at.% in X5). The possible reason is that TiO$_2$ is easy to form and covers the surface, especially above the Ti-rich (Ti, Mo)$_5$Si$_3$ phase, which improves the oxidation resistance of E5 at 800 ℃.

5.4.3 Pre-oxidation of X5 at 800 ℃

In case of X5, no protective scale is found for 800 ℃, its oxidation resistance is significantly lower than X5 at 1100 ℃-1200 ℃. Mendiratta et al. [182] demonstrated that pre-oxidation of Mo-11Si-11B at 1300 ℃ for 4h improved the oxidation behavior of the sample at 800 ℃. In addition, based on the suggestion of Figure 5.30 (c), there is almost no mass change at 1100 ℃-1200 ℃ for 20h. Hence, it seems to be possible to create a rather protective oxide scale by pre-oxidation at 1100-1200 ℃ which might lead to a better oxidation resistance at 800 ℃.

Figure 5.35 shows a significant improvement in oxidation resistance of pre-oxidized samples as compared to that at 800 ℃ without prior higher-temperature treatment (Figure 5.30 (c)). For all the pre-exposed samples, almost no mass change is found up to 30 h. In particular, the samples pre-oxidized at 1100 ℃ for 10h have a good performance of the oxidation resistance until 60h. Continuous TGA experiment demonstrates that a much lower mass change (0.14 mg/cm^2 at 10h) is observed (Figure 5.36) as compared to that before pre-oxidation at 800 ℃ (70 mg/cm^2 at 10h in Figure 5.30 (d)).

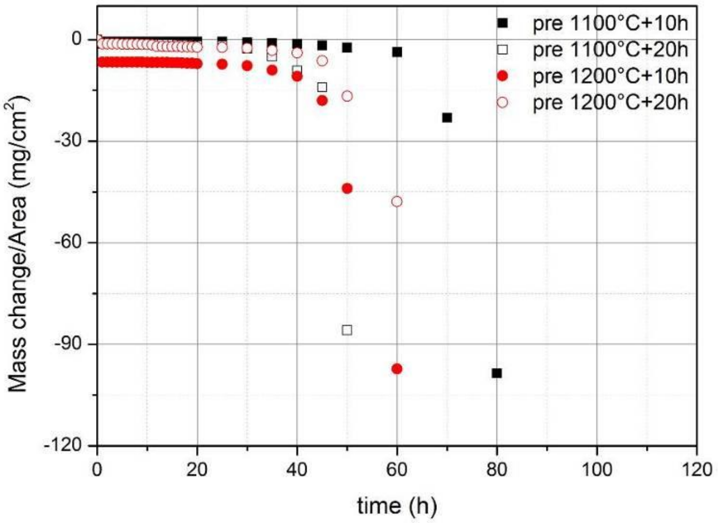

Figure 5.35: Cyclic oxidation kinetics of X5 at 800 ℃ after pre-oxidation at 1100 ℃-1200 ℃

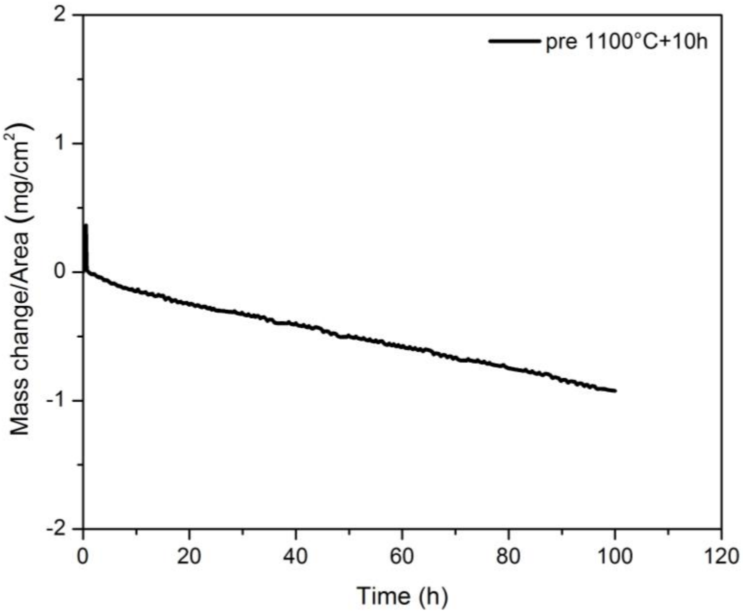

Figure 5.36: TGA oxidation of X5 at 800 ℃ after pre-oxidation at 1100 ℃ for 10h

Figure 5.37 provides the microstructures of the surface and cross section in the X5 pre-oxidized samples before (1100 ℃ for 10h) and after TGA (1100 ℃ for 10h + 800 ℃ for 100h). A continuously oxidized

TiO_2 scale with a thickness of less than 1 μm is present on the surface of the sample before TGA. Underneath this scale, a duplex scale consisting of TiO_2 and SiO_2 develops (Figure 5.37 (a-b)). After TGA, some particles (1-4 μm) are present on the surface of the sample (Figure 5.37 (c)), which is also found in the sample before TGA (Figure 5.37 (a)). The oxide scale on the cross section is divided into an outermost, rutile layer at the oxide/air interface and a duplex scale comprising titania and silica. Compared of the microstructure before TGA, a thicker duplex scale with a thickness of ~ 20 μm is present in the sample after TGA. The thicker duplex scale results in an extension of the inward O diffusion path and therefore inhibits the formation of volatile MoO_3, which improves the oxidation resistance of the sample.

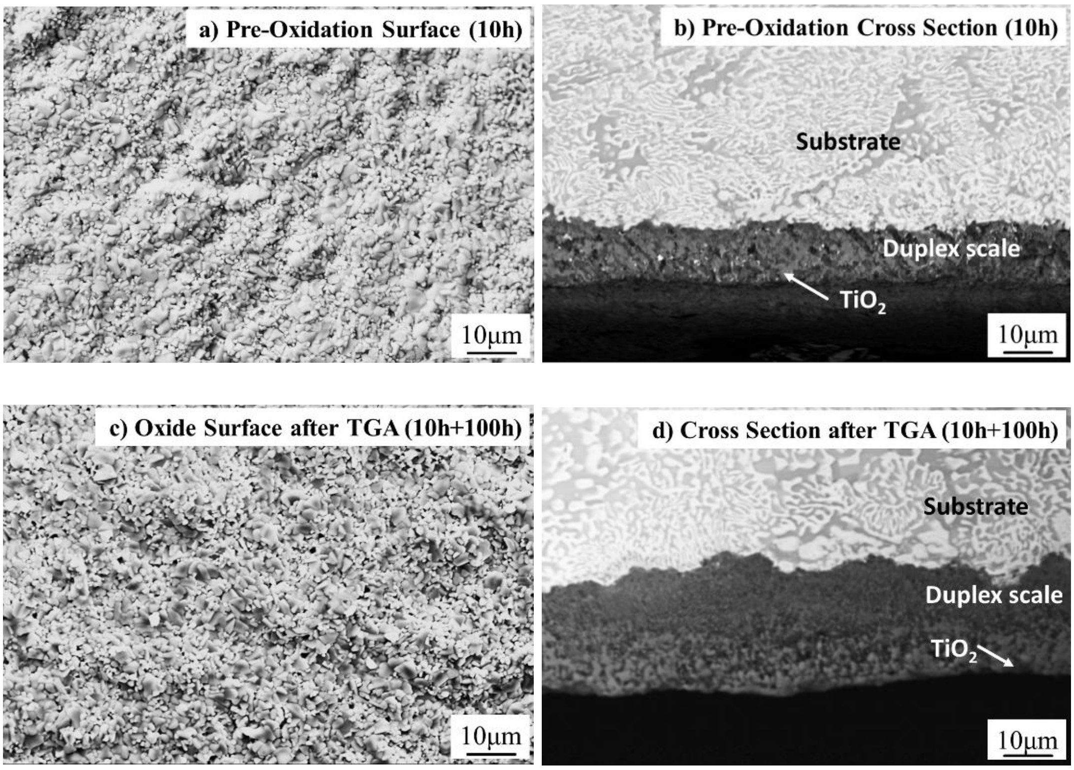

Figure 5.37: Microstructures of the oxide surface and cross section of X5 in pre oxidation at 1100 ℃ for 10h (a-b) and after TGA (1100 ℃ for 10h+800 ℃ for 100h) (c-d)

After the pre-oxidation, a rutile layer and a duplex scale comprising titania and silica are formed in X5. Thus, the oxidation resistance of X5 has significantly improved at 800 ℃ compared of the sample before pre-oxidation.

5.4.4 Conclusions

E5 (consisted of (Mo, Si, Ti) and $(Ti, Mo)_5Si_3$ phases) has a better oxidation resistance at 800 ℃ than X5 (consisted of (Mo, Si, Ti) and $(Mo, Ti)_5Si_3$ phases). Due to a similar content of (Mo, Si, Ti) (47.9 at.% in E5 and 54.2 at.% in X5), it is implied that $(Ti, Mo)_5Si_3$ has a better oxidation resistance than $(Mo, Ti)_5Si_3$ at 800 ℃.

When the oxidation temperatures increase to 1100 ℃ and 1200 ℃, due to the formation of both TiO_2 scale and the duplex scale of TiO_2 and SiO_2, X5 exhibits better oxidation resistance than at 800 ℃, which inhibits the growth and evaporation of Mo oxide. Because of the poor oxidation resistance at 800 ℃ for X5, a pre-oxidation oxidation at 1100 ℃ for 10h is selected to improve the oxidation behavior of X5. After the pre-oxidation, a TiO_2 layer and a duplex scale comprising TiO_2 and SiO_2 are formed in X5. The oxidation behavior of X5 at 800 ℃ is significantly improved with the pre-oxidation oxidation after TGA.

6 Summary and Outlook

In this chapter a brief summary of this work consisting of the microstructures, creep and oxidation behavior of the eutectic and eutectoid is presented first. Second, an outlook is also given which addresses the chances and challenges of directional solidification of these eutectic and eutectoid microstructures.

6.1 Summary

The objective of this work was to evaluate the potential of Mo-Si-Ti alloys as promising high temperature materials. The determination of suitable eutectic and eutectoid compositions for Mo-Si-Ti alloys has been conducted first. Then creep behavior of selected eutectic and eutectoid Mo-Si-Ti alloys were investigated in the temperature range of 1000-1300 ℃ and the stress range of 50-200MPa. The oxidation behavior of these alloys was also investigated at 800, 1100 and 1200 ℃ under constant and cyclic oxidation conditions.

A suitable eutectic microstructure consisted of (Mo, Ti, Si) + (Ti, Mo)$_5$Si$_3$ phases obtained with the composition of Mo27.2-Si20.0-Ti52.8 (E5), which has nearly complete eutectic microstructure (96.1 vol.%). By contrast, a suitable composition for the eutectoid microstructure (Mo, Ti, Si) + (Mo, Ti)$_5$Si$_3$ has been determined as Mo45-Si21-Ti34 (X5) after a suitable heat-treatment condition of 1300 ℃ and 200h. The volume fraction of eutectoid microstructure in X5 is around 99 vol.%.

For the creep behavior, the determined stress exponents are 3.6 in E5 and 3.5 in X5, meaning that dislocation climb is the operative deformation mechanism in E5 and X5. (Ti, Mo)$_5$Si$_3$ and (Mo, Si, Ti) contribute to the creep process in E5 based on the analysis of the strain rate and the activation energy. By contrast, (Mo, Si, Ti) dominates the creep process in X5. X5 has a better creep resistance behavior than that of E5. This is because (Mo, Ti)$_5$Si$_3$ in X5 is not a deformable phase, which thus significantly improves the creep resistance of X5. Furthermore, it is found that E5 and X5 have stable microstructures after creep at the minimum creep rate (less than 0.02 strain) by the analysis of the volume fractions of different phases and the phase boundary density. With the increase of the strain (such as more than 0.6), the phase boundary density significantly decreases, implying the microstructures change of E5 and X5.

Concerning oxidation behavior, at 800 ℃, it is concluded that E5 shows a better oxidation resistance than X5, measured for up to 100h, indicating probably that (Ti, Mo)$_5$Si$_3$ phase in E5 exhibits a better oxidation resistance than (Mo, Ti)$_5$Si$_3$ phase in X5. No protective oxidized scale is found on the surface of X5 oxidized at 800 ℃, and some cracks are present on the surface and the cross section. However, the oxidation behavior of X5 at 800 ℃ is significantly improved when the samples are pre-exposed at 1100 ℃ for 10h and then cyclically oxidized at 800 ℃. SEM results demonstrated that the surface morphology of the alloy is almost the same as the alloy before and after TGA, a thicker duplex scale on the cross section after TGA is observed, which improves the oxidation resistance of the sample by extending the inward O diffusion path to inhibit the formation of volatile MoO_3.

6.2 Outlook

So far, this work provided fundamental knowledge about Mo-Si-Ti alloys with respect to their potential in creep and oxidation resistance. However, in the eutectic and eutectoid microstructure, the transverse grain boundaries, which are perpendicular to the direction of the principal stress are often the main locations of the crack generation and propagation in the creep process. In order to assess whether the properties of E5 and X5 could even further be improved directional solidification technology can be applied to increase the creep resistance of alloys by eliminating the transverse grain boundaries, and producing longitudinally elongated lamellar microstructures [183-186]. Thus, with E5, directional solidification technology was exemplified to obtain a lamellar microstructure by different solidification velocities of 6 mm/h, 18 mm/h, 42 mm/h and 60 mm/h, see Figure 6.1. However, it is found that different morphologies are present in the different areas with different solidification velocities. No or only a small amount of lamellar microstructure is formed. Based on the the Scheil simulation by Pandat, an extended solidification interval (~ 600K) is present in alloy E5 (Figure 5.7), which may be the reason for the formation of different morphologies during the directional solidification.

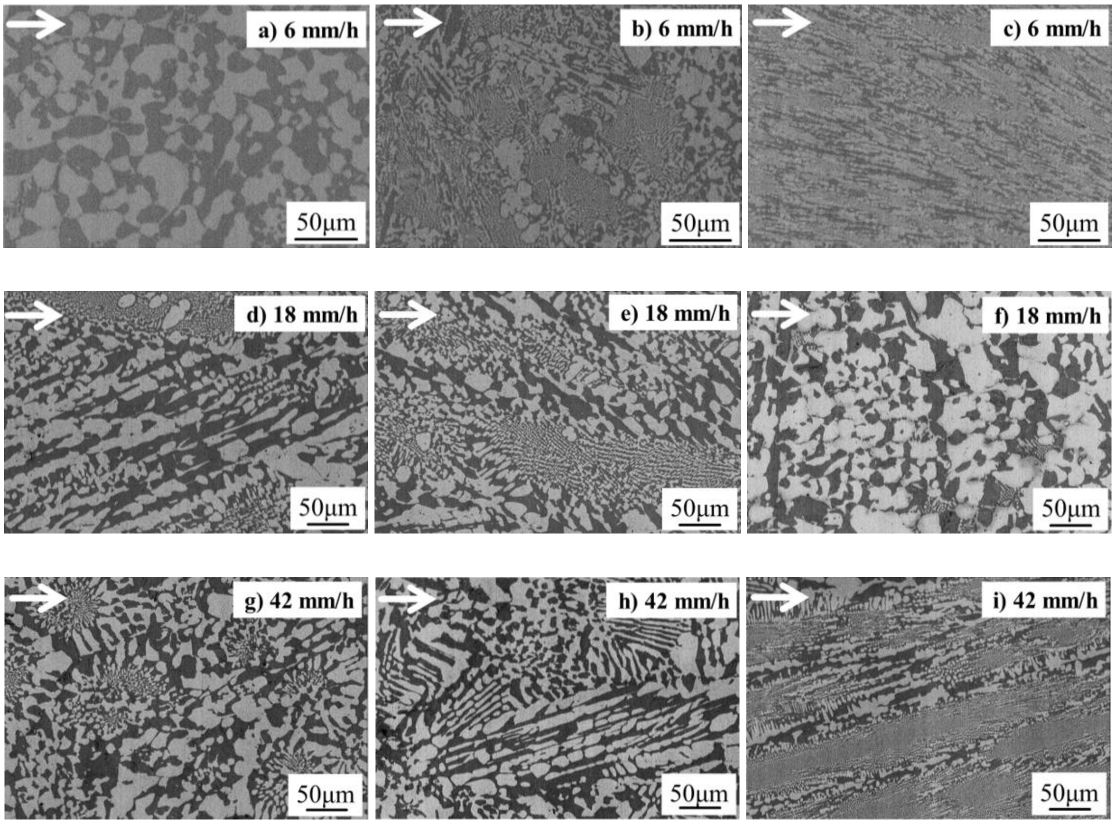

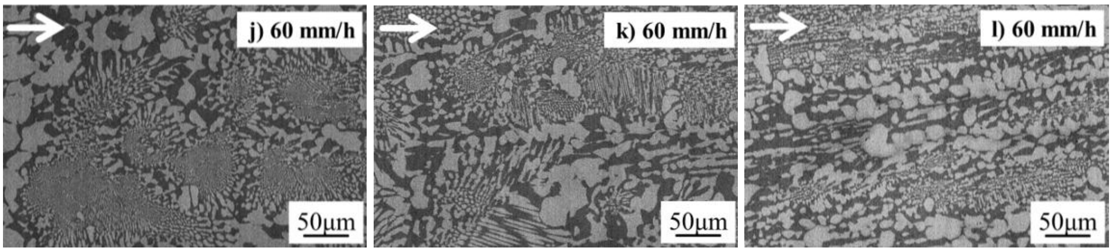

Figure 6.1: Microstructures of E5 after directional solidification at 6 mm/h, 18mm/h, 42 mm/h and 60 mm/h in the different areas of the samples (the arrow direction is the direction of the solidification (a-c at 6 mm/h; d-f at 18 mm/h; g-i at 42 mm/h; j-l at 60 mm)

According to the suggestions of Pandat, alloy X5 with the eutectoid microstructure has a much narrower solidification interval as E5 (~100K). Thus, it may be possible for X5 to obtain a lamellar microstructure after directional solidification. However, the major problem observed was that during the solidification process the samples tend to crack easily (Figure 6.2). This was found to be because of the presence of the brittle Mo_3Si [97, 187].

Figure 6.2: Rod of X5 after arc melting

An alternative approach suggested by some researchers to circumvent the problems with the brittleness of Mo_3Si is to employ powder metallurgy [123, 187-189]. Specifically, elemental powders were milled with hardened steel balls at 1200 rpm under argon atmosphere, and then were compacted by cold isostatic pressing followed by subsequent sintering. A rod without cracks has been successfully obtained in this research. However, oxygen analysis indicated with 1.18 at.% major oxygen pick-up in the sample while only 0.08 at.% O is observed in the arc melted sample (Table 6.1). This may be because Ti is very reactive with oxygen especially when processed as powder due to the increased surface area. The presence of gaseous impurities can also influence the composition of X5, which results in the formation of a residual (Mo, Si, Ti) after the directional solidification (Figure 6.3). Thus, the impact of gas impurities is still a serious problem in the preparation process, which should be systematically evaluated and improved in the later work.

Table 6.1: Oxygen analysis of the materials produced via the bulk and powder route after arc melting

Oxygen analysis (at.%)	**Mo**	**Si**	**Ti**	**O**	**N**
bulk arc melting	43.78	20.56	35.58	**0.08**	43.78
powder arc melting	43.70	20.28	34.78	**1.18**	43.70

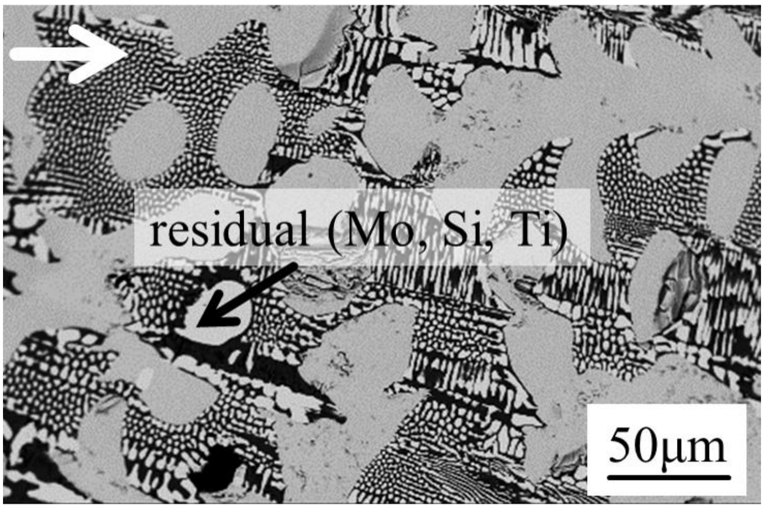

Figure 6.3: Microstructure of X5 after directional solidification at 42 mm/h (the white arrow direction is the direction of the solidification)

7 References

1. Saravanamuttoo, H.I.H., Rogers, G.F.C., and Cohen, H., *Gas turbine theory*. 2001: Pearson Education.
2. Unger, D.P. and Herzog, H.J., *Comparative Study on Energy R&D Performance: Gas Turbine Case Study*. Energy Laboratory, Massachusetts Institute of Technology, Report, 1998.
3. Eliaz, N., Shemesh, G., and Latanision, R., *Hot corrosion in gas turbine components.* Engineering failure analysis, 2002. **9**(1): p. 31-43.
4. Boyce, M.P., *Gas turbine engineering handbook*. 2011: Elsevier.
5. Segersäll, M., *Nickel-Based Single-Crystal Superalloys: the crystal orientation influence on high temperature properties*. Linköping University, Dissertation, 2013.
6. *http://cset.mnsu.edu/engagethermo/images/gasturbineanimation.png*.
7. Sims, C.T., *A history of superalloy metallurgy for superalloy metallurgists.* Superalloys 1984, 1984: p. 399-419.
8. Donachie, M.J. and Donachie, S.J., *Superalloys: a technical guide*. 2002: ASM international.
9. Kobayashi, K., Yamaguchi, K., Hayakawa, M., et al., *High-temperature fatigue properties of austenitic superalloys 718, A286 and 304L.* International Journal of Fatigue, 2008. **30**(10): p. 1978-1984.
10. Krenn, C.R., *The crystallography of fatigue crack initiation in Incoloy-908 and A-286 steel.* Lawrence Berkeley National Laboratory, 2010.
11. Brooks, J.A. and Thompson, A.W., *Microstructure and hydrogen effects on fracture in the alloy A-286.* Metallurgical Transactions A, 1993. **24**(9): p. 1983-1991.
12. De Cicco, H., Luppo, M., Gribaudo, L., et al., *Microstructural development and creep behavior in A286 superalloy.* Materials characterization, 2004. **52**(2): p. 85-92.
13. Ford, D. and Arthey, R., *Development of single crystal alloys for specific engine applications.* Rolls-Royce Limited Metallurgical Research Laboratories, 1986.
14. Ro, Y., Koizumi, Y., and Harada, H., *High temperature tensile properties of a series of nickel-base superalloys on a* γ/γ' *tie line.* Materials Science and Engineering: A, 1997. **223**(1): p. 59-63.
15. Kakehi, K., *Tension/compression asymmetry in creep behavior of a Ni-based superalloy.* Scripta Materialia, 1999. **41**(5): p. 461-465.
16. Reed, R., Matan, N., Cox, D., et al., *Creep of CMSX-4 superalloy single crystals: effects of rafting at high temperature.* Acta materialia, 1999. **47**(12): p. 3367-3381.
17. Kakehi, K., *Effect of primary and secondary precipitates on creep strength of Ni-base superalloy single crystals.* Materials Science and Engineering: A, 2000. **278**(1): p. 135-141.

18. Furrer, D. and Fecht, H., *Ni-based superalloys for turbine discs.* JOM, 1999. **51**(1): p. 14-17.

19. Caron, P. and Lavigne, O., *Recent studies at Onera on superalloys for single crystal turbine blades.* Archive ouverte HAL AerospaceLab,, 2011(3): p. p. 1-14.

20. Ross, E.W. and O'Hara, K.S., *Rene N4: a first generation single crystal turbine airfoil alloy with improved oxidation resistance, low angle boundary strength and superior long time rupture strength.* Superalloys 1996, 1996: p. 19-25.

21. Caron, P. and Khan, T., *Evolution of Ni-based superalloys for single crystal gas turbine blade applications.* Aerospace Science and Technology, 1999. **3**(8): p. 513-523.

22. Frasier, D., Whetstone, J., Harris, K., et al., *Process and alloy optimization for CMSX-4 superalloy single crystal airfoils.* High temperature materials for power engineering, 1990: p. 1281-1300.

23. Harris, K., Erickson, G., Sikkenga, S., et al., *Development of the rhenium containing superalloys CMSX-4® & CM 186 LC® for single crystal blade and directionally solidified vane applications in advanced turbine engines.* Superalloys 1992, 1992. **297**.

24. Harris, K. and Wahl, J.B., *Improved single crystal superalloys, CMSX-4 (SLS)[La+Y] and CMSX-486.* Superalloys 2004, 2004: p. 45-52.

25. Giamei, A. and Anton, D., *Rhenium additions to a Ni-base superalloy: effects on microstructure.* Metallurgical transactions A, 1985. **16**(11): p. 1997-2005.

26. Mottura, A., Finnis, M., and Reed, R., *On the possibility of rhenium clustering in nickel-based superalloys.* Acta Materialia, 2012. **60**(6): p. 2866-2872.

27. O'hara, K.S., Walston, W.S., Ross, E.W., et al., *Nickel base superalloy and article*. U.S. Patent Nr. 5,482,789, 9 Jan. 1996.

28. Walston, S., Cetel, A., MacKay, R., et al., *Joint development of a fourth generation single crystal superalloy.* Patent Nr. NASA/TM-2004-213062, E-14524 , 2004.

29. Sato, A., Harada, H., Yeh, A.-C., et al., *A 5th generation SC superalloy with balanced high temperature properties and processability.* Superalloys, 2008: p. 131-138.

30. Kitaguchi, H., *Microstructure-property relationship in advanced Ni-based superalloys*. Metallurgy-Advances in Materials and Processes. 2012: InTechOpen.

31. Roebuck, B., Cox, D., and Reed, R., *The temperature dependence of γ' volume fraction in a Ni-based single crystal superalloy from resistivity measurements.* Scripta materialia, 2001. **44**(6): p. 917-921.

32. Latief, F.H., Kakehi, K., and Murakami, H., *Anisotropic creep behavior of aluminized Ni-based single crystal superalloy TMS-75.* Materials Science and Engineering: A, 2013. **567**: p. 65-71.

33. Liu, L.-R., Jin, T., Zhao, N.-R., et al., *Effect of carbon addition on the creep properties in a Ni-based single crystal superalloy.* Materials Science and Engineering: A, 2004. **385**(1): p. 105-112.

34. Koizumi, Y., Kobayashi, T., Yokokawa, T., et al., *Development of next-generation Ni-base single crystal superalloys.* Superalloys 2004, 2004: p. 35-43.

35. Dimiduk, D.M. and Perepezko, J.H., *Mo-Si-B alloys: Developing a revolutionary turbine-engine material.* MRS bulletin, 2003. **28**(09): p. 639-645.

36. Caron, P., *High γ' solvus new generation nickel-based superalloys for single crystal turbine blade applications.* Superalloys 2000, 2000: p. 737-746.

37. Sivakumar, R. and Mordike, B., *High temperature coatings for gas turbine blades: a review.* Surface and coatings technology, 1989. **37**(2): p. 139-160.

38. Bewlay, B., Jackson, M., Subramanian, P., et al., *A review of very-high-temperature Nb-silicide-based composites.* Metallurgical and Materials Transactions A, 2003. **34**(10): p. 2043-2052.

39. Bewlay, B., Jackson, M., and Lipsitt, H., *The balance of mechanical and environmental properties of a multielement niobium-niobium silicide-based in situ composite.* Metallurgical and Materials Transactions A, 1996. **27**(12): p. 3801-3808.

40. Mendiratta, M.G. and Dimiduk, D.M., *Strength and toughness of a* Nb/Nb_5Si_3 *composite.* Metallurgical and Materials Transactions A, 1993. **24**(2): p. 501-504.

41. Subramanian, P., Mendiratta, M., and Dimiduk, D., *The development of Nb-based advanced intermetallic alloys for structural applications.* JOM Journal of the Minerals, Metals and Materials Society, 1996. **48**(1): p. 33-38.

42. Murakami, T., Sasaki, S., and Ito, K., *Oxidation behavior and thermal stability of Cr-doped* $Nb(Si, Al)_2$ *and* $Nb_3Si_5Al_2$ *matrix compacts prepared by spark plasma sintering.* Intermetallics, 2003. **11**(3): p. 269-278.

43. Holmes, J., *Tensile creep behaviour of a fibre-reinforced* $SiC\text{-}Si_3N_4$ *composite.* Journal of materials science, 1991. **26**(7): p. 1808-1814.

44. Prewo, K.M. and Brennan, J.J., *High-strength silicon carbide fibre-reinforced glass-matrix composites.* Journal of Materials Science, 1980. **15**(2): p. 463-468.

45. Zhu, S., Mizuno, M., Kagawa, Y., et al., *Monotonic tension, fatigue and creep behavior of SiC-fiber-reinforced SiC-matrix composites: a review.* Composites Science and Technology, 1999. **59**(6): p. 833-851.

46. Jéhanno, P., Heilmaier, M., and Kestler, H., *Characterization of an industrially processed Mo-based silicide alloy.* Intermetallics, 2004. **12**(7): p. 1005-1009.

47. Perepezko, J. and Sakidja, R., *Oxidation-resistant coatings for ultra-high-temperature refractory Mo-based alloys.* JOM, 2010. **62**(10): p. 13-19.

48. Yao, Z., Stiglich, J., and Sudarshan, T., *Molybdenum silicide based materials and their properties.* Journal of Materials Engineering and Performance, 1999. **8**(3): p. 291-304.

49. Heilmaier, M., Krüger, M., Saage, H., et al., *Metallic materials for structural applications beyond nickel-based superalloys.* JOM Journal of the Minerals, Metals and Materials Society, 2009. **61**(7): p. 61-67.

50. Yamaguchi, M., Inui, H., and Ito, K., *High-temperature structural intermetallics.* Acta materialia, 2000. **48**(1): p. 307-322.

51. Kruzic, J., Schneibel, J., and Ritchie, R., *Fracture and fatigue resistance of Mo-Si-B alloys for ultrahigh-temperature structural applications.* Scripta Materialia, 2004. **50**(4): p. 459-464.

52. Gottstein, Günter. *Physikalische grundlagen der materialkunde*. 2007: Springer-Verlag.

53. Takeuchi, S. and Argon, A., *Steady-state creep of single-phase crystalline matter at high temperature.* Journal of materials science, 1976. **11**(8): p. 1542-1566.

54. Wilshire, B. and Scharning, P., *Creep and creep fracture of commercial aluminium alloys.* Journal of Materials Science, 2008. **43**(12): p. 3992-4000.

55. Coakley, J., Dye, D., and Basoalto, H., *Creep and creep modelling of a multimodal nickel-base superalloy.* Acta Materialia, 2011. **59**(3): p. 854-863.

56. Kowalewski, Z., Hayhurst, D., and Dyson, B., *Mechanisms-based creep constitutive equations for an aluminium alloy.* The Journal of Strain Analysis for Engineering Design, 1994. **29**(4): p. 309-316.

57. Evans, R., Parker, J., and Wilshire, B., *The θ projection concept-A model-based approach to design and life extension of engineering plant.* International Journal of Pressure vessels and piping, 1992. **50**(1-3): p. 147-160.

58. Li, Y., *A new creep lifetime prediction method: the C-project concept.* International journal of pressure vessels and piping, 1996. **69**(2): p. 161-167.

59. Campbell, F.C., *Elements of metallurgy and engineering alloys*. 2008: ASM International.

60. Whittaker, M., Harrison, W., Deen, C., et al., *Creep Deformation by Dislocation Movement in Waspaloy.* Materials, 2017. **10**(1): p. 61.

61. Lai, G.Y., *High-temperature corrosion and materials applications*. 2007: ASM International.

62. Janda, D., *Mechanical properties and oxidation behavior of micro-alloyed iron aluminides*. Karlsruher Institut für Technologie, Dissertation, 2015.

63. Fitzer, E. and Benesovsky, F. *Molybdenum disilicide as high-temperature material*. in *Plansee Proc., 2nd Seminar, Reutte/Tyrol*. 1955 1956: p. 56-79.

64. Westbrook, J. and Wood, D., *"PEST" degradation in beryllides, silicides, aluminides, and related compounds.* Journal of Nuclear Materials, 1964. **12**(2): p. 208-215.

65. Grabke, H. and Meier, G., *Accelerated oxidation, internal oxidation, intergranular oxidation, and pesting of intermetallic compounds.* Oxidation of Metals, 1995. **44**(1): p. 147-176.

66. Baek, J.H. and Jeong, Y.H., *Breakaway phenomenon of Zr-based alloys during a high-temperature oxidation.* Journal of Nuclear Materials, 2008. **372**(2): p. 152-159.

67. Evans, H., Donaldson, A., and Gilmour, T., *Mechanisms of breakaway oxidation and application to a chromia-forming steel.* Oxidation of Metals, 1999. **52**(5): p. 379-402.

68. Wadsworth, J. and Wittenauer, J., *The history of development of molybdenum alloys for structural applications*. Conference: 122. annual meeting of the Minerals, Metals and Materials Society (TMS), Denver, CO (United States), 1993.

69. Saage, H., Krüger, M., Sturm, D., et al., *Ductilization of Mo-Si solid solutions manufactured by powder metallurgy.* Acta Materialia, 2009. **57**(13): p. 3895-3901.

70. Ciulik, J. and Taleff, E., *Power-law creep of powder-metallurgy grade molybdenum sheet.* Materials Science and Engineering: A, 2007. **463**(1): p. 197-202.

71. Floquet, N., Bertrand, O., and Heizmann, J., *Structural and morphological studies of the growth of MoO_3 scales during high-temperature oxidation of molybdenum.* Oxidation of metals, 1992. **37**(3-4): p. 253-280.

72. Sturm, D., Heilmaier, M., Schneibel, J.H., et al., *The influence of silicon on the strength and fracture toughness of molybdenum.* Materials Science and Engineering: A, 2007. **463**(1): p. 107-114.

73. Gokhale, A. and Abbaschian, G., *The Mo-Si (molybdenum-silicon) system.* Journal of Phase Equilibria, 1991. **12**(4): p. 493-498.

74. Miller, M., Kenik, E., Mousa, M., et al., *Improvement in the ductility of molybdenum alloys due to grain boundary segregation.* Scripta materialia, 2002. **46**(4): p. 299-303.

75. Scruggs, D., *Ductile molybdenum composition containing a spinel dispersion*. U.S. Patent Nr. 3,320,036, 1967.

76. Schneibel, J.H., Brady, M.P., Kruzic, J., et al., *On the improvement of the ductility of molybdenum by spinel ($MgAl_2O_4$) particles.* Zeitschrift für Metallkunde, 2005. **96**(6): p. 632-637.

77. Gunter, I., Schneibel, J.H., and Kruzic, J., *Ductility and fracture toughness of molybdenum with $MgAl_2O_4$ additions.* Materials Science and Engineering: A, 2007. **458**(1): p. 275-280.

78. Petrovic, J.J., *Mechanical behavior of $MoSi_2$ and $MoSi_2$ composites.* Materials Science and Engineering: A, 1995. **192**: p. 31-37.

79. Ito, K., Nakamoto, T., Inui, H., et al. *Stacking Faults on (001) in Transition-Metal Disilicides with The $C11_b$ Structure*. in *MRS Proceedings*. 1996, Cambridge Univ Press. p. 599.

80. Peralta, P., Maloy, S., Chu, F., et al., *Mechanical properties of monocrystalline C11b $MoSi_2$ with small aluminum additions.* Scripta materialia, 1997. **37**(10): p. 1599-1604.

81. Yoo, M. and Yoshimi, K. *Ideal cleavage fracture of transition-metal silicides: a comparison analysis*. in *MRS Proceedings*. 1998, Cambridge Univ Press. p. KK6-6.

82. Wade, R.K. and Petrovic, J.J., *Fracture modes in $MoSi_2$.* Journal of the American Ceramic Society, 1992. **75**(6): p. 1682-1684.

83. Petrovic, J., *Toughening strategies for $MoSi_2$-based high temperature structural silicides.* Intermetallics, 2000. **8**(9): p. 1175-1182.

84. Kircher, T.A. and Courtright, E.L., *Engineering limitations of $MoSi_2$ coatings.* Materials Science and Engineering: A, 1992. **155**(1): p. 67-74.

85. Sharif, A., *High-temperature oxidation of $MoSi_2$.* Journal of materials science, 2010. **45**(4): p. 865-870.

86. Petrovic, J.J., *MoSi 2-based high-temperature structural silicides.* MRS Bulletin, 1993. **18**(07): p. 35-41.

87. Liu, Y., Shao, G., and Tsakiropoulos, P., *On the oxidation behaviour of $MoSi_2$.* Intermetallics, 2001. **9**(2): p. 125-136.

88. Yanagihara, K., Przybylski, K., and Maruyama, T., *The role of microstructure on pesting during oxidation of $MoSi_2$ and $Mo(Si, Al)_2$ at 773K.* Oxidation of metals, 1997. **47**(3-4): p. 277-293.

89. Kumar, K. and Liu, C., *Ordered intermetallic alloys, part II: silicides, trialuminides, and others.* JOM, 1993. **45**(6): p. 28-34.

90. Umakoshi, Y., Sakagami, T., Hirano, T., et al., *High temperature deformation of $MoSi_2$ single crystals with the C11b structure.* Acta Metallurgica et Materialia, 1990. **38**(6): p. 909-915.

91. Maloy, S., Mitchell, T., Petrovic, J.J., et al. *The Temperature and Strain Rate Dependence of the Flow Stress in $MoSi_2$ Single Crystals*. in *MRS Proceedings*. 1993: Cambridge Univ Press.

92. Kimura, K., Nakamura, M., and Hirano, T., *High temperature deformation behaviour of $MoSi_2$ and WSi_2 single crystals.* Journal of Materials Science, 1990. **25**(5): p. 2487-2492.

93. Severin, K.P., *Energy Dispersive Spectrometry of Common Rock Forming Minerals*. 2004: Springer.

94. Inui, H., Ishikawa, K., and Yamaguchi, M., *Creep deformation of single crystals of binary and some ternary $MoSi_2$ with the C11b structure.* Intermetallics, 2000. **8**(9): p. 1159-1168.

95. Nunes, C., Sakidja, R., Dong, Z., et al., *Liquidus projection for the Mo-rich portion of the Mo-Si-B ternary system.* Intermetallics, 2000. **8**(4): p. 327-337.

96. Christensen, A.N., *Preparation and Characterization of Mo_3Si and Mo_5Si_3.* Acta Chemica Scandinavica: A, 1983. **37**(6).

97. Rosales, I. and Schneibel, J., *Stoichiometry and mechanical properties of Mo_3Si.* Intermetallics, 2000. **8**(8): p. 885-889.

98. Ochiai, S. *Influence of the addition of Cr and Al elements to the Mo_3Si intermetallic alloy on the phase construction and the oxidation behavior*. in *Materials Science Forum*. 2003. Trans Tech Publ.

99. Rosales, I., Martinez, H., Bahena, D., et al., *Oxidation performance of Mo_3Si with Al additions.* Corrosion Science, 2009. **51**(3): p. 534-538.

100. Rosales, I., Schneibel, J., Heatherly, L., et al., *High temperature deformation of A15 Mo_3Si single crystals.* Scripta materialia, 2003. **48**(2): p. 185-190.

101. Ström, E., *Mechanical properties of Mo_5Si_3 intermetallics as a function of composition.* Materials characterization, 2005. **55**(4): p. 402-411.

102. Chu, F., Thoma, D., McClellan, K., et al., *Synthesis and properties of Mo_5Si_3 single crystals.* Intermetallics, 1999. **7**(5): p. 611-620.

103. Briant, C., Petrovic, J.J., Bewlay, B.P., et al., *High Temperature Silicides and Refractory Alloys.* Boston, 1993: Cambridge University Press.

104. Meyer, M.K., *Oxidation and creep behavior of Mo_5Si_3 based materials.* Iowa State University, Dissertation, 1995.

105. Meyer, M.K. and Akinc, M., *Oxidation Behavior of Boron-Modified Mo_5Si_3 at 800°-1300°C.* Journal of the American Ceramic Society, 1996. **79**(4): p. 938-944.

106. Akinc, M., Meyer, M.K., Kramer, M.J., et al., *Boron-doped molybdenum silicides for structural applications.* Materials Science and Engineering: A, 1999. **261**(1): p. 16-23.

107. Yoshimi, K., Yoo, M., Wereszczak, A., et al., *Deformation behavior of Mo_5Si_3 single crystal at high temperatures.* Materials Science and Engineering: A, 2002. **329**: p. 228-234.

108. Meyer, M.K., Kramer, M.J., and Akinca, M., *Compressive creep behavior of Mo_5Si_3 with the addition of boron.* Intermetallics, 1996. **4**(4): p. 273-281.

109. Chokshi, A. and Langdon, T., *Characteristics of creep deformation in ceramics.* Materials Science and Technology, 1991. **7**(7): p. 577-584.

110. Lemberg, J. and Ritchie, R., *Mo-Si-B Alloys for Ultrahigh-Temperature Structural Applications.* Advanced Materials, 2012. **24**(26): p. 3445-3480.

111. Meyer, M., Thom, A., and Akinc, M., *Oxide scale formation and isothermal oxidation behavior of Mo-Si-B intermetallics at 600-1000°C.* Intermetallics, 1999. **7**(2): p. 153-162.

112. Parthasarathy, T., Mendiratta, M., and Dimiduk, D., *Oxidation mechanisms in Mo-reinforced Mo_5SiB_2 (T2)-Mo_3Si alloys.* Acta Materialia, 2002. **50**(7): p. 1857-1868.

113. Supatarawanich, V., Johnson, D., and Liu, C., *Oxidation behavior of multiphase Mo-Si-B alloys.* Intermetallics, 2004. **12**(7): p. 721-725.

114. Supatarawanich, V., Johnson, D., and Liu, C., *Effects of microstructure on the oxidation behavior of multiphase Mo-Si-B alloys.* Materials Science and Engineering: A, 2003. **344**(1): p. 328-339.

115. Wang, F., Shan, A., Dong, X., et al., *Microstructure and oxidation resistance of laser-remelted Mo-Si-B alloy.* Scripta materialia, 2007. **56**(9): p. 737-740.

116. Majumdar, S., Schliephake, D., Gorr, B., et al., *Effect of yttrium alloying on intermediate to high-temperature oxidation behavior of Mo-Si-B alloys.* Metallurgical and Materials Transactions A, 2013. **44**(5): p. 2243-2257.

117. Gorr, B., Wang, L., Burk, S., et al., *High-temperature oxidation behavior of Mo-Si-B-based and Co-Re-Cr-based alloys.* Intermetallics, 2014. **48**: p. 34-43.

118. Poulton, D. and Smeltzer, W., *Oxygen diffusion in monoclinic zirconia.* Journal of the Electrochemical Society, 1970. **117**(3): p. 378-381.

119. Burk, S., Gorr, B., Trindade, V., et al., *Effect of Zr addition on the high-temperature oxidation behaviour of Mo-Si-B alloys.* Oxidation of metals, 2010. **73**(1-2): p. 163-181.

120. Majumdar, S., Burk, S., Schliephake, D., et al., *A study on effect of reactive and rare earth element additions on the oxidation behavior of Mo-Si-B system.* Oxidation of metals, 2013. **80**(3-4): p. 219-230.

121. Schliephake, D., Azim, M., von Klinski-Wetzel, K., et al., *High-temperature creep and oxidation behavior of Mo-Si-B alloys with high Ti contents.* Metallurgical and Materials Transactions A, 2014. **45**(3): p. 1102-1111.

122. Jain, P. and Kumar, K., *Tensile creep of Mo-Si-B alloys.* Acta Materialia, 2010. **58**(6): p. 2124-2142.

123. Schneibel, J., *High temperature strength of Mo-Mo$_3$Si-Mo$_5$SiB$_2$ molybdenum silicides.* Intermetallics, 2003. **11**(7): p. 625-632.

124. Yoshimi, K., Nakamura, J., Kanekon, D., et al., *High-Temperature Compressive Properties of TiC-Added Mo-Si-B Alloys.* JOM, 2014. **66**(9): p. 1930-1938.

125. Hochmuth, C., Schliephake, D., Völkl, R., et al., *Influence of zirconium content on microstructure and creep properties of Mo-9Si-8B alloys.* Intermetallics, 2014. **48**: p. 3-9.

126. Yu, J., Li, Z., Zheng, X., et al., *Tensile properties of multiphase Mo-Si-B refractory alloys at elevated temperatures.* Materials Science and Engineering: A, 2012. **532**: p. 392-395.

127. Yoshimi, K., Nakatani, S., Nomura, N., et al., *Thermal expansion, strength and oxidation resistance of Mo/Mo$_5$SiB$_2$ in-situ composites at elevated temperatures.* Intermetallics, 2003. **11**(8): p. 787-794.

128. Mitra, R. and Rao, V.V.R., *Elevated-temperature oxidation behavior of titanium silicide and titanium silicide-based alloy and composite.* Metallurgical and Materials Transactions A, 1998. **29**(6): p. 1665-1675.

129. Williams, J. and Akinc, M., *Oxidation resistance of Ti$_5$Si$_3$ and Ti$_5$Si$_3$ Zx at 1000 ℃ (Z= C, N, or O).* Oxidation of Metals, 2002. **58**(1): p. 57-71.

130. Burk, S., Gorr, B., Christ, H.-J., et al., *High-temperature oxidation behaviour of a single-phase (Mo, Ti)$_5$Si$_3$ (Mo-Si-Ti) alloy.* Scripta Materialia, 2012. **66**(5): p. 223-226.

131. Yang, Y., Chang, Y., Tan, L., et al., *Experimental investigation and thermodynamic descriptions of the Mo-Si-Ti system.* Materials Science and Engineering: A, 2003. **361**(1): p. 281-293.

132. Yang, Y., Bei, H., Chen, S., et al., *Effects of Ti, Zr, and Hf on the phase stability of Mo_ss+ Mo$_3$Si+ Mo$_5$SiB$_2$ alloys at 1600 ℃.* Acta Materialia, 2010. **58**(2): p. 541-548.

133. Zhang, L. and Wu, J., *Thermal expansion and elastic moduli of the silicide based intermetallic alloys Ti$_5$Si$_3$(X) and Nb$_5$Si$_3$.* Scripta materialia, 1997. **38**(2): p. 307-313.

134. Rosenkranz, R., Frommeyer, G., and Smarsly, W., *Microstructures and properties of high melting point intermetallic Ti_5Si_3 and $TiSi_2$ compounds.* Materials Science and Engineering: A, 1992. **152**(1-2): p. 288-294.

135. Min, K.S., Ardell, A., Eck, S., et al., *A small-specimen investigation of the fracture toughness of Ti_5Si_3.* Journal of materials science, 1995. **30**(21): p. 5479-5483.

136. Mitra, R., Eswara Prasad, N., and Mahajan, Y., *Mechanical behaviour of Ti_5Si_3 based alloys and composites.* Transactions of the Indian Institute of Metals, 2008. **61**(5): p. 427-433.

137. Abba, A., Galerie, A., and Caillet, M., *High-temperature oxidation of titanium silicide coatings on titanium.* Oxidation of metals, 1982. **17**(1-2): p. 43-54.

138. Taniguchi, S., Minamida, T., and Shibata, T. *Oxidation Behaviour of Ti_5Si_3 at Temperatures between 1400 and 1700K. Materials science forum*. Trans Tech Publications, 1997. **251**:p.227-234.

139. Tang, Z., Williams, J.J., Thom, A.J., et al., *High temperature oxidation behavior of Ti_5Si_3-based intermetallics.* Intermetallics, 2008. **16**(9): p. 1118-1124.

140. Tang, Z., Thom, A.J., and Akinc, M., *Role of nitrogen on the oxidative stability of Ti_5Si_3 based alloys at elevated temperature.* Intermetallics, 2006. **14**(5): p. 537-543.

141. Meschter, P.J. and Schwartz, D.S., *Silicide-matrix materials for high-temperature applications.* JOM Journal of the Minerals, Metals and Materials Society, 1989. **41**(11): p. 52-55.

142. Sandwick, T. and Rajan, K., *The oxidation of titanium silicide.* Journal of electronic materials, 1990. **19**(11): p. 1193-1199.

143. Frommeyer, G., *Microstructure and properties of the refractory intermetallic Ti_5Si_3 compound and the unidiectionally solidified eutectic.* Metallkunde, 1990. **81**: p. 307-313.

144. Zhou, W., Apkarian, R., Wang, Z.L., et al., *Fundamentals of scanning electron microscopy (SEM)*, in *Scanning microscopy for nanotechnology*. 2006: Springer.

145. Smith, K. and Oatley, C., *The scanning electron microscope and its fields of application.* British Journal of Applied Physics, 1955. **6**(11): p. 391.

146. Nixon, W., *The general principles of scanning electron microscopy.* Philosophical Transactions of the Royal Society of London. Series B, Biological Sciences, 1971. **261**(837): p. 45-50.

147. Ngo, P.D., *Energy dispersive spectroscopy*, in *Failure Analysis of Integrated Circuits*. 1999: Springer.

148. Newbury, D.E., *Energy-Dispersive Spectrometry.* Characterization of Materials, 2002: Springer.

149. Robin, D., *Implementation, Analytical Characterization and Application of a Novel Portable XRF/XRD Instrument.* Universiteit Gent, Dissertation, 2012.

150. Suryanarayana, C. and Norton, M.G., *X-ray diffraction: a practical approach*. 2013: Springer Science & Business Media.

151. Seemüller, H.C.M., *Evaluation of Powder Metallurgical Processing Routes for Multi-Component Niobium Silicide-Based High-Temperature Alloys*. Karlsruher Institut für Technologie, Dissertation, 2016.

152. Gulliver, G., *The quantitative effect of rapid cooling upon the constitution of binary alloys.* Journal of the Japan Institute of Metals, 1913. **9**(1): p. 120-157.

153. Scheil, E., *Bemerkungen zur schichtkristallbildung.* Zeitschrift für Metallkunde, 1942. **34**(3): p. 70-72.

154. Yang, Y., Chang, Y., Tan, L., et al., *Multiphase equilibria in the metal-rich region of the Mo-Ti-Si-B system: thermodynamic prediction and experimental validation.* Acta materialia, 2005. **53**(6): p. 1711-1720.

155. Exner, H. and Hougardy, H., *Einführung in die quantitative Gefügeanalyse (Introduction to Quantitative Analysis of Microstructures).* Deutsche Gesellschaft für Metallkunde, Oberursel, 1982.

156. Moseev, N., Chudinov, V., Goshchitskh, B., et al., *Molecular Dynamics Study of Atomic Configuration of Point Defects in Intermetallic Compound* Mo_3Si*.* physica status solidi (a), 1986. **94**(1): p. 147-152.

157. Mughrabi, H., *Microstructural aspects of high temperature deformation of monocrystalline nickel base superalloys: some open problems.* Materials Science and Technology, 2009. **25**(2): p. 191-204.

158. Nathal, M., MacKay, R., and Miner, R., *Influence of precipitate morphology on intermediate temperature creep properties of a nickel-base superalloy single crystal.* Metallurgical and Materials Transactions A, 1989. **20**(1): p. 133-141.

159. Yavari, P. and Langdon, T.G., *An examination of the breakdown in creep by viscous glide in solid solution alloys at high stress levels.* Acta Metallurgica, 1982. **30**(12): p. 2181-2196.

160. Schliephake, D., *Der Einfluss von Fe auf Ti-haltige Mo-Si-B Legierungen: Phasenbildung, Gefüge und Druckkriechverhalten.* Karlsruher Institut für Technologie, Dissertation, 2017.

161. Mason, D. and Van Aken, D.C., *On the creep of directionally solidified* $MoSi_2$-Mo_5Si_3 *eutectics.* Acta metallurgica et materialia, 1995. **43**(3): p. 1201-1210.

162. Sadananda, K., Feng, C., Mitra, R., et al., *Creep and fatigue properties of high temperature silicides and their composites.* Materials Science and Engineering: A, 1999. **261**(1): p. 223-238.

163. Azim, M., Schliephake, D., Hochmuth, C., et al., *Creep Resistance and Oxidation Behavior of Novel Mo-Si-B-Ti Alloys.* JOM, 2015. **67**(11): p. 2621-2628.

164. Mughrabi, H., Ott, M., and Tetzlaff, U., *New microstructural concepts to optimize the high-temperature strength of* γ'*-hardened monocrystalline nickel-based superalloys.* Materials Science and Engineering: A, 1997. **234**: p. 434-437.

165. Frost, H.J. and Ashby, M.F., *Deformation mechanism maps: the plasticity and creep of metals and ceramics*. 1982: Pergamon press.

166. Sherby, O.D. and Burke, P.M., *Mechanical behavior of crystalline solids at elevated temperature.* Progress in Materials Science, 1968. **13**: p. 323-390.

167. *DIN EN ISO 643: Mikrophotographische Bestimmung der scheinbaren Korngröße* 2015.

168. Heilmaier, M. and Reppich, B., *Creep lifetime prediction of oxide-dispersion-strengthened nickel-base superalloys: A micromechanically based approach.* Metallurgical and Materials Transactions A, 1996. **27**(12): p. 3861-3870.

169. Bedworth, R. and Pilling, N., *The oxidation of metals at high temperatures.* Journal of the Japan Institute of Metals, 1923. **29**(3): p. 529-582.

170. Moore, W.J., *Oxidation of Metals at High Temperatures.* Journal of The Electrochemical Society, 1953. **100**(7): p. 302-313.

171. Gleeson, B., *High-Temperature Corrosion of Metallic Alloys and Coatings.* Materials science and technology, 2000.

172. An, T., Guan, H., Sun, X., et al., *Effect of the* θ-α-Al_2O_3 *transformation in scales on the oxidation behavior of a nickel-base superalloy with an aluminide diffusion coating.* Oxidation of Metals, 2000. **54**(3-4): p. 301-316.

173. Larson, J. M. and Floreen, S., *Metallurgical factors affecting the crack growth resistance of a superalloy.* Metallurgical Transactions A, 1977. **8**(1): p. 51-55.

174. Raffaitin, A., Monceau, D., Andrieu, E., et al., *Cyclic oxidation of coated and uncoated single-crystal nickel-based superalloy MC2 analyzed by continuous thermogravimetry analysis.* Acta materialia, 2006. **54**(17): p. 4473-4487.

175. Abderrazik, G.B., Moulin, G., and Huntz, A., *Relation between impurities and oxide-scale growth mechanisms on Ni-34Cr and Ni-20Cr alloys. I. Influence of C, Mn, and Si.* Oxidation of Metals, 1990. **33**(3): p. 191-235.

176. Vialas, N., Monceau, D., and Pieraggi, B. *Effect of cycle frequency on high temperature oxidation behavior of alumina-forming coatings used for industrial gas turbine blades*. Materials science forum, 2004. **461-464**: p. 747-754.

177. Babu, N., Balasubramaniam, R., and Ghosh, A., *High-temperature oxidation of* Fe_3Al*-based iron aluminides in oxygen.* Corrosion Science, 2001. **43**(12): p. 2239-2254.

178. Haynes, J., Pint, B., Porter, W., et al., *Comparison of thermal expansion and oxidation behavior of various high-temperature coating materials and superalloys.* Materials at high temperatures, 2004. **21**(2): p. 87-94.

179. Melsheimer, S., Fietzek, M., Kolarik, V., et al., *Oxidation of the intermetallics* $MoSi_2$ *and* $TiSi_2$*-A comparison.* Oxidation of Metals, 1997. **47**(1): p. 139-203.

180. Kofstad, P., *Nonstoichiometry, diffusion, and electrical conductivity in binary metal oxides*. 1972: Wiley-Interscience New York.

181. Azim, M.A., Burk, S., Gorr, B., et al., *Effect of Ti (Macro-) Alloying on the High-Temperature Oxidation Behavior of Ternary Mo-Si-B Alloys at 820-1,300 ℃.* Oxidation of metals, 2013. **80**(3-4): p. 231-242.

182. Mendiratta, M., Parthasarathy, T., and Dimiduk, D., *Oxidation behavior of αMo-*Mo_3Si*-*Mo_5SiB_2 *(T2) three phase system.* Intermetallics, 2002. **10**(3): p. 225-232.

183. Deschamps, J., Georgelin, M., and Pocheau, A., *Crystal anisotropy and growth directions in directional solidification.* Europhysics Letters, 2006. **76**(2): p. 291.

184. Versnyder, F.I. and Shank, M., *The development of columnar grain and single crystal high temperature materials through directional solidification.* Materials Science and Engineering, 1970. **6**(4): p. 213-247.

185. Hasemann, G., Bogomol, I., Schliephake, D., et al., *Microstructure and creep properties of a near-eutectic directionally solidified multiphase Mo-Si-B alloy.* Intermetallics, 2014. **48**: p. 28-33.

186. Kazemi, O., Hasemann, G., Krüger, M., et al. *Phase field simulation of a directional solidification of a ternary eutectic Mo-Si-B Alloy*. IOP Conference: Materials Science and Engineering. 2016.

187. Mitra, R., Chattopadhyay, K., Srivastava, A.K., et al. *Effect of Ductile and Brittle Phases on Deformation and Fracture Behaviour of Molybdenum and Niobium Silicide Based Composites*. Key Engineering Materials, 2009. **395**(1): p. 179-192.

188. Choe, H., Schneibel, J., and Ritchie, R., *On the fracture and fatigue properties of Mo-*Mo_3Si*-*Mo_5SiB_2 *refractory intermetallic alloys at ambient to elevated temperatures (25 ℃ to 1300 ℃).* Metallurgical and materials transactions A, 2003. **34**(2): p. 225-239.

189. Schneibel, J.H., Kramer, M., Ünal, Ö., et al., *Processing and mechanical properties of a molybdenum silicide with the composition Mo-12Si-8.5 B (at.%).* Intermetallics, 2001. **9**(1): p. 25-31.

8 Appendix

Table 8.1: Crystal structure and Lattice constants of possible phases in E1-E4 detected by XRD (*Angles are given only when not fixed by lattice symmetry

Phase	Crystal Structure	n	Lattice constant (Å)			V (Å^3)	
			a	b	c		
Mo	bodycenteredcubic	2	3.1472	-	-	a^3	31.2
Ti$_5$Si$_3$	hexagonal (D8$_8$)	16	7.444	-	5.143	a^2 c sin60 °	246.8
Mo$_5$Si$_3$	bodycentered tetragonal (D8$_m$, tI32)	32	9.6483	-	4.9135	a^2 c	457.4

Table 8.2: Relative parameters for the eutectic microstructures in E1-E4

Eutectic		$X_{(Mo, Ti, Si)}$ (at.%)	$X_{(Ti,Mo)_5Si_3}$ (at.%)	$f_{(Mo, Ti, Si)}$ (at.%)	$f_{(Ti,Mo)_5Si_3}$ (at.%)	$W_{(Mo, Ti, Si)}$ (wt.%)	$W_{(Ti,Mo)_5Si_3}$ (wt.%)	$\rho_{(Mo, Ti, Si)}$ (g/cm^3)	$\rho_{(Ti,Mo)_5Si_3}$ (g/cm^3)
E1	**Mo**	52.7	8.5	54.5	45.5	66.1	33.9	7.74	4.82
	Si	3.0	37.5						
	Ti	44.3	54.0						
E2	**Mo**	44.4	6.6	52.4	47.6	63.5	36.5	7.32	4.72
	Si	2.4	37.5						
	Ti	53.2	55.9						
E3	**Mo**	49.7	7.7	53.3	46.7	64.8	35.2	7.59	4.78
	Si	2.8	37.5						
	Ti	47.5	54.8						
E4	**Mo**	50.1	7.8	41.5	58.5	53.4	46.6	7.61	4.78
	Si	2.8	37.5						
	Ti	47.1	54.7						
E5	**Mo**	47.1	7.2	49.8	49.7	61.2	38.4	7.46	4.73
	Si	2.6	37.5						
	Ti	50.3	55.3						

Table 8.3: Crystal structure and Lattice constants of possible phases in X1-X3 detected by XRD (*Angles are given only when not fixed by lattice symmetry)

Phase	**Crystal Structure**	**n**	**Lattice Constant *(Å)***			***V (Å^3)***	
			a	**b**	**c**		
Mo$_3$Si	A15	8	4.893	-	-	a^3	117.1
Ti$_5$Si$_3$	hexagonal (D8$_8$)	16	7.444	-	5.143	$a^2 c \sin 60°$	246.8
Mo$_5$Si$_3$	body-centered tetragonal (D8$_m$, tI32)	32	9.6483	-	4.9135	$a^2 c$	457.4

Table 8.4: Crystal structure and Lattice constants of possible phases on the surface ofX5 in the oxidation temperature range of 800 ℃-1200 ℃ detected by XRD (*Angles are given only when not fixed by lattice symmetry)

Phase	**Crystal Structure**	**n**	**Lattice Constant *(Å)***			***V (Å^3)***	
			a	**b**	**c**		
TiO$_2$	Tetragonal	6	4.593	-	2.959	$a^2 c$	62.4
SiO$_2$	Trigonal hexagonal	9	4.913	-	5.405	$a^2 c \sin 60°$	113.0

Acknowledgments

First and foremost, I would like to sincerely express my deep gratitude to Prof. Dr.-Ing. Martin Heilmaier for the opportunity to carry out this work and his invaluable scientific guidance. He was always willing to discuss with me difficulties of my research and provided me with scientific guidance and support. Without his guidance, this work would never have come to fruition.

Furthermore, I would like to thank Dr. Alexander Kauffmann for his kind and selfless help in the stage of my research work at the IAM-WK. When I got stuck, he gave me new perspectives through many fruitful discussions. He standardized my experimental skills and improvied my scientific thought during the study.

I would like to thank Daniel Schliephake for his effective cooperation and stimulating discussions during my PhD work.

I would also like to thank my colleagues from IAM-WK, especially the members of the Physical Metallurgy group, for their help and support. I will only name a few: Camelia Gombola and Hans Chen for TGA and XRD testing; Adelheid Ohl and Michaela Nagel from IAM-WK for their restless support in the metallography.

My gratitude goes to China Scholarship Council (CSC) and KIT for providing the funding for my research work.

I would like to thank my friends Monika Vogt, Jörg Vogt, Yujie Tsang, lovely Malena and Katrina for their continued support through all ups and downs.

I would like to thank my friends Dr. Jie Ye, Dr. Dandan Qu, Dr. Meng He, Dr. Zhi Chen, Dr. Di Chen, Dr. Zhenzhong Yu, Dr. Ping Gao, Dr. Wenqian Feng and Dr. Yuantao Cui for their warm friendship that made my stay in Karlsruhe pleasant.

Last but not least, I would like to thank my beloved parents and all my family members for their never-ending love and support.